A PRECISION MEASUREMENT OF THE ^{129}Xe ELECTRIC DIPOLE MOMENT USING DUAL NOBLE GAS MASERS

by

Mark A. Rosenberry

A dissertation submitted in partial fulfillment
of the requirements for the degree of
Doctor of Philosophy
(Physics)
in The University of Michigan
2000

Doctoral Committee:

Professor Timothy Chupp, Chairperson
Professor Joel Bregman
Associate Research Scientist Ralph Conti
Professor Gordan Kane
Professor Steven Rand

For Andrea, who dreams with me

ACKNOWLEDGEMENTS

I would like to thank the numerous people whose support made this project possible. First is my thesis advisor, Timothy Chupp, who has done so much to keep me going in the right direction through the years. Next I thank the other members of the Michigan group: Kevin, Robert, Matt, Todd, Shenq-Rong, and Jon. All of them graciously made time to help me solve problems with my system. I am grateful for the help of three talented undergraduates, Bill Peters, Sam Stavis, and Jeff Wright, who all made important contributions to the physical apparatus. I thank our glassblower, Harold Eberhart, for the hundreds of cells he made, and his advice concerning their design.

The assistance of our colleagues at the Harvard-Smithsonian Center for Astrophysics is also deeply appreciated. I thank Ron Walsworth for his encouragement throughout the project, and his welcome when I worked in Boston. Thanks to my counterpart David Bear, who has worked hard with me, and whose conversations have helped keep me sane. Most importantly I thank Rick Stoner. Without his many ideas and ceaseless enthusiasm this project would have gotten nowhere.

Finally I must thank all the people whose love made this project bearable. Thanks so much Mom and Dad. This time graduating is a big deal. Thanks to my many friends here for the games that kept life fun. Thanks most of all to my wife Andrea, who has been there for me every day. You make everything I do special.

PREFACE

This dissertation describes a measurement of the permanent electric dipole moment (EDM) in ^{129}Xe. An EDM violates both parity and time reversal, and so its size sets limits on the **CP**-violating parameters of the Standard Model and its extensions. Two species of noble gas Zeeman masers were employed to achieve this precision. Zeeman masers are tools that permit very long running times and the advantages of *in situ* magnetometry. The Bloch equations that model the maser behavior are derived, and their solution predicts the maser polarizations for different system settings. Details of the construction of the apparatus (particularly the EDM cells employed) are provided. Over a six month period the experiment achieved a statistical sensitivity of 2.84 $\times 10^{-27}$ e cm but was limited by a systematic effect whose origin is unknown. Various approaches for identifying and eliminating this systematic are discussed.

TABLE OF CONTENTS

LIST OF FIGURES

Figure

LIST OF TABLES

Table

LIST OF APPENDICES

Appendix

CHAPTER I

Motivation for the Experiment

This experiment is designed to measure the permanent electric dipole moment (EDM) of xenon-129. This introductory chapter is intended to explain why such a measurement is important, and to familiarize the reader with the issues involved. Specifically discussed are the improper symmetries such as parity (**P**) and time reversal (**T**), and how an atomic EDM violates them. The neutral kaon system, where **T**-violation has been observed, is described in some detail. The fundamental particle interactions between the atom's components that give rise to such violations are presented next, along with several theories of such interactions which predict EDM values close to current experimental sensitivity. The final section presents the limits on theories of elementary particle physics (such as supersymmetry) that can be set by an experiment done on a table-top employing high-precision atomic techniques.

1.1 Symmetries

In order to describe how a system of particles evolves with time, one writes down equations of motion. If the system is complex, it is often helpful to investigate how these equations change if one transforms some of the variables. If the same equations of motion describe the system after the transformation, then the transformation is said to be a symmetry. Note that the transformation may change the solution to the equations of motion, because we have different initial conditions. However, a transformation is asymmetric only if a new set of equations are required to describe the evolution of the system, and not just a change in the initial conditions. A symmetry

is said to be violated when the transformation does not preserve the equations of motion for the system of interest.

Familiar symmetries include spatial translation and rotation. These are termed proper symmetries because they can be carried out continuously in infinitesimal steps. As an example, one can imagine winding up a toy car and releasing it on a flat surface. The car can be placed in a variety of different positions, or facing different directions, but the motion of the car after its release will not vary. There are also improper transformations, which can not be built up from infinitesimal steps; they are all or nothing. Parity (**P**) and time reversal (**T**), along with charge conjugation (**C**), are improper or discrete transformations. Under a parity operation, one changes from a left-handed co-ordinate system to a right-handed one: i.e. $\vec{x} \rightarrow -\vec{x}$. If parity is a good symmetry, then the same equations of motion should describe a process viewed normally and the same process viewed in a mirror. A time reversal operation changes the sign of the time co-ordinate, so that time progresses backwards rather than forwards. Classically, time reversal holds if the same equations describe a scene in a movie played forwards or played backwards. (Quantum mechanically this is not quite true, but it still provides a useful analogy.) Charge conjugation transforms all particles to their corresponding anti-particles, reversing the quantum numbers of charge, lepton number, etc. Unfortunately this operation has no intuitive analog. All three improper transformations are symmetries for all ordinary, long-range interactions.

A system will often be described as "even" or "odd" under a transformation. For parity or charge conjugation, the system is even if the eigenvalue of the operator is 1 ($\mathbf{P\Psi}(\vec{x},\mathbf{t}) = \mathbf{\Psi}(\vec{x},\mathbf{t})$). The system is odd if the eigenvalue is -1 ($\mathbf{P\Psi}(\vec{x},\mathbf{t}) = -\mathbf{\Psi}(\vec{x},\mathbf{t})$). If the eigenvalue for the transformation is neither 1 or -1, then the system is not in an eigenstate of the transformation and so is not even or odd. There is an added complication for time reversal, because quantum mechanical time reversal includes complex conjugation. The time reversal operator is $\mathbf{T} = \mathbf{U}\ \mathbf{K}$ [76], where **K** is the complex conjugation operator and **U** is a unitary transformation analogous to P above. Multiplying out $\mathbf{TT} = \mathbf{UKUK} = \mathbf{UU}^*$ gives $T^2 = \pm 1$. In analogy to parity and charge conjugation, $T^2 = 1$ for even systems and $T^2 = -1$ for odd systems.

A measurement of an electric dipole moment is important because an EDM vio-

lates parity and time reversal. An electric dipole moment is defined as [42]

$$\vec{\mathrm{d}} = \int \vec{\mathrm{r}}\,\rho(\vec{\mathrm{r}})\,\mathrm{d}^3\mathrm{r} \tag{1.1}$$

where $\rho(\vec{\mathrm{r}})$ describes the charge distribution of the system. A simple set of pictures makes it clear how an EDM violates symmetries. Take a particle with some net spin, and imagine that it also has a separation of charge. The Wigner-Eckhart theorem [79] requires that the charge separation must lie along the spin axis. Under a time reversal operation, the orientation of charge remains the same, but the direction of spin changes: thus time reversal is violated. The case for parity is completely analogous. Note that an EDM is both **P** odd and **T** odd.

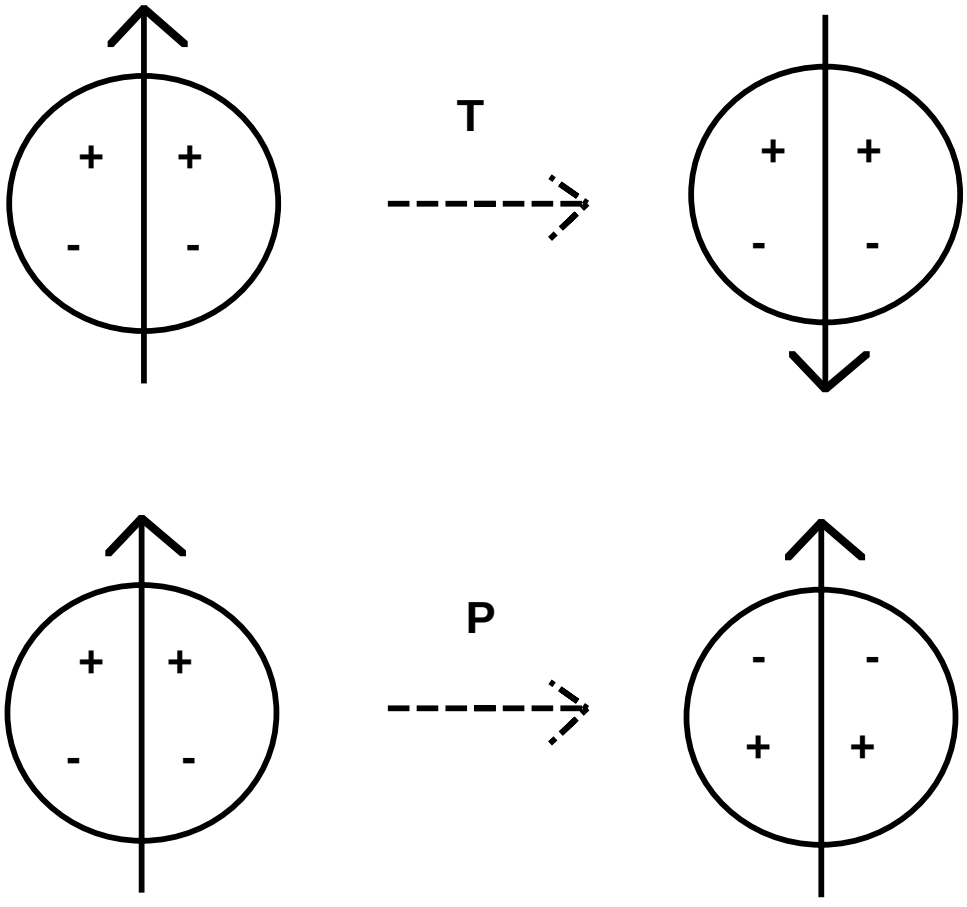

Figure 1.1: An EDM violates Parity and Time Reversal

It is important to note that the atom in the above picture remains static, so that the EDM is time-independent. There are many cases of molecules that are said to

have electric dipole moments: water, NH_3, and HF for example. The energy shift in the molecular states is indeed linearly dependent on the electric field. However, these observed moments are induced by the electric field because of the degenerate ground states of the molecule. The dipole moment does not exist at zero field: hence its expectation value is not permanent in the same way as a true EDM.

Over the past fifty years, there has been considerable work done studying violations of **C**, **P** and **T**. It has been well established that parity (**P**) symmetry is violated in weak interactions, and the experiment of Christenson, Cronin, Fitch, and Tuylay [9] in 1964 demonstrated that the combined charge-parity (**CP**) symmetry is violated in the decay of neutral kaons. Recently, the CPLEAR collaboration at CERN has shown direct time reversal invariance (**T**) violation, again in the neutral kaon system [80]. This had long been expected, because of the powerful **CPT** theorem. This theorem requires that acting on any state with all three operations **C**,**P**, and **T** must return the original state. It has been rigorously proven for any local theory which satisfies Lorentz invariance [58]. Thus a **CP** violation should be synonymous with a **T**, or time reversal, violation. Numerous searches have been made for either **CP** or **T** violation in other systems. So far, the baryon asymmetry of the universe is the only other evidence of such a violation [54] , and that evidence is rather hard to quantify. However, the continuing experiments have succeeded in pushing down the upper limits on time reversal violating effects by many orders of magnitude in the past four decades.

1.2 Known CP violation: Kaon Decay

As mentioned above, the only direct experimental measurement of **CP** violation has occurred in neutral kaons. It is therefore worth a brief digression to discuss the kaon system. The neutral kaon K_0 is a meson composed of a strange antiquark ($\overline{s}$) and a down quark (d). Its anti-particle the $\overline{K_0}$, composed of an s and a $\overline{d}$. Since both the K_0 and the $\overline{K_0}$ undergo strangeness-nonconserving decay into pions, it is possible to change a K_0 into a $\overline{K_0}$ (or visa versa) through a second-order interaction.

It was originally assumed that this mixing would give rise to two distinct eigen-

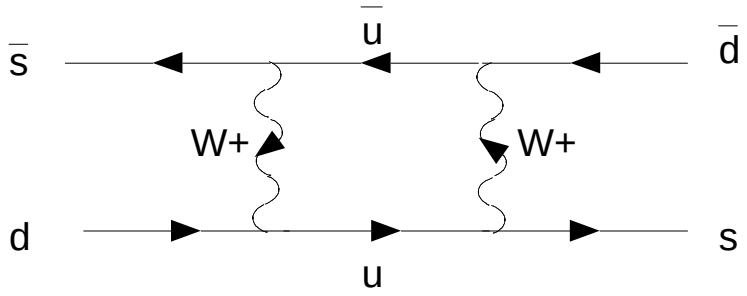

Figure 1.2: A Neutral Kaon transforms to its own anti-particle

states,

$$|K_1> = \frac{1}{\sqrt{2}}(|K_0> + |\overline{K_0}>) \tag{1.2}$$

$$|K_2> = \frac{1}{\sqrt{2}}(|K_0> - |\overline{K_0}>) \tag{1.3}$$

It is easy to see that **CP** acting on K_1 returns K_1 (CP = +1) whereas **CP** acting on K_2 returns $-K_2$ (CP = -1). Thus K_1 is **CP** even and K_2 is **CP** odd. Therefore, in order to conserve **CP** a K_1 must decay into two pions and a K_2 must decay into three. Limitations in the available energy (the kaon mass is only 3.5 times the pion mass [69]) mean that the decay into three pions is much slower than the decay into two.

When the 1964 experiment was performed, a short-lived state K_S and a long-lived state K_L were indeed observed. However, careful measurements showed that the states were not **CP** eigenstates. The K_L decayed into two pions for a small fraction of the events. The size of the **CP** violation is quantified by this fraction ε

$$|K_L> = \frac{|K_2> + \varepsilon|K_1>}{\sqrt{1+|\varepsilon|^2}} \tag{1.4}$$

The measurement found $|\varepsilon| \approx 2.3 \times 10^{-3}$

The work of CPLEAR looked for a chain of events that began with a proton and anti-proton annihilating to produce a charged kaon, a charged pion, and either a K_0 or a $\overline{K_0}$ [80]. The sign of the charged kaon revealed which neutral kaon was initially produced. The researchers then looked for decays of the neutral kaon to see if the original particle had changed to its counterpart between the time of its creation and its demise. They found a clear difference between the rates of $K_0 \rightarrow \overline{K_0}$

and $\overline{K_0} \rightarrow K_0$, of magnitude

$$\frac{(\overline{K_0} \rightarrow K_0) - (K_0 \rightarrow \overline{K_0})}{(\overline{K_0} \rightarrow K_0) + (K_0 \rightarrow \overline{K_0})} = (6.6 \pm 1.6) \times 10^{-3} \tag{1.5}$$

When combined with the results of other experiment's analysis at CPLEAR (which confirm **CPT**-invariance and $\Delta S = \Delta Q$ for this experiment [22]) this demonstrates direct **T**-violation.

Clearly an impressive amount effort has gone into observing **CP**-violation in the neutral kaon system. However, many proposed **CP** violating processes, including the baryon asymmetry of the universe, are not flavor changing and so would have to arise from a separate mechanism. EDM measurements are one of the best ways to set limits on many of the mechanisms that theorists have proposed.

1.3 Sources of CP violation in Elementary Particle Theory

An atomic EDM would either arise from an intrinsic fermion EDM or the elementary particle interactions among the atom's constituents. The Standard Model and its various extensions have different **CP** violating parameters that could lead to an EDM. Searches that can set new limits on **T** violation thus provide much needed evidence to determine which of the theories are physically permissible. Below I discuss some of the various theories and how they apply to my search. The discussion generally follows the work of Barr [1], [3].

The Standard Model has two potentially **CP** violating parameters. One is δ_{KM}, the imaginary phase of the 3x3 Kobayashi-Maskawa matrix. δ_{KM} only causes **CP** violation in flavor-changing processes, such as those involved in kaon decay. It has been shown that δ_{KM}'s contributions to an EDM vanish for one-loop , two-loop and three-loop processes [3]. Therefore its contribution to any EDM is very small, far below present experimental limits. The other **CP**-violating parameter of the Standard Model is

$$\overline{\theta} = \theta + \text{ArgdetM} \tag{1.6}$$

where θ labels the QCD vacuum and M is the quark mass matrix. $\overline{\theta}$ only contributes to **CP** violation in strong interactions, and in particular it gives a value for the neutron EDM of about $10^{-16} \sin(\overline{\theta})$ e cm. Since the experimental value for the neutron

is of the order 10^{-25} [35], this requires $\overline{\theta}$ to be extremely small. This leads to the so-called Strong **CP** problem: why would such a parameter be so small given that it is a sum of two apparently independent terms? Two main types of models have arisen to explain this phenomenon: the Peccei-Quinn (PQ) mechanism which eliminates the offending term through the creation of axions, and spontaneous symmetry breaking which requires $\overline{\theta}$ to be zero at the tree level and receive only small radiative corrections. The PQ mechanism has difficulties in that axions have severe astrophysical constraints [54] and that several searches for certain types have been unsuccessful [20],[50]. The second approach has a wide range of models, some without testable consequences, and so I will say no more about it. In any case, $\overline{\theta}$ is less sensitive to atomic EDM's than to the neutron EDM. This being the case, it would require an extremely high precision measurement for an atomic EDM to set limits on Standard Model parameters.

The situation for the various theories that extend the Standard Model is more promising. There are many such models, which introduce a plethora of potential **CP**-violating parameters. One class of theories is that of the flavor-changing models, which postulate a new boson that couples different generations of quarks (and leptons). A well-known example is the Left-Right Model (discussed in [63]), which assumes that **P** and **CP** are conserved at very high energies, but violated at lower energies due to parity asymmetry of the vacuum. The theory thus introduces right-handed partners to the W and Z (which must have a much larger mass to be experimentally acceptable), and the mixing between W_L and W_R allows for **CP** violation. The level of mixing is set by the parameter ζ, expected to be of the order 10^{-3} to 10^{-4}. This theory predicts neutron (and some atomic) EDM's at a level close to the present limits. Indeed, current data constrains the theory significantly, but the work of McKellar and his group [60] have found corrections so that it is still viable. If an EDM is measured within the next few years, this theory will be a serious contender.

Various Multi-Higgs Models also predict atomic EDM's near present experimental limits. The introduction of another Higgs doublet into the theory gives rise to terms with non-hermitian operators, and so potentially **CP** violating parameters. Probably the most important subclass of this group are the supersymmetry (SUSY) models. The introduction of supersymmetric partners such as the gluino make possible one-

loop level contributions to EDM's, meaning that they allow values more than a thousand times the present limits! Naturally such numbers are based on guesses for the phases, and various mechanisms can suppress such values enormously [3].

Table 1.1 shows the present limits on some parameters used in these theories, and mentions the measurement that determined them. The conversions from measurement to limit were obtained from [2]. Note that x_q is proportional to $\sin 2\,\zeta$.

Parameter	Limit	Source	Reference
$\overline{\theta}$	2.5×10^{-10}	neutron	[35]
x_q	5.8×10^{-3}	^{199}Hg	[44]
ε_H	$0.7/\tan\beta$	^{199}Hg	[44]
ε_{SUSY}	6.3×10^{-3}	neutron	[35]

Table 1.1: Present Limits on some parameters in **T**-violating Theories

1.4 Atomic EDM's

One or more of the mechanisms discussed in the previous section could impart an EDM to a fundamental particle or an interaction between such particles. More work is naturally required to understand how such effects extend to composite particles: nucleons, nuclei, and atoms.

The problem with using an atom is that the electrons in it will re-arrange themselves in the presence of an electric field, in such a way that all components of the atom experience no net force. L.I. Schiff has shown [78] that a system of non-relativistic charged point particles that interact electrostatically can not have an EDM, assuming that the charge and EDM distribution are the same. Note that this applies even if the individual components of an atom do possess an EDM. The various mechanisms that could generate an atomic EDM can be deduced from the exceptions to Schiff's theorem.

First of all, a relativistic treatment shows that if the electron possesses an EDM, the atom will too. This effect is dominant in atoms with an unpaired electron such as the alkalis. It is small for closed-shell atoms such as xenon in its ground state. Second, electron-nucleon interactions that are **T**-odd and **P**-odd can generate

an EDM. Two relativistically invariant forms for these interactions exist: tensor-pseudotensor interactions and scalar-pseudoscalar interactions. Third, the finite size of the nucleus means that the spatial charge and EDM distribution of the nucleus may not be the same. Thus the EDM of a neutron or proton, or **T**-odd and **P**-odd nucleon-nucleon interactions, could give rise to an atomic EDM. The difference in the two distributions is measured by the Schiff moment **Q**, defined to be [27]

$$\vec{\mathrm{Q}} = \frac{e}{10} \sum_{i=\mathrm{protons}} \left(< r_i^2 \vec{\mathrm{r}}_i > - \mathrm{R}_\circ^2 < \vec{\mathrm{r}}_\mathrm{i} > \right) \tag{1.7}$$

where r refers to the position of the protons in the nucleus and $\mathrm{R}_\circ$ is the nuclear radius. The Schiff moment, in turn, can be related to η, a dimensionless parameter which sets the strength of the nucleon-nucleon T-violating interaction. Flambaum, et al. [26], have calculated for ^{129}Xe,

$$\mathrm{Q} = 1.75 \times 10^{-8}\, \eta\, \mathrm{e\,fm}^3 \tag{1.8}$$

All of the effects mentioned above become much more prominent for heavy atoms, and so an atomic EDM tends to scale as Z^2 or Z^3. For a moderately high Z, the nuclear effects (or relativistic effects) can lead to an atomic EDM that is substantially larger than the neutron EDM (or electron EDM). For this reason atomic EDM measurements can set much more stringent limits on certain **T** violating limits than neutron EDM measurements can. The dependance on Z also means that an EDM measurement in ^{129}Xe must be more precise than one made in a heavier atom, such as ^{199}Hg, to set the same limits on **T** violating parameters.

Mechanism	Order of Magnitude
Electron EDM ($\mathrm{J} \neq 0$)	$\mathrm{Z}^3\alpha^2\mathrm{d_e}$
Tensor-Psuedotensor	$\mathrm{Z}^2\mathrm{G_F C_T}$
Scalar-Pseudoscalar ($\mathrm{J} \neq 0$)	$\mathrm{Z}^3\mathrm{G_F C_S}$
Nuclear EDM - finite size	$\mathrm{Z}^2 \frac{\mathrm{r_n}}{\mathrm{a_\circ^2}} \mathrm{d_n}$
Nuclear Magnetic Quadrupole	$\mathrm{Z}^2\alpha^2 \frac{\mathrm{m}}{\mathrm{M}} \mathrm{d_n}$

Table 1.2: Scaling of **P**,**T** odd effects in atoms.

Note that $\mathrm{C_T}$ is a dimensionless parameter measuring the strength of the tensor-pseudotensor interaction, and $\mathrm{C_S}$ is the analogous parameter for the scalar-pseudoscalar

interaction. The nuclear quadrupole effect was not mentioned earlier because it only applies to atoms with $I \geq 1$.

Several different theorists have gone beyond this order of magnitude estimate and predicted quantitative values for these coefficients. From these, an expression for d_{Xe} can be found.

$$d_{Xe} = 10^{-3} d_e + 5.2 \times 10^{-21} C_T + 7.5 \times 10^{-23} C_S + 4.7 \times 10^{-26} \eta \qquad (1.9)$$

where the coefficients were determined by Khriplovich [48], Martensson-Pendril [63], Khriplovich [47], and Flambaum [26], respectively. Such coefficients are generally determined to perhaps 30%, given the complicated theory involved.

Presented in table 1.3 is a list of the current limits set on these effects by other experiments. Also provided are the previous best measurements of an EDM in an atom and in ^{129}Xe in particular. The values for d_e and d_{Xe} are at the 68% confidence level, while the others are at the 95% confidence level.

Parameter	Limit	Source	Reference
d_e	4×10^{-27}	Tl beam	[16]
η	1.6×10^{-3}	^{199}Hg	[44]
C_T	1.3×10^{-8}	^{199}Hg	[44]
C_S	7×10^{-7}	^{199}Hg	[44]
d_{atom}	8.7×10^{-28}	^{199}Hg	[44]
d_{Xe}	1.4×10^{-26}	^{129}Xe	[88]

Table 1.3: Some Current Limits on **T** violation and Atomic EDM's

Inserting these values into equation 1.9 above yields an indirect limit on d_{Xe} of about 2×10^{-28} e cm. The uncertainty in this number comes primarily from the calculation of the coefficients, and so is difficult to determine [3], but this does provide an estimate of how good an experimental measurement in ^{129}Xe must be to provide new information.

CHAPTER II

The Experiment

2.1 Overview

This section outlines the method used to make a ^{129}Xe EDM measurement in this system. By definition, any system possessing an EDM will have two distinct energy eigenstates if placed in a non-zero static electric field. When a noble gas atom with nuclear spin one-half is placed in a magnetic field, the magnetic sublevels of the ground state split, giving an energy difference $2\ \vec{\mu} \cdot \vec{\mathrm{B}}$. This is referred to as the Zeeman effect. Applying an electric field causes the energy levels to shift further, each by an amount $\vec{\mathrm{d}} \cdot \vec{\mathrm{E}}$. The difference in the energy between when the electric field is antiparallel to B (labelled E2) versus when it is parallel (labelled E1) is thus $4\ \vec{\mathrm{d}} \cdot \vec{\mathrm{E}}$.

To obtain a good measurement of d, it is essential to control B to extremely high precision: otherwise shifts in the magnetic field will mask any shifts due to the electric field. This is the reason for using two noble gas species. The second species acts as an *in situ* magnetometer to compensate for drifts in B (see section 4.1 for details). The helium's own EDM shift will be negligible in comparison with that of the xenon (recall that an atomic EDM is expected to scale as Z^2 or higher).

To observe the energy difference of the atomic states, it is necessary to polarize the atoms so that their spins line up with the magnetic field. This is done by optically pumping rubidium vapor, which then transfers its polarization to the noble gases [91], [96]. Next the noble gas spin ensembles are tipped off the magnetic field axis. The spins then experience a torque and begin precessing at the frequency corresponding

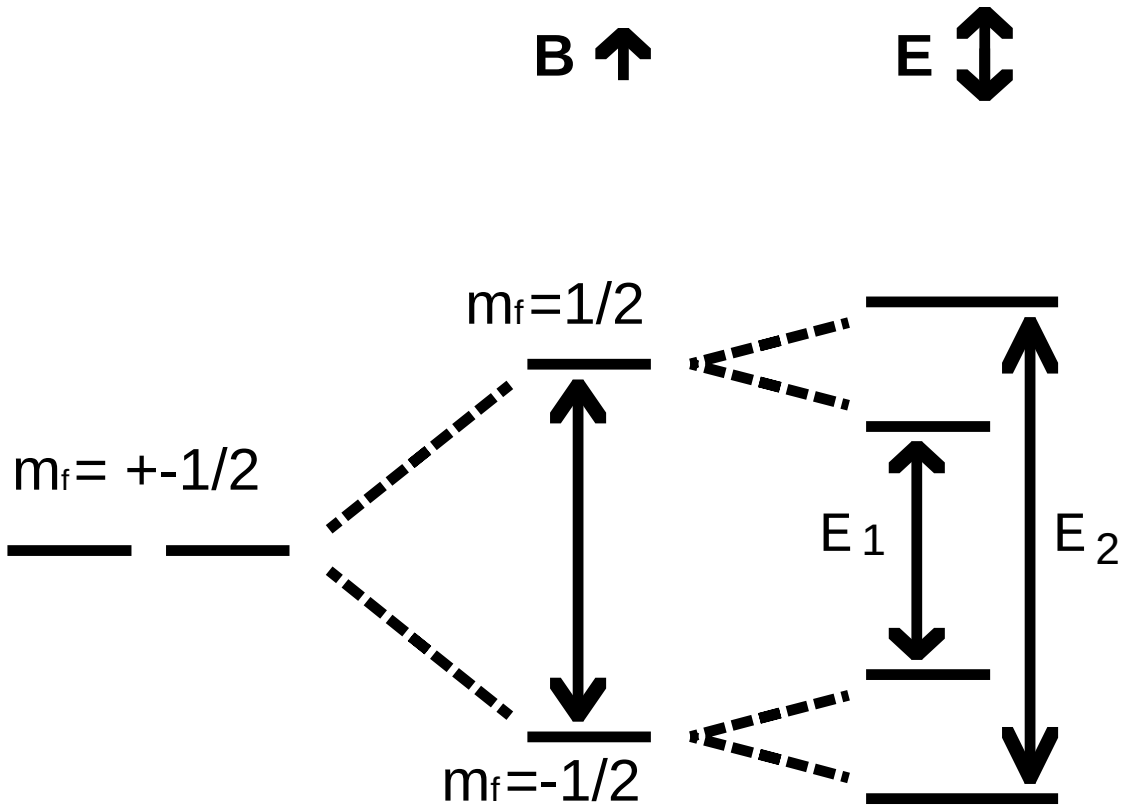

Figure 2.1: The transition energy changes 4 $\vec{d} \cdot \vec{E}$ when the electric field is reversed

to the energy difference. A "pick-up" coil of wire is placed near the atoms, in order to measure the current induced by the changing magnetic field of the precessing atomic spins.

If the resonance of the pick-up coil is very different from the atomic frequency, the amplitude of the observed signal gradually decays (this is free-induction decay, or FID). This is because atoms at different fields precess at different rates, so the phases of the spins at different positions spread out until the net signal cancels. Therefore the time constant of the decay, referred to as T_2, is usually set by the magnetic field gradients across the cell. However, I can tune the resonance of the pick-up coil to match the frequency of the atomic precession, and thus couple the circuit to the spins. This provides feedback to the system, and maintains the spin coherence for a longer time. Given good coupling between the cell and the coil, and sufficiently high noble gas polarization, the system passes beyond a threshold point and becomes a

maser [74], [73].

The advantage of the maser is that it allows extremely long run times (months). This makes possible very precise measurements of the atomic frequencies. Since the atomic polarizations are theoretically constant, they will not change the magnetic fields and cause frequency shifts. Such shifts were the dominant source of uncertainty in a previous version of this experiment [68]. To obtain masing in both helium and xenon simultaneously is a significant technical challenge, since the two species have different criteria for signal optimization. The solution is to use cells with two separate regions connected by a transfer tube. The first region is a pump bulb where the atoms are polarized; the second is a maser bulb where the masing occurs.

The last step in the procedure is to apply an electric field to the cell while observing the maser frequencies. Data is acquired for a fixed length of time, and then the electric field direction is reversed. Periodically a scan with no electric field is run, as a calibration. About once a day the sets are saved and analyzed while data acquisition continues. The data is corrected for long-term drifts or systematic effects, and then the string variance of the frequencies are calculated to reduce the effects of short-term drifts. From this, the EDM for the run is obtained. The final, reported value is the weighted average of the individual runs.

2.2 The Apparatus

Generating a maser requires a number of different components; a source of polarized light, a cell with the appropriate gases, a uniform magnetic field, and a detection system. To measure an EDM, high voltage is needed as well. Some of these systems, such as the magnetic field and the cell temperatures, require separate control loops with corresponding electronics. The details of these pieces of the apparatus are explained in the following sections; refer to figure 2.2 for a visual overview.

2.2.1 Magnetic Fields and Shielding

A Zeeman maser is very sensitive to magnetic fields and magnetic field gradients. The use of magnetic shielding isolates the maser from effects of the Earth's field or other experiments taking place nearby. The shielding is made of mu-metal, and

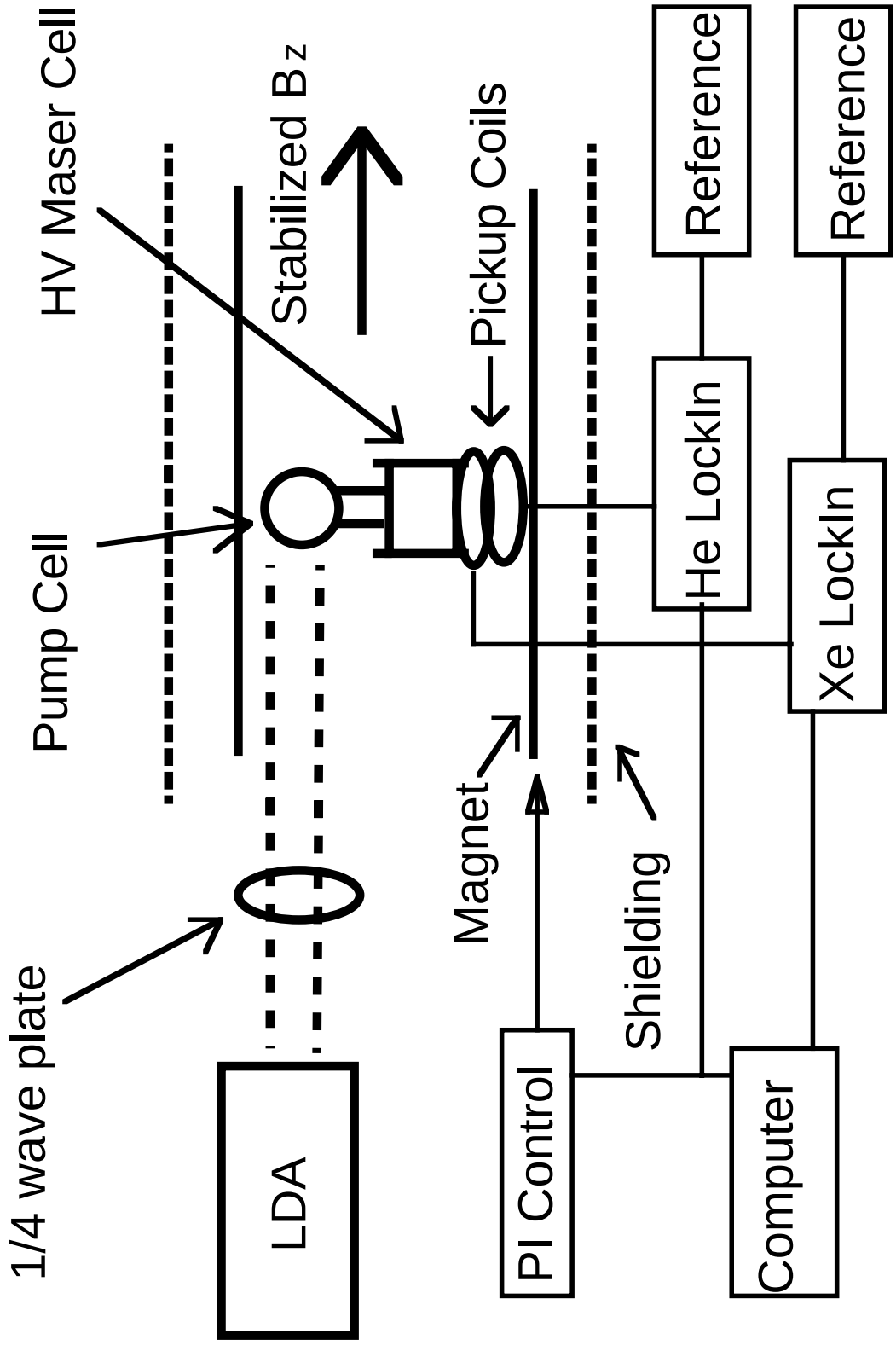

Figure 2.2: Simplified Schematic of EDM Measurement Apparatus

is shaped into three layers of cylinders. The ends of the cylinders are partially but not completely capped, so as to permit laser light, etc, to reach the cell. The shielding is much more effective in the transverse direction than the longitudinal, with measurements putting the transverse shielding factor at 125,000 and the longitudinal at 25,000. Furthermore, since one side of the shields is capped more thoroughly than the other, the oven is actually placed slightly asymmetrically in the shields, being a little closer to the better capped end.

Over time, the magnetic domains within the mu-metal will align themselves along the local magnetic field. This causes the shielding to generate a small magnetic field that gradually changes. To minimize this effect, the shielding needs to be degaussed on a regular basis. A large magnetic field is used to saturate the domains in the shielding. The applied field is then reversed, and the magnetization of the shielding follows it back, forming a hysteresis loop. By gradually reducing the applied field, the magnetization of the shielding becomes progressively smaller until it is nearly zero. The rate of reversal must be low enough that the skin depth of the shielding exceeds its thickness. In practice, the degaussing field is obtained by running a current at 0.5 Hz though the solenoid for three minutes, with a maximum amplitude of 2.5 A.

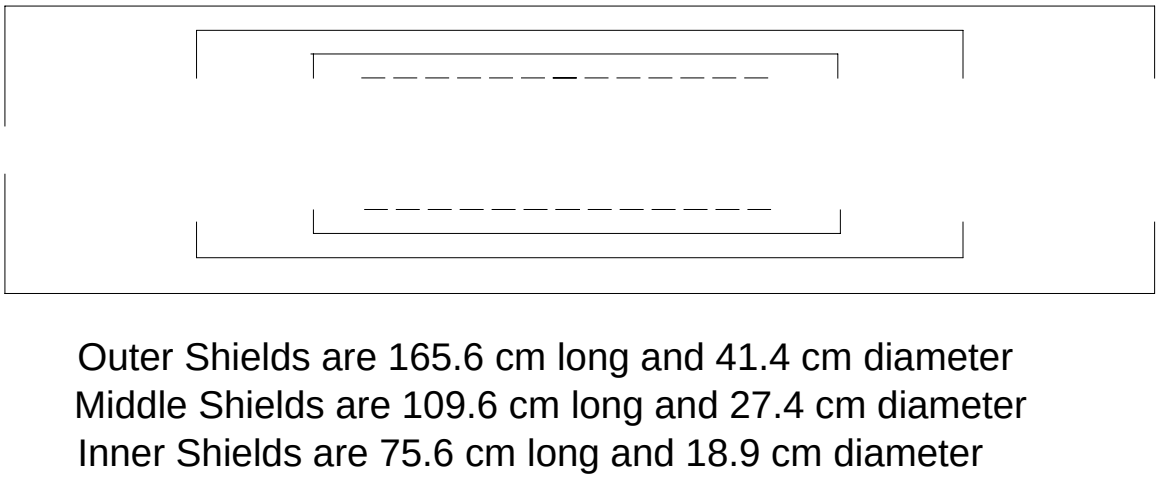

Figure 2.3: Dimensions of solenoid and shielding

Within the shields is the solenoid, which provides a magnetic field of 3.1 gauss. The solenoid used is 61 cm long and 18.4 cm diameter, and is double wrapped

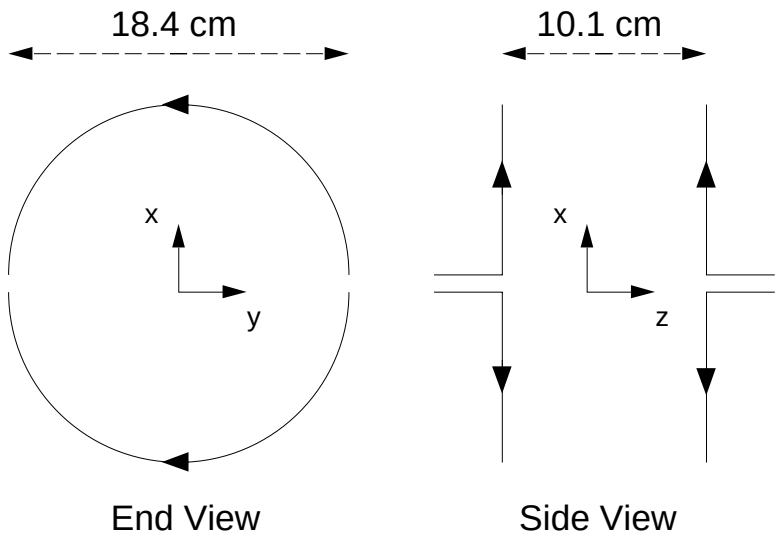

Figure 2.4: C-coil design for $\frac{\partial B_z}{\partial x}$ trim coil [68]

to reduce effects of wire pitch. The wire used is 25 AWG, giving about 20 turns per centimeter for a single layer. It requires 64.5 mA to generate the correct field strength. Five centimeters of additional turns are located at each end of the solenoid: these are also double-wrapped. These end corrections can be independently adjusted to provide a more uniform field (refer to figures 2.5, 2.6). There are also three trim coils to reduce the gradient of B_z along x, y, and z, also wrapped on the outside of the magnet. The $\frac{\partial B_z}{\partial z}$ trim is just an anti-Helmholtz coil, whereas the other two trims use a C-coil design (refer to figure 2.4). All three trims have the same separation, 10.1 cm.

Field gradients are crucial because they set the limits on the coherence time for an ensemble of precessing spins, as mentioned previously. For the cylindrical maser bulb (oriented along the z axis), in the high-pressure limit, where L is the cylinder length, a is its radius, and D the diffusion constant [61]

$$\frac{1}{T_2} = \frac{L^4\gamma^2}{120D}\left|\frac{\partial B_z}{\partial z}\right|^2 + \frac{7a^4\gamma^2}{96D}\left(\left|\frac{\partial B_z}{\partial x}\right|^2 + \left|\frac{\partial B_z}{\partial y}\right|^2\right) \tag{2.1}$$

For this experiment, L = 2 cm, a = 0.64 cm and D = 0.69 cm^2/sec for He, D = 0.14 cm^2/sec for Xe (see table 3.1). This equation also provides a rough estimate of the longitudinal magnetic field gradients: about 40 μGs/cm under running conditions. Refer to section 3.4 for further comments on T_2.

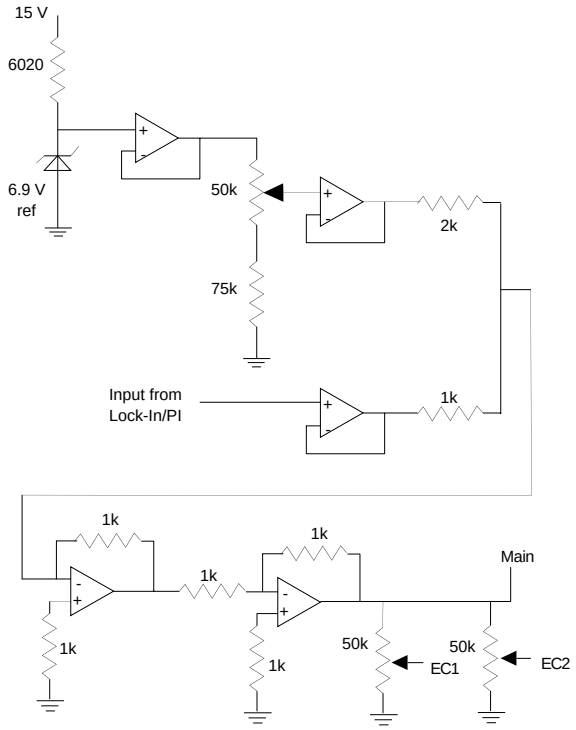

Figure 2.5: Magnet Control Circuit Part One: Determining Proper Voltage

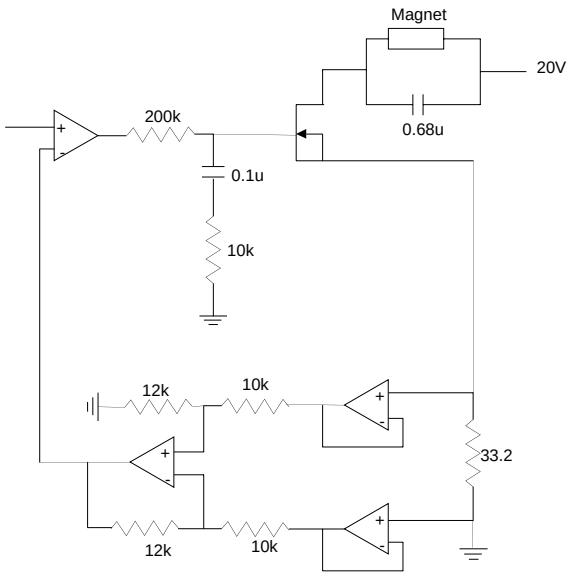

Figure 2.6: Magnet Control Circuit Part Two: Main Feedback Loop (End Correction Loops are identical)

In order to insure a stable magnetic field during data taking, a feedback loop is employed (see figures 2.5,2.6). One of the species, typically xenon, has its maser output compared to a reference frequency. The Ithaco 393 lock-in [41] that does this acts as a phase-sensitive detector, outputting .01 V per degree of phase difference (more details are given in section 2.2.4 below). Since the maser signal out of the pre-amp is generally about 25 mV (refer to section 2.2.4 below), the Ithaco sensitivity is set to 30 mV to obtain optimum performance. The Ithaco's time constant is 4.0 msec: any longer tends to break the lock-loop. The output of the lock-in is sent on to a home built proportional-integral (PI) circuit with a proportional gain around .1, an integrator time constant typically set to .3 sec, and a filter of 0.03 Hz. The result is then sent back to the magnet control circuit, which sums in the difference to adjust the main current and end corrections. The correction voltage is generally about 0.5 mV, and varies by around 0.1 mV in a typical 24-hour period.

2.2.2 Light

Polarizing the atoms requires a source of light at the rubidium D1 resonance line, 794.7 nm. During data collection, either one or two Opto-Power laser diode arrays (Model: OPC-A015-FCPS) [67] or a single Coherent laser diode array (Model: FAP-I) [15] were used, depending on what was available. The Opto-Power units each provide about 15 watts of power, whereas the Coherent provides 30 watts. These arrays have a broad and irregular profile, with a FWHM over 1 nm (see figure 2.7), but they require essentially no maintenance, being simple turn-key units.

The Coherent laser is more stable than the Opto-Power units in several respects. First of all, the overnight drift in the laser beam power is 0.1% for the Coherent but 0.3% or more for the Opto-Powers. The Coherent may also have a more stable frequency, though this is hard to measure. However, I have observed that substantial changes in the room temperature of the laboratory can move the Opto-Power lasers completely off resonance, while Coherent has never been so affected. It is not entirely clear if this difference is attributable to superior manufacturing or the relatively old age of the Opto-Power units. Chapter Six describes a system to improve the control of the Opto-Power units, thus greatly reducing their drift.

The output of each laser passes through an AR coated lens to collimate it, then a

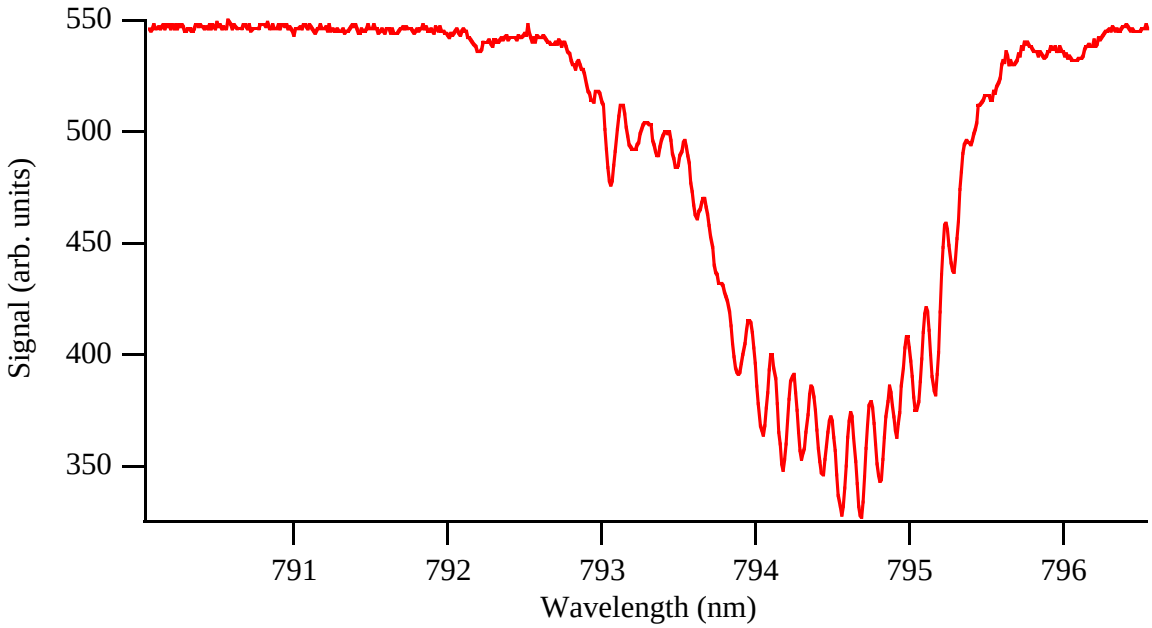

Figure 2.7: Typical Profile of the Opto-Power diode laser array. Rb resonance is at 794.7. The Coherent is similar.

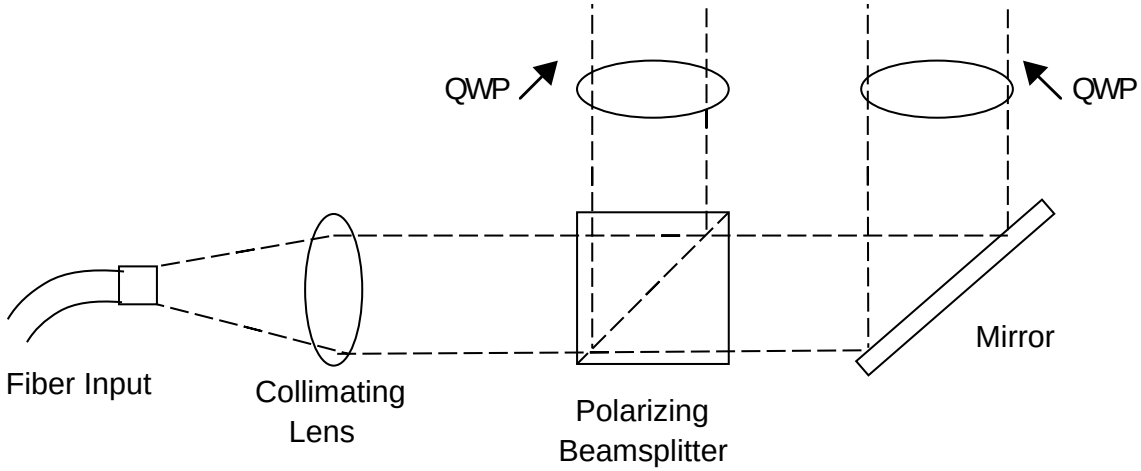

Figure 2.8: Optics for a laser diode array beam

polarizing beamsplitter, and then quarter wave plates to circularly polarize the light. Since the two output beams of the beamsplitter have different linear polarizations, the two quarter wave plates must have perpendicular axes. Note that the polarization of the initial laser diode array beam is a sensitive function of the temperature and mechanical stress placed on its output fiber. As this polarization changes with time, the relative power of the two circularly polarized beams also changes. Although nominally the total power delivered to the cell is constant, the differences in quarter wave plate orientation or beam steering may have some effect on the cell polarization.

The circularly polarized beams then shine into the upper chamber of the cell. Presumably about 8% of the power is lost at the oven window; another 14% of this light is reflected from the front face of the cell and lost. A further 8% is lost if the laser beam powers are monitored, using a set of microscope slides that pick off part of the beams.

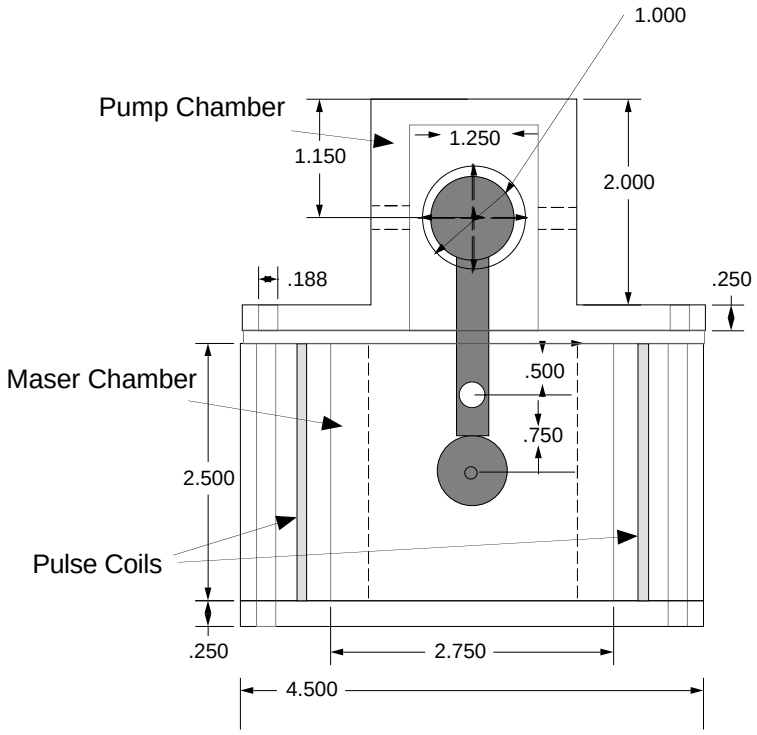

Figure 2.9: View of the oven parallel to shields. Cell position is shaded. Measurements are in inches.

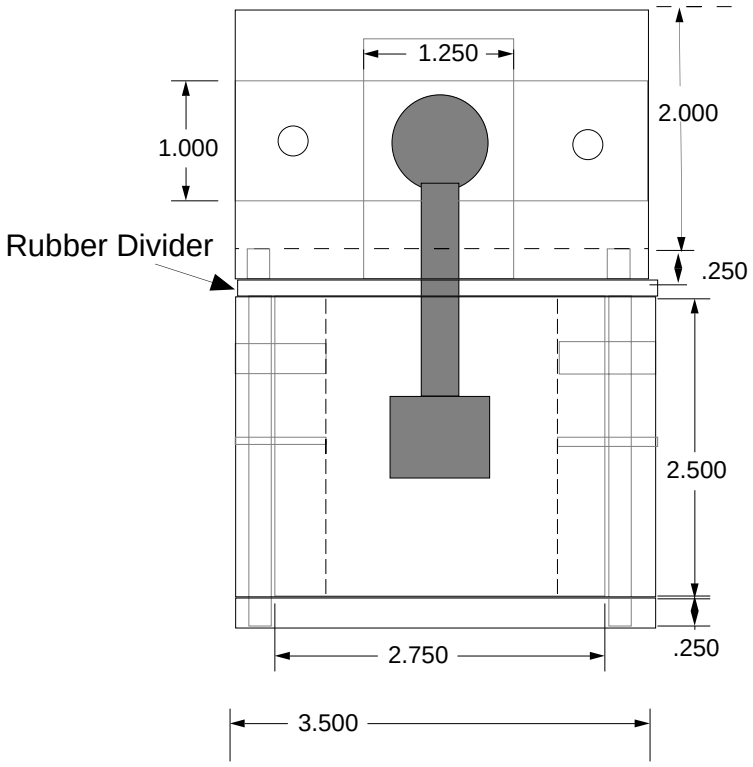

Figure 2.10: Side view of the oven. Cell position is shaded. Measurements are in inches.

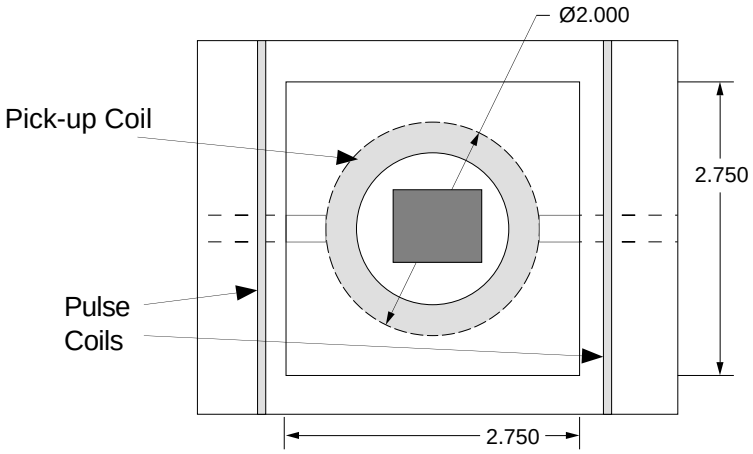

Figure 2.11: Bottom view of the oven (maser chamber only). Cell position is shaded. Measurements are in inches.

2.2.3 Oven and Cell Temperature Control

The cell sits within a nylatron oven, whose dimensions are given is figures 2.9, 2.10,2.11. Nylatron is a nylon-molybdenum-disulfide composite that is nonmagnetic and easy to machine. It can tolerate the temperatures used in the system, though it will melt if directly exposed to the high powered laser light for a substantial period of time. The function of the oven is to provide the structural framework for the cell, and for the pulse and pick-up coils described below. The oven has two chambers (separated by a silicone rubber stopper 0.125" thick) to provide different temperatures for the pump and maser bulbs. These two chambers are physically distinct pieces that must be separated to remove or insert a cell. The maser chamber piece is further subdivided into an outer block, an inner block, and a bottom plate. The outer block makes the connections to pumping chamber, the airflow, etc., and provides the form for the pulse coils. The inner block provides the structural support for the pick-up coils, enabling these to be removed from the oven without straining the wires. The bottom plate is removed to observe the cell while the high voltage tabs (refer to section 2.2.5) are pressed into position.

The oven rests in a cradle which conforms to the shape of the solenoid's bore. The vertical position actually fixes the maser bulb about 1 cm below the axis of the solenoid. This offset partially compensates for the gradients caused by polarized atoms in the transfer tube.

Temperature control of the two oven chambers is achieved with a flowing air system: heated air warms the pump chamber and cooler air cools the maser chamber. Note that the laser beams also contribute substantially to the heating of the pump bulb. The pump bulb is heated to 120°C to obtain a reasonable rubidium vapor pressure. The density can be estimated using Killian's formula (T being temperature in Kelvin, [Rb] given in cm^{-3})

$$[\mathrm{Rb}] = \frac{10^{(10.55-\frac{4132}{\mathrm{T}})}}{1.38 \times 10^{-16}\,\mathrm{T}} \tag{2.2}$$

giving us a density of 2.0×10^{13} cm^{-3}. Computer simulations have shown that the helium favors high rubidium densities (temperatures of 180°C and above) , whereas the xenon polarization is a relatively weak function of temperature from 110 to 160°C, with a maximum near 140. At higher temperatures, the rubidium is the dominant

mechanism for the xenon's longitudinal depolarization. However, the lifetime of the cells is determined by how quickly the rubidium is driven out of the pumping region (refer to section 2.2.6), and so the lower temperature of 120°C is felt to give the best results over the long term. The polarized noble gases diffuse down to the maser bulb, which is kept cool (40 °C) to greatly reduce the rubidium vapor density and so extend the xenon polarization's lifetime.

Temperature control is important in obtaining the needed maser stability. One disadvantage to the two-bulb cell design I use is that the densities in the two bulbs are different. At 120/40 °C, a 1 °C change in the pump temperature leads to a 0.15% change in density in the masing region; a 1 °C change in maser temperature gives a 0.18% change. This can be important because the radiation damping and the magnetic fields created by the atomic species depend directly upon density: a full explanation is given in the Chapter 4. Temperature changes can also affect T_1 and T_2 through changes in the wall interactions or diffusion constants.

The original set-up for maintaining the oven temperatures used Omega Omron controllers with a flowing air system [66]. These units were very convenient to use, and maintained a temperature stability of 0.1 K rms over many hours. However, it became necessary to further improve the control, which led to the construction of separate PI controllers to replace the Omron units (see figure 2.12). These use the input from a three-lead platinum 100 ohm RTD set within the appropriate chamber as part of a bridge circuit. The resulting error signal is sent to a PI control circuit. The output current of the circuit goes to an Omega PCM-1 device This device is attached to solid-state relay that gates line power, with the PCM ensuring that the outlet's output power is proportional to the PCM's input current. An 800 W heater is plugged in to the aforementioned outlet, and this is used to heat the incoming air. All bridge resistors in this control circuit have temperature coefficients of less than 5 ppm/°C, and it also proved important to use high stability op-amps. This led to control at a level of 10-20 mK rms in the maser chamber, but only 60-70 mK rms in the pump chamber. The temperature is monitored separately from the control system, although the monitor RTD's were located very close to those used by the control circuits. Indeed the location of the RTD's is a tricky business, because of the effects of the laser beams on the pump bulb temperature. If the RTD's were placed

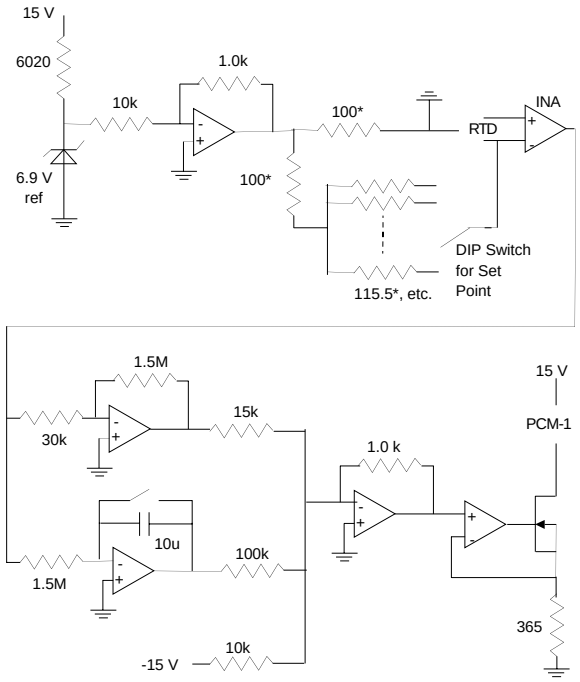

Figure 2.12: Maser Temperature Control Circuit. Pump Circuit has same form but different values. Resistors with an * are 5 ppm/°C

in the laser beam, it is doubtful that they would absorb the same amount of heat as the cell. However, the poor thermal conduction of the glass means that if the RTD's are outside the beam they may not measure the temperature of the cell gases very accurately. It is felt that the best position for the pump chamber RTD's are on the pull-off of the cell (see figure 2.18), just out of the laser beam. The uncertainty this introduces in the measurement of the cell's absolute temperature is neglected.

The temperature control system includes pressure control of the incoming air. Pressure regulation is achieved using an Omega PX236-100G pressure transducer to sense the pressure just above the heaters. The transducer's output is fed to a PID control loop with an overall proportional gain of 2158, an integration frequency of 0.12 Hz and a differential frequency of 1.59 Hz (see figure 2.13). The output of the control circuit is sent to an MKS Type 248 Control Valve to moderate the flow rate [62]. Vibration within the maser chamber is an important source of noise, so it is important to limit the air flow through that chamber to the minimum necessary for cooling.

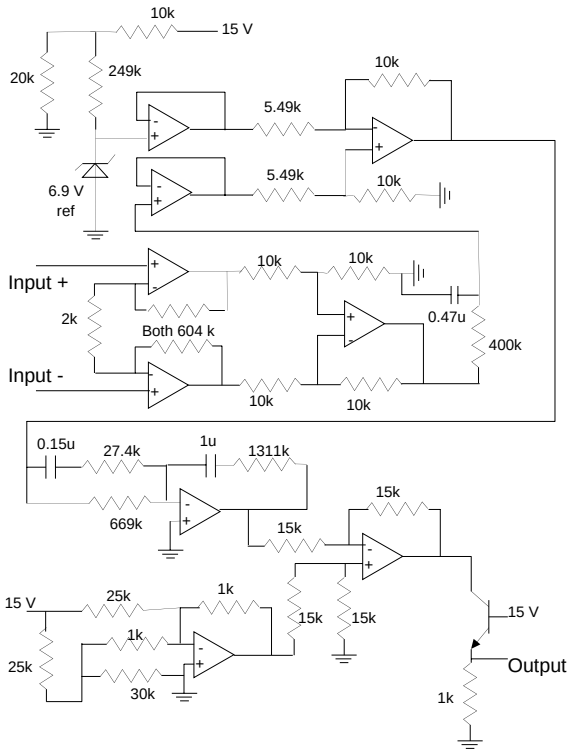

Figure 2.13: Pressure Control Circuit

2.2.4 Creating and Observing Spin Precession

The polarization of the noble gases can be tipped away from the magnetic field axis by use of a pulse coil. This is not necessary for the masers, which will spontaneously build up (from background noise) when the system is on-resonance. However it is necessary when the system is off-resonance, in order to determine the rate constants of the cell (refer to section 3.6). The pulse coils consist of two rectangular 3.5" x 2.5" coils, each with three turns of wire, spaced 3.12" apart and centered on the maser bulb (see figures 2.9,2.10,2.11). The coils are oriented to generate a magnetic field transverse to the solenoid axis, When a signal is desired in FID work, the computer outputs a 50 millisecond pulse. This turns on the output of our frequency synthesizers and blanks off the pre-amplifiers. The frequency synthesizer outputs tend to be slightly on all the time, so the computer pulse also controls an additional gate after this output. Even this gate does not completely eliminate the bleed-through, so the pulse driver circuit is disconnected for maser running. The synthesizer outputs are typically 0.1 Vpp for Xe and 0.05 Vpp for He, resulting in a

tip angle of 4 degrees for Xe and 6 degrees for He (away from the z axis). The size of this tip is a compromise between obtaining a clear signal and maintaining the same longitudinal polarization.

The spins then begin to precess around the z axis. This precession can be observed via the current induced in pick-up coils located next to the cell. There is one coil for each species, each encircling the maser bulb and aligned with the transfer tube. There is a 0.16" gap between the coils so that screws can pass between them, in order to press the high voltage tabs firmly against the cell. Each coil is made from 3550 turns of 38 gauge wire on a form with inner diameter 1.52", an outer diameter of 2.00" and a thickness of 0.36". The Q of the He circuit is about 29; the Q of the Xe circuit is 14. Calculations put the geometrical filling factor $\eta' A = 0.53$ cm^2. Naturally the two coils are coupled, with their mutual inductance estimated to be 0.23 H. (Self-inductances when the oven is in position are about 0.6 H)

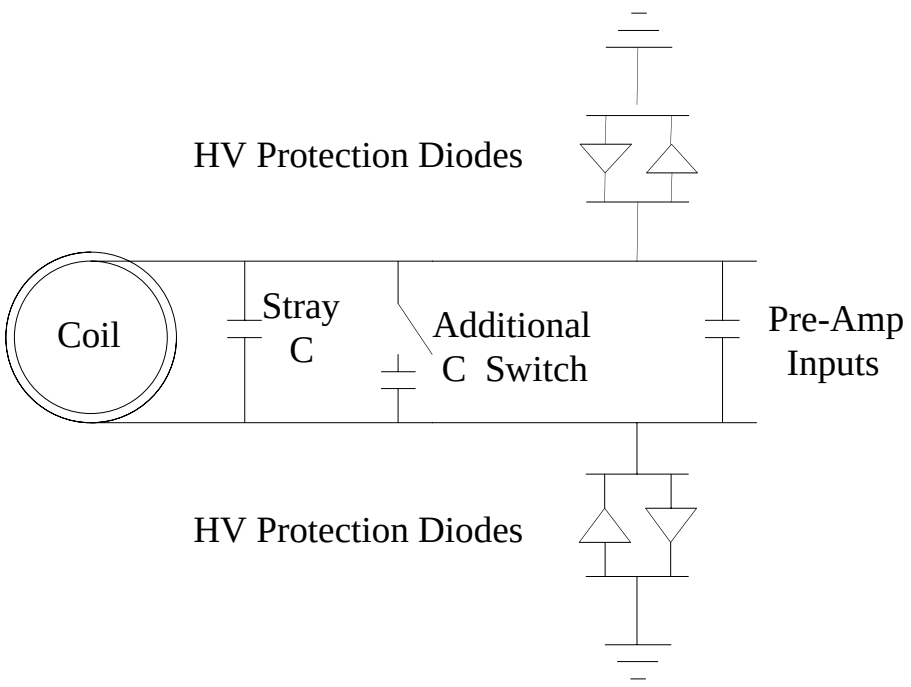

Figure 2.14: Schematic of Pick-up Coil circuit

The pick-up coils are connected through semi-rigid coax wires to a resonance box. The stray capacitance of the wires is about 150 pF, and the pre-amps (mentioned below) contribute an additional 25 pF. The resonance box contains a switch for each species that allows additional capacitance to be summed in. This changes the

resonant frequency of the pick-up coils, either matching them closely to the atomic frequencies or placing them several kHz away in the "off-resonance" state. 2470 pF is added to the Xe on resonance, and 200 pF to the helium. Obtaining the correct ratio of coil resonances (2.754, the ratio of the atom's nuclear magnetic moments) is a tedious procedure in light of the strong mutual inductance. All capacitors used are type C0G (30 ppm/°C) to reduce the drift in the coil resonance frequencies with temperature. (See Chapter Four for a discussion of cavity pulling effects.) The resonator circuits also contain 1N914 diodes, to protect the preamps in the event of high voltage breakdown through the coils. (Refer to figure 2.14.) The diodes are replaced if the system consistently has stability problems with the high voltage running.

Next the signals are passed through the SR560 pre-amplifiers. These are manufactured by Stanford Research Systems [84]. To eliminate the presence of 60 Hz harmonics, it proved necessary to run the pre-amps on an external DC power supply rather than use line power. The pre-amps are set to a gain of 1000, and have high-pass and low-pass filters, each at 6 dB/oct and set a factor of 10 away from the atomic frequency.

The capacitor box temperature control system, completed August 11, 1999, encloses the resonance box and the pre-amps in a box of styrofoam sheeting. The box temperature is kept at 29 °C to insure reasonable control. The system is simple: two 5 Ω, 25 W resistors are attached to the resonance box in series, while a 3 kΩ thermistor measures the temperature. The control circuit outputs up to 0.3 A, corresponding to a maximum power output of 0.9 W. If turned on at room temperature the box requires about 12 hours to equilibrate, but thereafter it remains quite stable, with variations of 5 mK rms. The control circuit for the current delivered to the resistors was very similar to the one for the oven temperature control given in figure 2.12.

From the preamps, the signal is passed to the SR850 lock-in's (also made by SRS). The lock-ins extract the beat frequency between the atomic signal and a reference set by SRS model DS345 frequency synthesizers. To do so, the lock-in multiplies the two sine waves and passes the result through a low pass filter. At this point the

lock-in signal is given by

$$\begin{aligned} V_{psd} &= V_{sig}\ \sin(\omega_{sig}\,t + \theta_{sig})\ V_{ref}\ \sin(\omega_{ref}\,t + \theta_{ref}) \\ &= \frac{1}{2} V_{sig}\, V_{ref}\ \cos((\omega_{sig} - \omega_{ref})\,t + (\theta_{sig} - \theta_{ref})) \end{aligned} \tag{2.3}$$

This technique for extracting the signal at a specific frequency is called phase-sensitive detection [83], because if the two frequencies are identical, the size of the output signal depends on the relative phase of the two waves. Using a control circuit, the relative phase can therefore be held at zero. This is "phase-locking", and the control system is therefore called a phase-locked loop. The circuit to control the magnetic field (refer to section 2.2.2) is an example of this.

All the frequency synthesizers used are externally locked to the (internal) reference of an SRS model FS700 Loran-C frequency standard box to synchronize their outputs. The beat frequency is set to be 25 mHz; the lock-ins have a 12 dB/oct low pass filter with a 1 second time constant, giving a bandwidth of .125 Hz. For maser runs the lock-ins sample the data at .5 Hz (generated by an HP3325B frequency synthesizer, manufactured by Hewlett-Packard [40]). The sample rate is therefore more than twice the bandwidth, as required by the Niquist criterion.

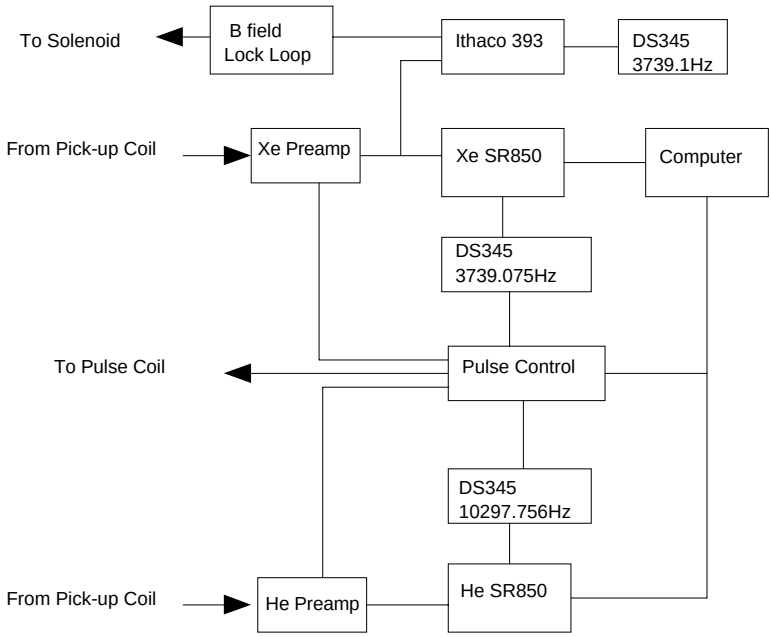

Figure 2.15: Signal Detection Subsystem

The lock-ins store two beat waves which have a 90° phase difference. The data is

then downloaded onto the data acquisition computer, a Mac IIci, using GPIB. Here a macro in Igor Pro 3.0 (produced by WaveMetrics [94]) combines the two waves into a continuously increasing phase. Another macro performs a least squares fit to the phase line to extract the frequency of the atomic resonance. The programs to tip the magnetic field and read the free induction decay (when not masing) and to degauss the shields are written as Igor external operations (XOP's). The Igor Pro macros enable data taking to be completely automated.

2.2.5 High Voltage

The electric field across the cell is generated by two Glassman high voltage supplies of type MJ30 [31]. Each can generate up to 30 kV and a maximum of 400 μA, with one supply wired for positive voltages and the other for negative. These then run into Kilovac high voltage SPDT relays that can handle up to 35 kV [53]. The Kilovac relays are given 20 V to insure switching, and are themselves controlled by computer output through a solid-state relay (refer to figure 2.16). From each relay comes an insulated wire that passes through a low-pass filter (a 1.5 MΩ resistor and a 3.3 nF high voltage capacitor). The filter reduces the 55 kHz noise output by the Glassman supplies from 50 mV to 130μV (at 4 kV/cm). Without the filters, the maser stability with the electric field on is a factor of two worse than with the field off.

After the filter the high voltage wire runs through a connector, and then to the oven. At the oven, the wire is run through the bottom plate of the maser chamber and up to the cell. Each wire then ends in a brass tab, cylindrical with a diameter of 180 mils and a thickness of 120 mils. The edges are carefully rounded, and a cone-shaped depression drilled into the back permits the tab to be pressed tightly against the cell with a 4-40 nylon screw. This design provides structural support as well as the potential difference needed. Considerable effort went into optimizing a design that gives the best possible coupling for the coils while still keeping them a safe distance from the tabs and the cell endplates. Typically one plate was set to 3.6 kV and the other -3.6 kV. Given the cell length of 2.0 cm, this gives a 3.6 kV/cm electric field. Sometimes slightly larger values of the field (3.75 - 4.0 kV/cm) were used instead. The cell can tolerate a higher field, but the larger fields caused bursts

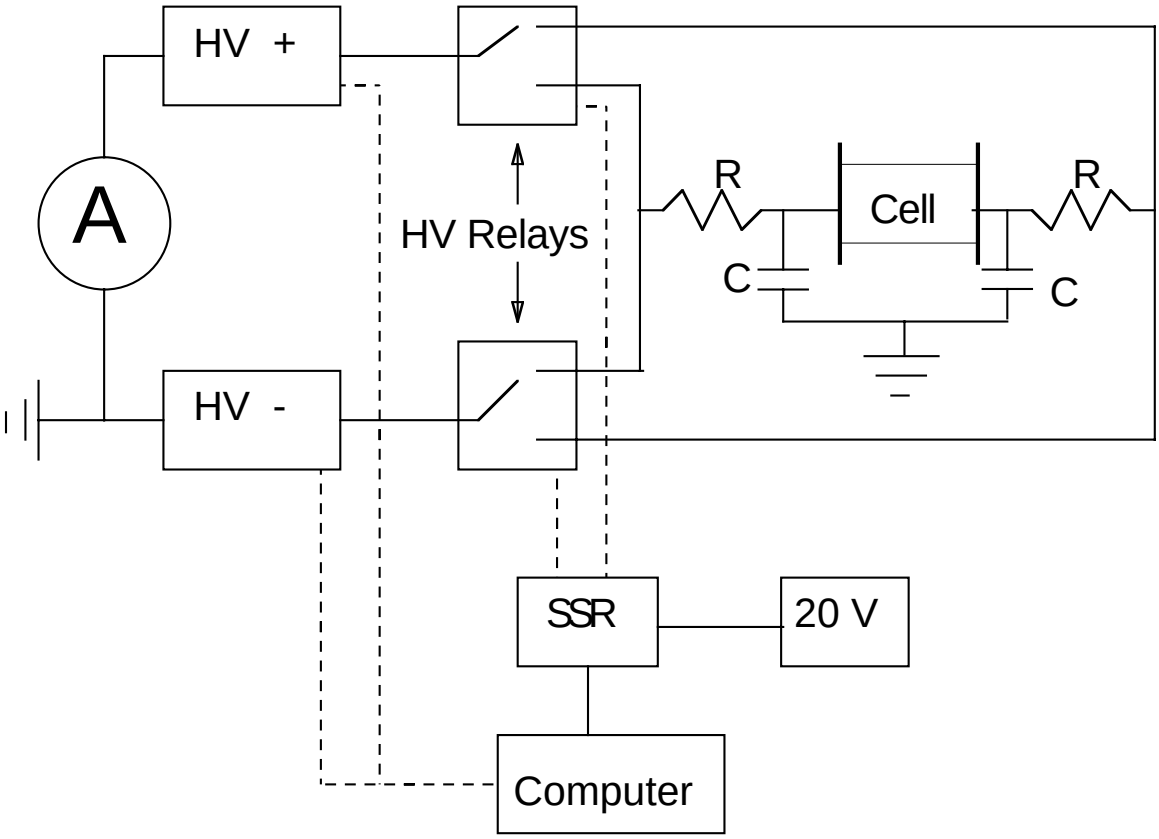

Figure 2.16: High Voltage Sub-system

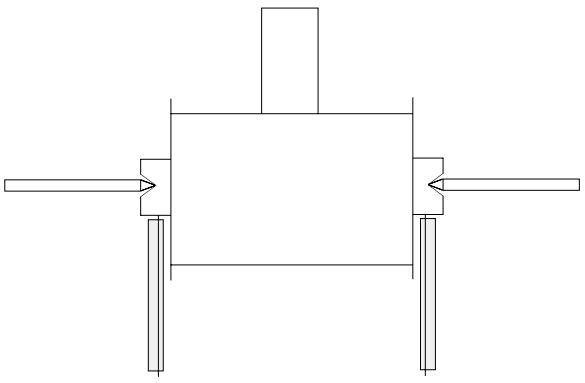

Figure 2.17: Side view of HV tabs pressed against the cell endplates

of noise as some kind of discharging occurred. At higher fields, these noise bursts can briefly overwhelm the maser signals, causing the magnet lock loop to fail and drive the magnetic field well away from the coil resonances. Occasionally a particularly nasty discharge would even damage the pre-amps used to observe the maser signals, despite their protective diodes. Fortunately, replacing the input FET (a NPD5564 chip) usually sufficed to fix the problem.

The leakage current is measured with a Keithley 614 electrometer [51], whose output is then recorded by a Fluke [29] multimeter. I chose to keep the negative supply at ground for safety (the Glassman supplies should not float more than 300mV from ground). The program input for the Glassman supplies runs through a 330 kΩ resistor to ground, which shows up as a leakage current of several microamps. To avoid this problem, an AD210BN chip is used as an optical isolator to prevent a current in the positive supply's program input. The high voltage supplies were controlled through the auxillary outputs of an SR830 lock-in, while the relays were controlled by a digital I/O on the computer's National Instruments board.

In this set-up, the measured leakage current includes all paths from the positive Glassman output to ground. It therefore includes current through the capacitors in the low-pass filters, or from the positive cell endplate to ground directly to ground, in addition to the current through the maser bulb. The measured value is still sufficient to set an upper limit to the leakage current, which is all the experiment requires. A typical measured leakage current is about 200pA, though some were larger or smaller. The leakage current is measured on top of an offset of about -1 nA: the origin of this offset is unclear, but may be related to improper impedance matching of the Keithley input. In any case, the offset is present with the high voltage supplies completely turned off, and so it is clearly not related to current passing through the cell. A more complete description of the leakage current is given in sections 4.2 and 5.3

2.2.6 Cells

The EDM cell used in the experiment (E17) consists of a spherical pump bulb, a narrow transfer tube, and a cylindrical maser bulb. This cell is made of Corning 7056 glass, which is a borosilicate glass with a helium permeability of 1.8×10^{-11} (cm^3 mm)/(sec cm^2 torr) at 120 °C, a thermal expansion of 5.1×10^{-6} in/in/°C, and

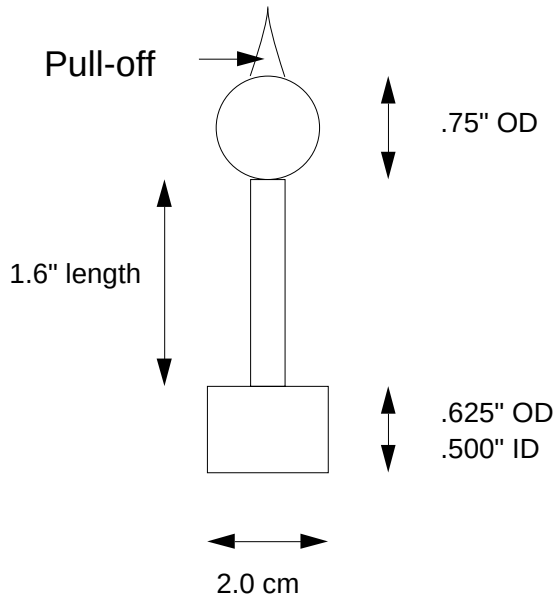

Figure 2.18: EDM Cell Dimensions

a volume resistivity of about $6 \times 10^{18}\,\Omega$ cm at 40 °C. The pump bulb is spherical, blown from 8mm OD heavy wall (2mm thick) tubing. The pump bulb has a volume of about 3.5 cm^3 , measured in several failed cells. A 1.6" length of glass tubing connects the pump bulb to the maser bulb. The ID of the tubing is .325 cm and so a transfer tube volume is 0.34 cm^3. The maser cylinder is just a piece of cut tubing: it is 1.979 cm long and its volume is 2.5 cm^3. The ends of the maser bulb are flat, thin (.004") plates of molybdenum. All of the glass is coated with octadecatrichlorosilane to improve the xenon longitudinal polarization lifetime [68].

The cell contains rubidium, xenon, helium, and nitrogen. Since the cell has two regions at two different temperatures (pump temperature 120 °C, maser temperature 40 °C), the densities of each species will be different for the two bulbs. The rubidium density was given in equation 2.2; The densities of the other species can be calculated by noting that the pressure for each will be constant in the cell, and so the product of density and temperature for each bulb is the same. Given knowledge of the bulb volumes, and the densities at room temperature (see the next section), we obtain the correct ratios of $n_{\mathrm{maser}} = 1.14 n_{\mathrm{room}}$ and $n_{\mathrm{pump}} = .90 n_{\mathrm{room}}$. Below are the gas pressures for cell E17.

An explanation of the choice of cell geometry and gas pressures is contained

Species	Pump Chamber Density	Maser Chamber Density	Pressure
Rb	2.0×10^{13} cm^{-3}	5.8×10^{10} cm^{-3}	
^{129}Xe	3.20×10^{18} cm^{-3}	4.04×10^{18} cm^{-3}	131 torr
^{3}He	3.30×10^{19} cm^{-3}	4.15×10^{19} cm^{-3}	1344 torr
N_2	2.40×10^{18} cm^{-3}	3.02×10^{18} cm^{-3}	98 torr

Table 2.1: Typical Cell Densities and Pressures

within Appendix A. It also includes some observations of the patterns of cell aging and deterioration. In general, the lifetime of a cell under stable running conditions is about six months of use. This is principally caused migration of rubidium out of the pump bulb. Attempts have been made to restore a cell's vitality by heating the maser bulb and transfer tube (or the whole cell) so as to move the Rb back into the pump bulb. These efforts have been uniformly unsuccessful, perhaps because the heat damaged the coating. Generally once a cell is worn out, it has to be replaced.

2.3 Cell Production

Cell production is the most difficult and arguably the most crucial part of this experiment. It required Eddie Otezia [68] at least a year to develop a good coating procedure, and it took Matt Rosen [75] and I over a year to modify and refine this for EDM cells.

The first step of cell production is to have a glassblower assemble a set of three cells, each separately attached to a manifold that has a side-arm for rubidium (refer to figure 2.19). The second step is to clean and coat the cells. The cells are each dipped into a bath of fresh piranha solution. Piranha is a hot, viscous mixture of hydrogen peroxide (30% by volume) and sulfuric acid (70% by volume). After one to two hours, the cells are removed and rinsed three times each with distilled water and then methanol. The cells are then again rinsed with distilled water and left to air dry for about one hour.

After drying, each cell in turn is dipped in the coating solution: five drops of octadecatrichlorosilane [CH_3-$(CH_2)_{17}$-$SiCl_3$ - hereafter referred to as OTS] are placed into 250 ml of solvent, a mixture of hexane and chloroform in a 9:1 volume ratio.

(Five drops is about 200 μl - want .8 ml/liter) The cells remain submerged for five minutes and then are lifted out of the solution and allowed to drip dry for five minutes more. Next comes a thorough rinse in pure chloroform to remove any unreacted OTS, and finally another methanol rinse. When all cells have been coated, they are placed in an oven to dry at 180 °C overnight. The higher temperature is to increase the bake-out rate of residual hexanes trapped on the glass.

It is difficult to obtain good cell coatings every time, and so the coatings are tested before proceeding. Two useful indicators are the contact angle (the "beading") of a water droplet on the glass, and the absence of a meniscus for water in the coated transfer tube. According to certain references, it is possible to successfully coat an unsatisfactory cell through a second application of OTS solution [59], or to at least re-use the glass by removing the coating with piranha [75]. However for this experiment any units that were not satisfactory were simply discarded. The reasons that the coating sometimes fails to form properly are not fully understood, but some ideas are expressed below. The work of Maoz and Sagiv [59], and of Fedchak et al. [25], are very helpful in this regard.

The most common mistakes in coating the glass are to use either the wrong concentration of OTS or to incorrectly gauge the needed amount of water. The coating solution has a threshold concentration at around 1mM, below which the surface tension at the glass-solution interface is insufficient to create a densely packed structure. If the concentration is adequate, the OTS will form a uniform physisorbed monolayer at the glass. In a proper (densely packed) coating the molecules are perpendicular to the surface, which reduces the sticking time of the xenon and maximizes the physical separation between the xenon and paramagnetic impurities in the glass. However, too high a concentration of OTS may cause it to bind to itself, making a conglomerate mass that does not bind well to the walls. Note that the formation of the coating is dependent only on concentration: it is independent of the time spent in the solution for times greater than three minutes or so.

The water issue also can go either way. Water reacts strongly with the OTS, and so too much will ruin the process. However, after the OTS molecules form the monolayer, they still must covalently bond to the glass and one another. This chemical process requires water to hydrolize the coating. In the procedure described

above, the water rinse just prior to coating is designed to leave enough water on the glass for the coating to form. However, good cells have previously been made with no such rinse and even with dry nitrogen blowing through the system to reduce atmospheric moisture. Clearly the water condition is poorly understood.

Note that in most of the "unsuccessful" cells some level of coating is formed, but it is not the desired uniform monolayer and the beading effects are minimal if a water droplet test is performed. (A correct coating will give an equilibrium advancing contact angle of 112° [59]) Once a good coating is formed, however, it is quite robust and is not affected by water or solvents such as methanol or chloroform. The coating is vulnerable to high densities of rubidium however, with Eddie Otezia measuring a failure temperature of 190 °C [68]. A good coating is crucial to obtain long polarization decay times for xenon. The coating acts to reduce the strength of the interactions between the polarized atoms and the paramagnetic impurities in the glass. The coating has little direct effect on the helium, though a damaged (burned) coating may cause problems with helium as well as xenon.

To complete construction of the EDM cells, the molybdenum endplates must be attached. The molybdenum discs are made on a lathe, and then carefully sanded to insure smooth edges. Each disc has a diameter 40 mils greater than the glass cylinder, permitting some margin for error when gluing. To clean the discs, each is dipped in piranha solution for thirty seconds, rinsed in distilled water, and then polished with wipes soaked in methanol. To prevent the coating from interfering with the epoxy, the ends of the maser cylinders are sanded down using an emery board before the discs are attached. The cells are again rinsed with methanol and allowed to dry. When both components are ready, a small quantity of Epo-Tek #353ND epoxy (from Epoxy Technology, Inc. [23]) is prepared. Using the end of a glass pipette, a ring of epoxy is spread on the end of the glass cylinder. The amount used is very important: too little glue will not work, but too much will cause the cells to fail when heated or chilled as described below. (The epoxy has a coefficient of thermal expansion about an order of magnitude different than the glass and molybdenum). The plate is then pressed into position and held in place with a large paper holder. The cell is then baked at 90 °C for half an hour to set the epoxy, and then the procedure is repeated for the other side. Finally, the epoxy is cured at 140 °C for 12 hours. It is advisable

to test the epoxy, confirming that the cells can hold vacuum and high pressure, even at 150 °C or when chilled with liquid nitrogen.

Once the cells have passed the tests above, a 1 g ampule of rubidium is opened and dropped into the side-arm of the manifold. The rubidium is a naturally abundant mix, having 72% ^{85}Rb and 28% ^{87}Rb. The cells and manifold are then placed on the vacuum system, attached with mini-conflat. The manifold (excluding the sidearm) is then baked at a temperature of 125 °C for two or more days. The final pressure achieved is usually in the range of 10^{-9} torr. The rubidium is then chased into the cells using a torch. Care must be taken not to heat the coated cell, because the flame can damage the coating. After the chase, the cells are pumped on for another day, and then filled (refer to figure 2.19). Filling commences with a nitrogen purge of the system. Then, a pressure P_1 of 90% enriched ^{129}Xe is passed through a noble gas getter into the volume V_1 of the gas manifold (Getters are model PS26C50R1V from SAES Pure Gas [82]). This is expanded into V_2 which contains the cells. The selected cell of volume V_3 (a subset of V_2) is then immersed in liquid nitrogen (temperature 77 K) up to the top of the transfer tube. This causes the entire quantity of xenon to freeze into that cell, a process referred to as "cryo-pumping". The final Xe pressure in the cell will then be $(V_1/V_3)P_1$. The volume ratio for the system is 3.8, and the typical final pressure at room temperature is 100 torr. Next, N_2 purified to 99.9999% is passed though a separate nitrogen getter, into the volume $V_1 + V_2$. The pressure is noted, and the final pressure at room temperature will given by

$$P_f = P_i\left(\frac{V_{pump}}{V_{tot}} + \frac{V_{mas} + V_{tube}}{V_{tot}}\left(\frac{T_{room}}{T_{N_2}}\right)\right) \tag{2.4}$$

The procedure is repeated for the ^{3}He, and then the gasses allowed to mix for 15 minutes to become uniform.

Finally the cell is pulled off the manifold and placed in the maser system, where it sits for 2 days at usual running conditions before it is used. This time allows the Rb to spread uniformly through the pump bulb, and to react with any residual impurities from the filling process.

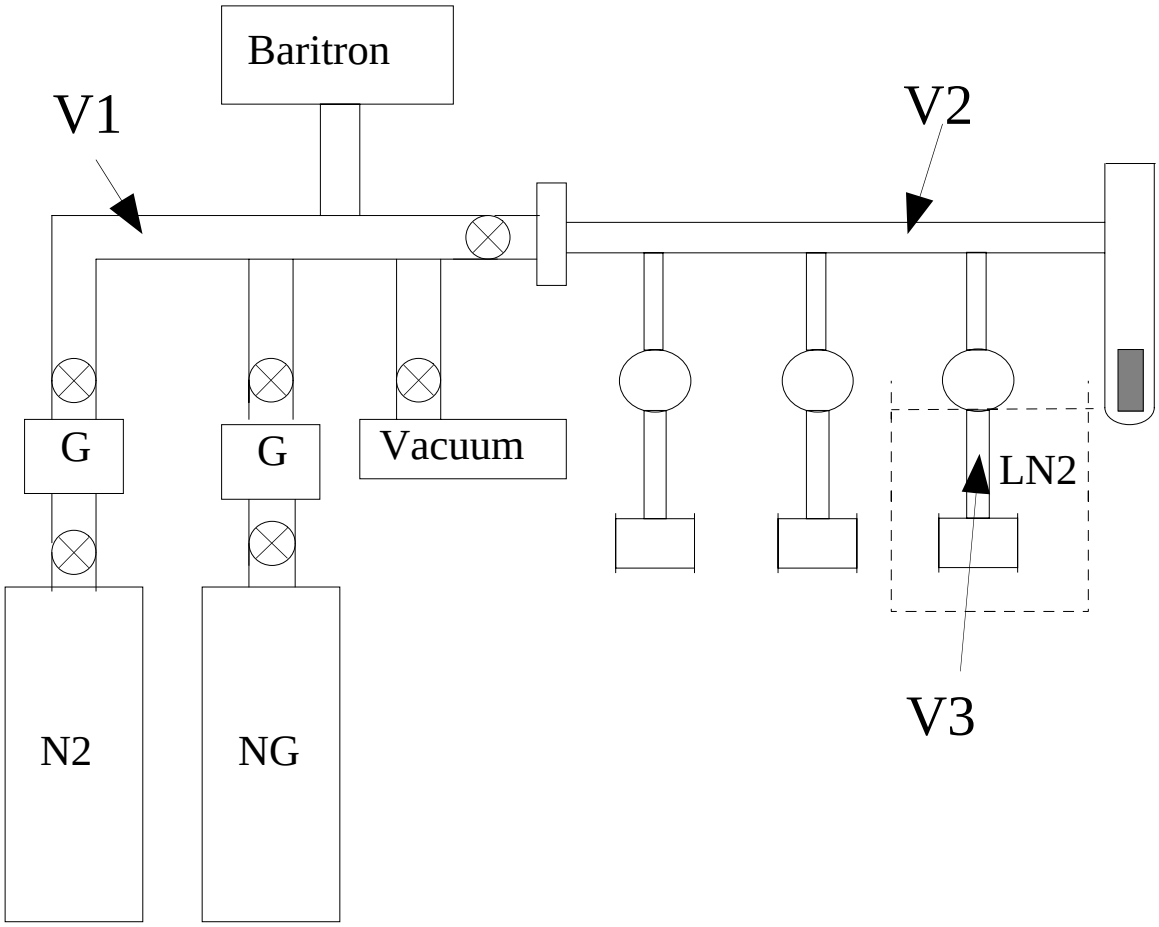

Figure 2.19: Filling portion of the vacuum station with three cell manifold

CHAPTER III

Polarization and Masing

3.1 Introduction

Generating and controlling polarization is a central theme of this experiment. This chapter will discuss how the atomic polarizations are created, the conditions required for masing, and the dynamics inherent in a dual bulb cell. The later sections give estimates for the polarizations and various rate constants, based on both measurements and calculations.

Atomic polarization is a macroscopic quantity related to the average orientation of the spins of the atoms. For the simple, two-state systems used in this experiment, the polarization along a given axis is the number of atoms with spins oriented along that axis minus the number oriented opposite the axis, divided by the total number of atoms:

$$P = \frac{N_\uparrow - N_\downarrow}{N_\uparrow + N_\downarrow} \tag{3.1}$$

One commonly considers the "axis" mentioned above to be the direction of the dominant magnetic field in the experiment. Note that the equation for polarization does not refer to the type of spin involved. To obtain the magnetization, and hence the magnetic field, the magnetic moments must be factored in. This will become relevant when calculating frequency shifts in Chapter Four.

3.2 Optical Pumping and Spin Exchange

The first step in polarizing the noble gases is to create a polarized rubidium vapor. The rubidium is polarized through optical pumping, a technique that has been employed for decades [46],[34]. The basic idea is to transfer the angular momentum of the laser light to the atomic vapor. Consider the following picture. The laser

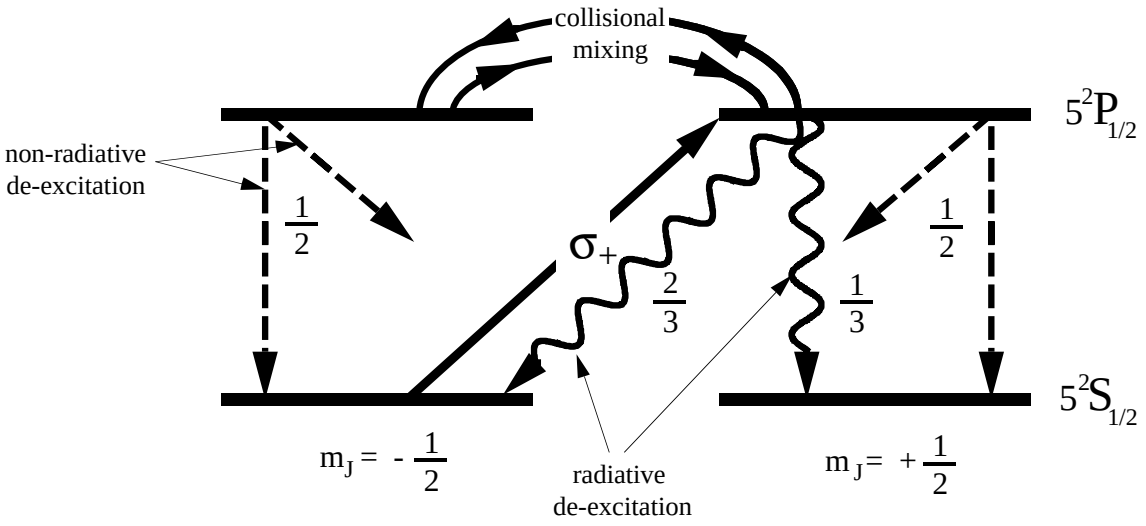

Figure 3.1: Optical Pumping

is circularly polarized and is tuned to the rubidium D1 transition. If the rubidium hyperfine structure is ignored, then these are the only four states that must be considered. The photons can only be absorbed by atoms in the $m = -\frac{1}{2}$ ground state, taking them to the $m = +\frac{1}{2}$ excited state. The excited state spontaneously decays to the two ground states with probabilities given by the appropriate Clebsch-Gordon coefficients, specifically $\frac{2}{3}$ and $\frac{1}{3}$. With enough laser power, all the atoms are eventually pushed out of the $m = -\frac{1}{2}$ ground state and into the $m = +\frac{1}{2}$ state, giving a completely polarized sample.

The presence of other gases in the system modifies this slightly. Collisions with nitrogen quench the excited rubidium, resulting in a much larger de-excitation rate than would be generated through spontaneous emission alone. This is important to prevent radiation trapping, the process where an unpolarized photon spontaneously emitted from one atom goes on to depolarize another atom, which can depolarize

another and so forth. The collisions between rubidium and all the other species also mix the two excited states. Both collisional processes cause the excited atom to have equal probability to return to either ground state, which improves the optical pumping efficiency.

The rubidium polarization is then given in terms of a optical pumping rate γ_{opt} and a relaxation rate Γ_{sd}. If ρ_+ refers to the proportional population of the $m = +\frac{1}{2}$ state, then the rubidium polarization as $\mathrm{P} = (\rho_+ - \rho_-)$ and

$$\frac{\mathrm{dP_{Rb}}}{\mathrm{dt}} = \gamma_{opt}(1 - \mathrm{P_{Rb}}) - \Gamma_{\mathrm{sd}}\mathrm{P_{Rb}} \tag{3.2}$$

For the case of $\mathrm{P_{Rb}(t = 0) = 0}$, this quickly yields

$$\mathrm{P_{Rb}} = \frac{\gamma_{\mathrm{Rb}}}{\gamma_{\mathrm{opt}} + \Gamma_{\mathrm{sd}}}(1 - \mathrm{e}^{-(\gamma_{\mathrm{opt}}+\Gamma_{\mathrm{sd}})\mathrm{t}}) \tag{3.3}$$

The time constant $\frac{1}{(\gamma_{opt}+\Gamma_{sd})}$ is of order milliseconds.

The above description ignored the nuclear magnetic moment of the rubidium. The coupling between the nuclear moment and the electronic moment causes the nucleus to act as a sink for the atom's angular momentum. The nucleus therefore slows down the optical pumping rate of the rubidium by an order of magnitude. Since this is still enormously faster than the other rate constants in the system, the rubidium is either fully polarized if the lasers are on or completely unpolarized if the lasers are off. The nuclear moment also leads to hyperfine structure in the atomic transition. This could be a significant complication, but in this cell the pressure broadening of the nitrogen and noble gases blur the hyperfine states so that they may be ignored.

The process of transferring polarization from the rubidium to the noble gases is called spin exchange. The cause for the transfer is a hyperfine interaction between the Rb valence electron and the noble gas nucleus. The Hamiltonian for this interaction is [36]

$$\mathrm{H} = -2\mathrm{g_n}\mu_\mathrm{n}\mu_\mathrm{B}\sum_{\mathrm{i}=1}^{\mathrm{n}}\left(\frac{\vec{\mathrm{I}}\cdot\vec{\mathrm{S}}_\mathrm{i}}{{\mathrm{r_i}}^3} - 3\frac{(\vec{\mathrm{I}}\cdot\vec{\mathrm{r}}_\mathrm{i})(\vec{\mathrm{S}}_\mathrm{i}\cdot\vec{\mathrm{r}}_\mathrm{i})}{{\mathrm{r_i}}^5} - \frac{8\pi}{3}\delta(\vec{\mathrm{r}}_\mathrm{i})\,\vec{\mathrm{I}}\cdot\vec{\mathrm{S}}_\mathrm{i}\right) \tag{3.4}$$

However, the expression is dominated by the last term, which represents Fermi contact between the electron and the nucleus. The size of the nucleus is therefore a very

important factor, and so xenon has a much faster spin exchange time than helium (about 2 minutes for Xe vs 195 hours for He).

The spin exchange is also strongly influenced by the time of the interaction. Therefore any mechanism that traps the Rb valence electron in the area of the noble gas nucleus is important. One example is the formation of a van der Waal's molecule. This occurs in a collision where a third atom carries away momentum energy so that the remaining Rb-Xe pair is weakly bound. (The Rb-He interatomic potential is too weak to form such molecules [95]). For the cell used in this experiment, this three-body interaction contributes about 60% to the spin exchange rate: binary collisions make up the rest [8].

The equations for the time-dependent noble gas polarizations are analogous to those for rubidium, with a pumping rate γ_{se} and a relaxations rate $\frac{1}{T_1}$. As with the rubidium case, transport dynamics are left out for the sake of clarity. (This is not a good approximation for the helium in a dual bulb cell: see section 3.4 for details)

$$\frac{dP_{NG}}{dt} = \gamma_{se}(P_{Rb} - P_{NG}) - \frac{P_{NG}}{T_1} \tag{3.5}$$

Assuming the rubidium polarization is constant and the initial noble gas polarization is zero, then

$$P_{NG} = P_{Rb}\frac{\gamma_{se}}{\gamma_{se} + \frac{1}{T_1}}(1 - e^{-(\gamma_{se}+\frac{1}{T_1})t}) \tag{3.6}$$

Incidently, the rubidium atoms that are not in the laser light (i.e. not in the pump bulb) will still have some residual polarization arising from spin exchange with the polarized noble gases. Since this is a spin exchange process, equation 3.6 applies if the labels Rb and NG are reversed.

3.3 Theoretical Derivation of Maser Operation

This section introduces the formalism and terminology that describe the maser equations. For ease of computation, SI units are used throughout. The first step is to derive the equations of motion for the noble gas polarizations. To begin with, consider a single noble gas atom of nuclear spin I in a magnetic field B. The nuclear

magnetic moment of such an atom can be written [55]

$$\vec{\mu} = \zeta \frac{\mathrm{e}}{\mathrm{m}} \vec{\mathrm{I}} \tag{3.7}$$

where e is the elementary charge, m is the mass of the proton and ζ is a constant for the atom. In addition, note that the torque on a pure magnetic dipole has the form [42]

$$\vec{\mathrm{N}} = \vec{\mu} \times \vec{\mathrm{B}} \tag{3.8}$$

Recalling that the torque is just the time rate of change of the angular momentum, these equations can be combined to yield

$$\frac{\mathrm{d}\vec{\mu}}{\mathrm{dt}} = \frac{\zeta \mathrm{e}}{2\,\mathrm{m}} \vec{\mu} \times \vec{\mathrm{B}} \tag{3.9}$$

Going a step further, consider the effect of having an ensemble of such atoms. The dipoles can naturally interact with one another and their environment. This leads to a decay of the magnetization with time. The system has a strong magnetic field in the z direction (along the solenoid's axis) and weak ones in x and y, so the z-component of the magnetization is defined to be the longitudinal part, and the other components to be the transverse part. The longitudinal magnetization decays slowly, due to collisions and wall interactions, with some time constant T_1. The decay of the transverse components, T_2, is dominated by dephasing of the spins as was mentioned earlier. It is convenient to describe the system in terms of the average magnetization (magnetic moment density), given by

$$\vec{\mathrm{M}} = \frac{1}{\mathrm{V}^2} \int \vec{\mu}(\vec{\mathrm{r}}) \mathrm{d}^3\mathrm{r} \tag{3.10}$$

for which we can write out

$$\begin{aligned}
\dot{\mathrm{M}}_\mathrm{x} &= \frac{\zeta \mathrm{e}}{\mathrm{m}}(\mathrm{M}_\mathrm{y}\mathrm{B}_\mathrm{z} - \mathrm{M}_\mathrm{z}\mathrm{B}_\mathrm{y}) - \frac{\mathrm{M}_\mathrm{x}}{\mathrm{T}_2} \\
\dot{\mathrm{M}}_\mathrm{y} &= \frac{\zeta \mathrm{e}}{\mathrm{m}}(\mathrm{M}_\mathrm{z}\mathrm{B}_\mathrm{x} - \mathrm{M}_\mathrm{x}\mathrm{B}_\mathrm{z}) - \frac{\mathrm{M}_\mathrm{y}}{\mathrm{T}_2} \\
\dot{\mathrm{M}}_\mathrm{z} &= \frac{\zeta \mathrm{e}}{\mathrm{m}}(\mathrm{M}_\mathrm{x}\mathrm{B}_\mathrm{y} - \mathrm{M}_\mathrm{y}\mathrm{B}_\mathrm{x}) - \frac{\mathrm{M}_\mathrm{z}}{\mathrm{T}_1}
\end{aligned} \tag{3.11}$$

These are the well-known Bloch equations. They can be written terms of polarization and frequency by noting that

$$\vec{\mathrm{M}} = \vec{\mathrm{P}} \mu_{ng}[\mathrm{ng}] \tag{3.12}$$

$$\vec{\omega} = \gamma\vec{B} \tag{3.13}$$

$$\gamma = \frac{\zeta e}{m} = \frac{2\zeta\mu_N}{\hbar} \tag{3.14}$$

where [ng] is the number density of the noble gas species and μ_N is the nuclear magneton.

The equations of motion for the maser bulb polarization, including the source term coming from the pump bulb, are then

$$\begin{aligned} \dot{P_x} &= (P_y\omega_z - P_z\omega_y) - \frac{P_x}{T_2} \\ \dot{P_y} &= (P_z\omega_x - P_x\omega_z) - \frac{P_y}{T_2} \\ \dot{P_z} &= (P_x\omega_y - P_y\omega_x) - \frac{P_z}{T_1} + (FP_p - P_z)G_m \end{aligned} \tag{3.15}$$

G_m is the rate of polarization influx to the maser region [12]. For the moment, P_p is taken as constant, with F to account for transfer tube losses. Naturally, this is only an approximate model of the real cell with its physical transfer tube.

In order to put the above equations in a useful form, the frequency components must be solved for and inserted. The transverse components of the frequency are proportional to the fields generated by the pick-up coils. These fields depend on the current that flows through the coils. The current is induced by the atomic magnetizations, which are precessing with frequency ω_z, and has a value determined by the intercepted flux and the frequency response of the coils. The feed-back inherent in a maser system is now apparent: the strength of the transverse frequencies is set by the size of the transverse magnetizations.

The flux through a given pick-up coil is

$$\begin{aligned} \Phi &= \eta\prime\mu_\circ A M_T \cos(\omega_z t) \\ &= \eta\prime\mu_\circ A\mu_{ng}[ng]P_T\cos(\omega_z t) \end{aligned} \tag{3.16}$$

where A is the area of the pick-up coil and $\eta\prime$ is a dimensionless geometrical constant that accounts for the relative positions of the coil and the cell. The EMF induced in the coil is just the time rate of change of this flux, and then (knowing the coil impedance) it is trivial to find the induced current.

$$\varepsilon = -\frac{d\Phi}{dt}$$

$$= -\Phi\omega_z \tag{3.17}$$

$$\mathrm{Z} = \frac{\omega_\circ \mathrm{R}}{\omega_z}\sqrt{\mathrm{Q}^2\left(\left(\frac{\omega_\mathrm{z}}{\omega_\circ}\right)^2 - 1\right)^2 + \left(\frac{\omega_\mathrm{z}}{\omega_\circ}\right)^2} \tag{3.18}$$

$$\mathrm{I} = \frac{\varepsilon_{max}}{\mathrm{Z}}\cos(\omega_z \mathrm{t} - \delta) \tag{3.19}$$

where $\omega_\circ$ is the resonance frequency of the coil, $\omega_\circ = (LC)^{-\frac{1}{2}}$, and Q is the quality factor of the pick-up coil circuit, $\mathrm{Q} = \frac{\omega_\circ \mathrm{L}}{\mathrm{R}}$

The magnetic field generated by the coils is then just a constant times this current. The pick-up coil is defined to be aligned with the y axis, and so most of the field will be oriented along $\hat{y}$. The other components of the field are ignored. Combining the above equations yields

$$\begin{aligned}\vec{\mathrm{B}} &= \kappa \mathrm{I}\hat{\mathrm{y}} \\ &= \kappa\eta\prime\frac{\mathrm{A}}{\mathrm{L}}\mu_\circ\mu_{\mathrm{ng}}[\mathrm{ng}]\mathrm{P_T}\left(\frac{\omega_\mathrm{z}}{\omega_\circ}\right)^2\rho(\omega_\mathrm{z})\cos(\omega_\mathrm{z}\mathrm{t} - \delta)\hat{\mathrm{y}}\end{aligned} \tag{3.20}$$

where κ is another geometric constant and

$$\rho(\omega_z) = \frac{\mathrm{Q}}{\sqrt{\mathrm{Q}^2\left(\left(\frac{\omega_z}{\omega_\circ}\right)^2 - 1\right)^2 + \left(\frac{\omega_z}{\omega_\circ}\right)^2}^2} \tag{3.21}$$

describes the frequency response of the pick-up coil circuit.

The various constants in equation 3.20 can be combined into more useful forms. The first new constant is η, which combines the earlier geometrical constants.

$$\eta = \kappa\eta\prime\frac{\mathrm{A}}{\mathrm{L}} \tag{3.22}$$

η describes the degree to which the atomic signals feed back on themselves due to the presence of the pick-up coil. Like $\eta\prime$, it is dimensionless. Two more important constants are τ_{rd} and $\mathrm{P}_\circ$ [13]

$$\frac{1}{\tau_{rd}} = \frac{1}{2}\gamma^2\mu_\circ \mathrm{Q}[\mathrm{ng}]\eta\frac{\hbar}{2}\mathrm{P}_\circ \tag{3.23}$$

$$\mathrm{P}_\circ = \frac{\mathrm{F}\mathrm{P}_\mathrm{p}\mathrm{G}_\mathrm{m}}{\mathrm{G}_\mathrm{m} + \frac{1}{\mathrm{T}_1}} \tag{3.24}$$

$\mathrm{P}_\circ$ would be the longitudinal polarization if no pick-up coils were present, or if the coils were tuned far off-resonance. τ_{rd}, the radiation damping time, sets the threshold

for masing as explained below. In terms of these definitions, the transverse frequency is then

$$\gamma\vec{\mathrm{B}} = \vec{\omega} = \frac{2\mathrm{P_T}}{\mathrm{P_\circ}\tau_{\mathrm{rd}}}\left(\frac{\omega_z}{\omega_\circ}\right)^2 \frac{\rho(\omega_z)}{\mathrm{Q}}\cos(\omega_z \mathrm{t} - \delta)\hat{\mathrm{y}} \tag{3.25}$$

where $\mathrm{P_T}$ is the amplitude of the transverse polarization.

It is easier to work with the polarization equations if the transverse polarization remains fixed along the positive x axis (in the rotating frame). This requires making the transformation

$$\hat{\mathrm{y}} \Rightarrow \cos(\omega_{\mathrm{z}}\mathrm{t})\hat{\mathrm{y}}' - \sin(\omega_{\mathrm{z}}\mathrm{t})\hat{\mathrm{x}}' \tag{3.26}$$

Neglecting the $2\,\omega_z$ "Bloch-Siegert" terms of the resulting expressions, the frequencies in the new coordinate system are

$$\begin{aligned}
\omega_x &= \frac{\mathrm{P_x}}{\mathrm{P_\circ}\tau_{\mathrm{rd}}}\frac{\omega_z}{\omega_\circ}\cos(\delta)\sin(\delta) && (3.27)\\
\omega_y &= \frac{\mathrm{P_x}}{\mathrm{P_\circ}\tau_{\mathrm{rd}}}\frac{\omega_z}{\omega_\circ}\cos^2(\delta) && (3.28)\\
\omega_z &= \gamma\mathrm{B_\circ} - \frac{\mathrm{P_z}}{\mathrm{P_\circ}\tau_{\mathrm{rd}}}\frac{\omega_{\mathrm{z}}}{\omega_\circ}\cos(\delta)\sin(\delta) && (3.29)\\
\sin(\delta) &= \rho(\omega_z)\left(\left(\frac{\omega_z}{\omega_\circ}\right)^2 - 1\right) && (3.30)\\
\cos(\delta) &= \frac{\rho(\omega_z)}{\mathrm{Q}}\frac{\omega_z}{\omega_\circ} && (3.31)
\end{aligned}$$

Note that in addition to generating the transverse frequencies, the pick-up coil has also shifted the longitudinal frequency ω_z. This tendency for the coil resonance to shift the atomic frequency is known as cavity pulling. The amount of cavity pulling depends on δ, the phase difference between the precessing atomic magnetization and the coil current.

Finally, the maser equations (in the rotating frame) can be expressed as

$$\begin{aligned}
\dot{\mathrm{P}}_{\mathrm{x}} &= \mathrm{P_x}\left(\frac{\mathrm{P_z}}{\mathrm{P_\circ}\tau_{\mathrm{rd}}}\left(\frac{\omega_{\mathrm{z}}}{\omega_\circ}\cos^2(\delta)\right) - \frac{1}{\mathrm{T_2}}\right) && (3.32)\\
\dot{\mathrm{P}}_{\mathrm{z}} &= \mathrm{FP_pG_m} - \frac{{\mathrm{P_x}}^2}{\mathrm{P_\circ}\tau_{\mathrm{rd}}}\left(\frac{\omega_{\mathrm{z}}}{\omega_\circ}\cos^2(\delta)\right) - \mathrm{P_z}\left(\frac{1}{\mathrm{T_1}} + \mathrm{G_m}\right) && (3.33)
\end{aligned}$$

A visual schematic of the terms which change the polarization vector is given in figure 3.2. G_m accounts for the transport of (longitudinal) polarization into the cell. By definition, $\mathrm{T_1}$ and $\mathrm{T_2}$ reflect the decay of the longitudinal and transverse

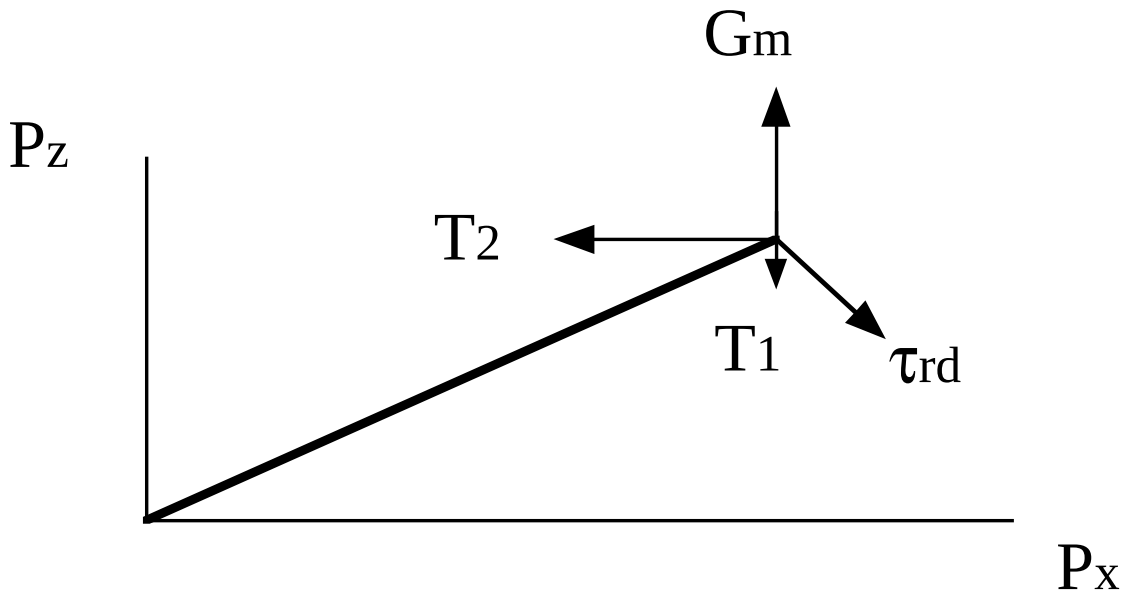

Figure 3.2: Terms changing the Polarization Vector

polarizations, respectively. The last term is the radiation damping, which describes the effect of the pick-up coils in pushing the polarization vector towards $\hat{x}'$

It is trivial to solve these equations, since there is only one steady-state solution with $P_x > 0$, The result gives the equilibrium masing conditions

$$\mathrm{P_z^{eq}} = \mathrm{P_\circ}\,\frac{\tau_{\mathrm{rd}}}{\mathrm{T_2}}\,\frac{\omega_\circ}{\omega_\mathrm{z}\cos^2(\delta)} \tag{3.34}$$

$$\mathrm{P_x^{eq}} = \sqrt{(\mathrm{P_\circ}\tau_{\mathrm{rd}})\frac{\omega_\circ}{\omega_\mathrm{z}\cos^2(\delta)}\mathrm{P_\circ}(\frac{1}{\mathrm{T_1}}+\mathrm{G_m})\left(1-\frac{\tau_{\mathrm{rd}}}{\mathrm{T_2}}\frac{\omega_\circ}{\omega_\mathrm{z}\cos^2(\delta)}\right)} \tag{3.35}$$

$$\omega_z = \gamma\mathrm{B_\circ} - \frac{1}{\mathrm{T_2}}\frac{\sin(\delta)}{\cos(\delta)} \tag{3.36}$$

It can be seen from 3.35 that P_x is real only if $\mathrm{T}_2 > \tau_{\mathrm{rd}}$. This requirement sets the threshold for maser operation.

In the case where the atomic resonance exactly matches the coil resonance ($\delta = 0$), the equations simplify to

$$\dot{\mathrm{P}}_\mathrm{x} = \mathrm{P_x}(\frac{\mathrm{P_z}}{\mathrm{P_\circ}\tau_{\mathrm{rd}}} - \frac{1}{\mathrm{T_2}}) \tag{3.37}$$

$$\dot{\mathrm{P}}_\mathrm{z} = \mathrm{FP_pG_m} - \frac{\mathrm{P_x}^2}{\mathrm{P_\circ}\tau_{\mathrm{rd}}} - \mathrm{P_z}(\frac{1}{\mathrm{T_1}}+\mathrm{G_m}) \tag{3.38}$$

$$\omega_z = \gamma\mathrm{B_\circ} \tag{3.39}$$

and the solution becomes

$$P_z^{eq} = P_\circ \frac{\tau_{rd}}{T_2} \tag{3.40}$$

$$P_x^{eq} = \sqrt{(P_\circ \tau_{rd}) P_\circ (\frac{1}{T_1} + G_m) \left(1 - \frac{\tau_{rd}}{T_2}\right)} \tag{3.41}$$

3.4 Dual Chamber Polarization Dynamics

In the previous derivation of the maser equations, the effects of the pumping region were neglected. The constants G_m and F were used to set the rate of polarization flow into the maser bulb. This is certainly sufficient to understand the maser's steady-state behavior. However, the dynamics of polarization transfer in a dual bulb cell are an interesting problem in their own right, and also very important in obtaining information needed to optimize the cell geometry and pressures.

The first step in incorporating the pump bulb is to include an equation for its longitudinal polarization in the coupled set above, allowing it to vary with the other parameters. The coupling of the pick-up coils to the pump bulb is quite weak, and so it is assumed that the transverse polarization is zero there.

$$\dot{P}_p = (P_{Rb} - P_p)\gamma_{se} - \frac{P_p}{T_1^p} - (P_p - FP_z)G_p \tag{3.42}$$

Once again the factor F is used to account for polarization losses in the transfer tube, so that the pump cell sees a lower effective maser polarization. It is easy to see that the above equation, which replaces equation 3.5, differs because of the addition of a transport term. The equilibrium solution to this equation (for $P_{Rb} > 0$) is

$$P_p = \frac{P_{Rb}\gamma_{se} + P_z^{eq} F G_p}{\gamma_{se} + \frac{1}{T_1^p} + G_p} \tag{3.43}$$

First consider the off-resonance case where there is no P_x. In this instance, P_z^{eq} becomes $P_\circ$, and so substituting into equation 3.24

$$P_p^{off} = \frac{P_{Rb}\gamma_{se}}{\gamma_{se} + \frac{1}{T_1^p} + G_p \left(1 - \frac{F^2 G_m}{G_m + \frac{1}{T_1^m}}\right)} \tag{3.44}$$

Comparing this to the results of section 3.2 which had no transport, we see that the change in the rubidium polarization is negligible ($\gamma_{opt} \gg \mathrm{G_p}$). The xenon polarization changes slightly, dropping a few percent. The helium polarization changes dramatically, dropping to half the value it had when transport effects were neglected.

If instead the pick-up coils are on-resonance and the system is masing, $\mathrm{P_z^{eq}}$ is found from equation 3.34 or 3.40. Taking the latter for clarity, equation 3.44 becomes

$$\mathrm{P_p^{on}} = \frac{\mathrm{P_{Rb}}\gamma_{\mathrm{se}}}{\gamma_{\mathrm{se}} + \frac{1}{\mathrm{T_1^p}} + \mathrm{G_p}\left(1 - \frac{\mathrm{F^2 G_m}\tau_{\mathrm{rd}}}{(\mathrm{G_m} + \frac{1}{\mathrm{T_1^m}})\mathrm{T_2}}\right)} \tag{3.45}$$

Again, the shift from off-resonance to on-resonance changes the xenon pump polarization by only a small amount. The helium is affected more substantially. Numerical values for these equations are provided in section 3.7 .

Moving back to the dynamics of transport, it can be seen that there are now three coupled differential equations for each species. If $\mathrm{P_x} = 0$ (pick-up coils off-resonance) then the two remaining expressions are easily reduced to a single second-order differential equation

$$\begin{aligned}
\ddot{\mathrm{P}}_\mathrm{z} &= \mathrm{F}\dot{\mathrm{P}}_\mathrm{p}\mathrm{G_m} - \dot{\mathrm{P}}_\mathrm{z}(\mathrm{G_m} + \frac{1}{\mathrm{T_1^m}}) \\
&= \mathrm{FG_m}(\mathrm{P_{Rb}}\gamma_{\mathrm{se}} - \mathrm{P_p}(\gamma_{\mathrm{se}} + \frac{1}{\mathrm{T_1^p}} + \mathrm{G_p}) + \mathrm{FP_z G_p}) - \dot{\mathrm{P}}_\mathrm{z}(\mathrm{G_m} + \frac{1}{\mathrm{T_1^m}}) \\
&= -(\gamma_{se} + \frac{1}{\mathrm{T_1^p}} + \frac{1}{\mathrm{T_1^m}} + \mathrm{G_p} + \mathrm{G_m})\dot{\mathrm{P}}_\mathrm{z} - \\
&\quad (\gamma_{se}\mathrm{G_m} + \frac{\gamma_{\mathrm{se}}}{\mathrm{T_1^m}} + \frac{\mathrm{G_p}}{\mathrm{T_1^m}} + \frac{\mathrm{G_m}}{\mathrm{T_1^p}} + \frac{1}{\mathrm{T_1^p T_1^m}} + \mathrm{G_m G_p}(1 - \mathrm{F^2}))\mathrm{P_z} + \mathrm{FG_m}\gamma_{\mathrm{se}}\mathrm{P_{Rb}}
\end{aligned} \tag{3.46}$$

The solution is therefore a double exponential [81]

$$\mathrm{P_z} = \mathrm{A_1 e^{-m_1 t}} + \mathrm{A_2 e^{-m_2 t}} + \epsilon \tag{3.47}$$

where

$$m_1 = \frac{1}{2}(\alpha + \sqrt{\alpha^2 - 4\beta}) \tag{3.48}$$

$$m_2 = \frac{1}{2}(\alpha - \sqrt{\alpha^2 - 4\beta}) \tag{3.49}$$

$$\alpha = \gamma_{se} + \frac{1}{\mathrm{T_1^p}} + \frac{1}{\mathrm{T_1^m}} + \mathrm{G_p} + \mathrm{G_m} \tag{3.50}$$

$$\beta = (\frac{1}{T_1^m} + G_m)(\gamma_{se} + \frac{1}{T_1^p} + G_p(1 - \frac{F^2 G_m}{G_m + \frac{1}{T_1^m}})) \quad (3.51)$$

$$A_1 = \frac{(m_2 - G_m - \frac{1}{T_1^m})P_z(0) + FG_m P_p(0) - m_2\epsilon}{m_2 - m_1} \quad (3.52)$$

$$A_2 = \frac{(G_m - \frac{1}{T_1^m} - m_1)P_z(0) - FG_m P_p(0) + m_1\epsilon}{m_2 - m_1} \quad (3.53)$$

$$\epsilon = \frac{FG_m\gamma_{se}P_{Rb}}{\beta} \quad (3.54)$$

where $P_p(0)$ and $P_z(0)$ refer to the initial polarizations.

Sections 3.6 and 3.7 demonstrate how this model has been used to calculate the noble gas polarizations. Appendix A describes how the different model parameters were optimized to obtain improved maser performance. This model can be made more accurate by including all the diffusion modes of the cylindrical transfer tube, instead of using just the first order G_m,G_p coefficients [86]. However the modest additional benefit was not judged to be worth the added mathematical complexity for the calculations performed here.

3.5 Near-Equilibrium Oscillations

In theory, the masers should reach their equilibrium state after some hours of settling time, and then remain in that state thereafter. In practice, there are often small perturbations to the masers that trigger a transient response. The source of such perturbations could be a burst of noise from a high voltage discharge, or an abrupt change in room temperature. In some cases the perturbations are sufficiently frequent that the maser oscillates continuously. To deal with this situation, it is convenient to extend the solutions to the maser equations to include near-equilibrium oscillations. In this regime, the polarizations can be written as the sum of the equilibrium solution (e.g. P_z^{eq}) plus a small time-dependant piece (e.g δP_z). Written in this form, the maser equations (given in equations 3.32 and 3.42) are

$$\left(\dot{P_x^{eq}} + \delta\dot{P}_x\right) = (P_x^{eq} + \delta P_x^{eq})\left(\frac{P_z^{eq} + \delta P_z}{P_\circ \tau_{rd}}(\frac{\omega_z}{\omega_\circ}\cos^2(\delta)) - \frac{1}{T_2}\right) \quad (3.55)$$

$$\left(\dot{P_z^{eq}} + \delta\dot{P}_z\right) = FG_m(P_p^{eq} + \delta P_p) - \frac{(P_x^{eq} + \delta P_x)^2}{P_\circ \tau_{rd}}\left(\frac{\omega_z}{\omega_\circ}\cos^2(\delta)\right) - (P_z^{eq} + \delta P_z)(\frac{1}{T_1} + G_m)$$

$$\left(\dot{P_p^{eq}} + \delta\dot{P}_p\right) = P_{Rb}\gamma_{se} + FG_p(P_z^{eq} + \delta P_z) - \left(\gamma_{se} + G_m + \frac{1}{T_1}\right)(P_z^{eq} + \delta P_z)$$

From the definition of the equilibrium solutions (equations 3.34, 3.35), we can cancel out static pieces. Then, making the assumption that the changes in the masers are small leads to the maser's near-equilibrium behavior

$$\delta\dot{P}_x = \frac{P_x^{eq}}{P_\circ \tau_{rd}}\delta P_z \tag{3.56}$$

$$\delta\dot{P}_z = FG_m\delta P_p - \frac{2P_x^{eq}}{P_\circ \tau_{rd}}\delta P_x - \left(G_m + \frac{1}{T_1}\right)\delta P_z \tag{3.57}$$

$$\delta\dot{P}_p = FG_p\delta P_z - \left(\gamma_{se} + G_m + \frac{1}{T_1}\right)\delta P_z \tag{3.58}$$

Unfortunately these three coupled differential equations do not have an analytical solution. If only the first two equations are considered (i.e. transport effects are neglected), then the two remaining equations can be combined into a single second-order differential equation, such as

$$\delta\ddot{P}_z = -\left(G_m + \frac{1}{T_1}\right)\delta\dot{P}_z - 2\left(\frac{P_x^{eq}}{P_\circ \tau_{rd}}\right)^2 \delta P_z \tag{3.59}$$

The solution to this equation is clearly an exponentially decaying sine wave. The decay rate is $\frac{1}{2}\left(G_m + \frac{1}{T_1}\right)$ and the frequency of the oscillation is

$$\omega \approx \sqrt{2}\frac{P_x^{eq}}{P_\circ \tau_{rd}} \tag{3.60}$$

Just as in section 3.4 above, ignoring the transport effects gives reasonable results for the xenon but not for the helium. In particular, equation 3.60 gives a value for the period of the helium oscillation that is about 300 seconds, while the experimentally measured value is close to 2000 seconds. A numerical evaluation of the three coupled equations reveals that the maser amplitude still varies as a decaying sinusoid. However, in this case the helium oscillation period is 1800 seconds, in much better agreement with the data. The effect that these oscillations have on the data is discussed in sections 4.3 and 5.3 .

3.6 Determining the Rate Constants

The previous sections have derived the equilibrium solutions for P_p, P_z, and P_x. These were given in terms of P_{Rb} and six further constants for each species. This sec-

tion will obtain numerical values for these constants, through a mix of measurement and calculation. A table of these values is given at the end of the section.

The first measurement made is performed with the helium. Since the helium diffuses so rapidly compared to its slow spin exchange and polarization loss times, the entire cell can be treated as a single volume when the pick-up coils are off-resonance. This means that there will be essentially no difference between the pump and maser bulbs. Therefore $F \approx 1$, and $T_1^p = T_1^m = T_1$. ^{3}He has another advantage, which is that $G \gg \frac{1}{T_1} \gg \gamma_{se}$. When these (very good) approximations are made, the dynamics of the cell polarization become trivial. Specifically, the two rate constants in the double exponential solution for P_z become

$$m_1 \approx (G_p + Gm) \tag{3.61}$$

$$m_2 \approx \frac{1}{T_1} \tag{3.62}$$

To measure the m's, we observe how P_z evolves in a transfer time measurement. The cell begins fully polarized, with the pick-up coils off-resonance and the gradients deliberately mistuned to give a short T_2. Then a large, near 90 degree tip is applied to both species in the maser bulb. This leads to a very large transverse polarization which quickly dies away, leaving the maser bulb with close to zero polarization. By pulsing several times in the following few minutes, one can observe the polarization from the pump bulb redistribute itself throughout the cell. This causes an exponential rise with time constant m_1, and it yields $G_p + G_m$. Following this rapid redistribution, the signal rises with a much slower time constant of several hours. The corresponding rate is $m_2 = \frac{1}{T_1}$. In the ideal case where the initial pulse destroys all the maser polarization without affecting the pump polarization, A_1 and A_2 are equal; even with a real pulse the magnitudes will be comparable. Therefore measuring the helium m's is not too difficult.

It is much harder to measure G_p and G_m separately. Fortunately, the way in which they are defined allows them to be related by a simple formula (see equation 3.65 below); through a coincidence of cell volumes and temperatures, it turns out they are nearly equal. Thus for the helium, the transfer time measurement provides the information needed to know most of the needed parameters (all except γ_{se}) to a high level of accuracy.

The constants for xenon are quite different from those of the helium, and this leads to a different form for the two exponents. Since the G's and the $\frac{1}{T_1}$'s are of comparable magnitude, the expression for the slower rate is now

$$m_2 \approx \left(\frac{1}{T_1^m}\right) + G_m\left(1 + \frac{F^2 G_p}{\gamma_{se}}\right) \tag{3.63}$$

γ_{se} is the fastest rate for the xenon, and so it dominates m_1.

$$m_1 \approx \gamma_{se} + \frac{1}{T_1^p} + G_p\left(1 + \frac{F^2 G_m}{\gamma_{se}}\right) \tag{3.64}$$

If a transfer time measurement is run on the xenon to find these parameters, the slower m_2 can be determined, but not the rapid m_1. In terms of these equations, the difficulty is that A_2 is an order of magnitude larger than A_1. Physically the reason is that the xenon maser polarization acts as a substantial drain on the pump polarization even when the polarizations are in equilibrium. Abruptly reducing the maser polarization only perturbs the pump polarization slightly before its rapid spin exchange catches up. This is quite different from the helium, where the polarizations of the two bulbs re-equilibrate well before spin exchange becomes significant.

To determine G_m and $\frac{1}{T_1^m}$ separately requires a second piece of information, which again is provided by theory. The transport coefficient G_m for the two noble gas species are different by the ratio of the diffusion constants, calculated below. The ratio was confirmed at the 20% level by experimental measurement [77]. Once G_m is known, $\frac{1}{T_1^m}$ is determined moderately well. Futhermore, G_m can be related to G_p for the xenon, just as it was for the helium.

The remainder of this section deals with calculated results. First of all, it is possible to compare the experimental value obtained for the helium G_m with theory. For a pump cell of volume V_p connected to the maser cell by a transfer tube of length L and cross-sectional area A, the rate of transfer out of the pump cell is [12]

$$G_p = \frac{D_p A}{V_p L} \tag{3.65}$$

The same formula can be applied to G_m. To evaluate this numerically requires the diffusion constants. The total diffusion constant for helium in terms of the pressures and partial diffusion constants is as follows [19]

$$\frac{1\,\text{atm}}{D_{He}} = \frac{P_{He}}{D_{He}^{He}} + \frac{P_{Xe}}{D_{He}^{Xe}} + \frac{P_{N_2}}{D_{He}^{N_2}} \tag{3.66}$$

The equation for Xe is completely analogous. Typical cell pressures are given in table 2.1. (Note $D_{He}^{Xe} = D_{Xe}^{He}$ [19]) The noble gas partial diffusion constants have been exhaustively measured by Kestin et al. [52]. The constants for noble gases moving through nitrogen are less well documented. The xenon-nitrogen constant was measured by Cates, et al. [7]. In the case of helium-nitrogen, it easiest was to calculate the constant, using the equation [37]

$$D_{N_2}^{NG} = (k_B T)\frac{4\sqrt{\frac{2k_B T}{\mu}}}{3\pi(d_{N_2} + d_{NG})^2(1\,\mathrm{atm})} \tag{3.67}$$

where $T_\circ$ is 298K and the d's are the atomic diameters (from [87])

Coefficient	T = 40 °C	T = 120 °C
D_{Xe}^{Xe}	0.0627 cm^2/sec	0.0971 cm^2/sec
D_{He}^{He}	1.96 cm^2/sec	2.87 cm^2/sec
D_{Xe}^{He}	0.593 cm^2/sec	0.869 cm^2/sec
$D_{Xe}^{N_2}$	0.11 cm^2/sec	0.16 cm^2/sec
$D_{He}^{N_2}$	0.536 cm^2/sec	0.812 cm^2/sec

Diffusion Constant	Maser Chamber	Pump Chamber
D_{Xe}	0.144 cm^2/sec	0.216 cm^2/sec
D_{He}	0.691 cm^2/sec	1.02 cm^2/sec

Table 3.1: Values for partial D's, final D's both species

.

These D values give a calculated helium G_p (from equation 3.65) of 0.0059 sec^{-1}, in rather poor agreement with the experimental measurement of $0.0026 + -0.0006$ sec^{-1}. More reliably, it yields the ratio of G_p^{He} to G_p^{Xe} as 4.80. This leads to the Xe G_p and G_m values, and so the xenon T_1. The numerical values are in table 3.3.

These longitudinal relaxation rates, T_1's, are difficult to calculate directly. They include contributions from collisions with gases, the gradients of the transverse magnetic fields, and wall interactions. The gradients contribute [18],[30]

$$\frac{1}{T_1} \approx D\,\frac{|\nabla B_x|^2 + |\nabla B_y|^2}{B_\circ^2} \tag{3.68}$$

The effect of collisions with other gases can be calculated in analogy to equation 3.76 below. However, the wall interactions are very important; for xenon they dominate by far. It is very hard to model these interactions because of their extreme complexity [91], [21],[45], and so the values found experimentally must be used without a cross-check.

It is expected that the interaction between the xenon and the walls will scale as some characteristic binding energy divided by the kinetic energy of the atom [25]: therefore the xenon T_1 should increase with temperature, and T_1^p should be greater than T_1^m The difference is modest, though, and is obscured by the transport between the two bulbs of the cell, so I have simply taken the xenon T_1 to be constant throughout the cell.

As a side note, be aware that the transverse relaxation rates (set by the T_2's) are not just the values given by equation 2.1. That "inherent" T_2, which is caused by magnetic field gradients, is modified by the longitudinal relaxation rate, the transport dynamics, and the radiation damping. In the upper energy state (i.e. when the spins are antiparallel to B), the effective T_2 is

$$\frac{1}{T_2^{\text{eff}}} = \frac{1}{T_2} + \frac{1}{T_1} + G_m - \frac{1}{\tau_{rd}} \tag{3.69}$$

T_2^{eff} is both the experimentally measured quantity and the correct time constant for the Bloch equations above. For most off-resonance work, where FID is being used, T_2^{eff} and T_2 are very similar, and so both quantities are simply called T_2. However, there are cases where the distinction becomes relevant. For example, in cells with an incorrect coating the Xe T_2^{eff} is dominated by T_1, and can be less than five seconds despite good gradients. More details of optimizing T_2^{eff} are given in Appendix A.

The xenon constant F reflects by the polarization loss to the walls during transport. The time spent in the tube is estimated from the first order diffusion mode [72]

$$\text{Time} = \frac{L^2}{2D} \tag{3.70}$$

which gives 47 seconds for Xe. The other required parameter is the T_1 in the transfer tube. This is corrected for temperature by averaging the pump and maser values given above. A much larger adjustment comes from the smaller surface to volume

ratio in the transfer tube compared to the maser cylinder. Since the collision rate goes as this ratio squared, there is correction factor equal to the square of the ratio of the radii of the two cylinders. The final form for F is

$$\mathrm{F} = \exp\left(\frac{-\,\mathrm{L}^2\,\mathrm{r}^2}{2\,\mathrm{D_{Xe}}\,\mathrm{T_1}\,\mathrm{r_t^2}}\right) \tag{3.71}$$

This gives a value for the Xe F of 0.75. The assumption that the He F = 1 can also be checked: the calculations above give a He transfer time of 10 seconds and an F = 0.994.

The last constants to be dealt with are γ_{se}'s. It turns out that these are easy to calculate. The pumping rates for the noble gases are given by

$$\gamma_{NG} = \mathcal{K}_{\mathrm{se}}^{\mathrm{NG}}\,[\mathrm{Rb}] \tag{3.72}$$

[Rb] is approximately given by equation 2.2. $\mathcal{K}_{\mathrm{se}}^{\mathrm{He}}$ arises exclusively from binary collisions, whereas $\mathcal{K}_{\mathrm{se}}^{\mathrm{Xe}}$ has contributions from both binary and three-body processes. The contribution from binary collisions is k_{se}, the velocity-averaged rate constant for spin exchange. k_{se} and its counterpart k_{sr} (velocity-averaged spin rotation) are found from the cross section σ

$$k_{se} = <\sigma \mathrm{v}> \tag{3.73}$$

Table 3.2 gives a list of of these values. The numbers presented include the nuclear slowing down factor of 10.8. Most of the coefficients have modest temperature dependence, but the Rb-He spin rotation is highly temperature dependent, going as $T^{4.259}$ [5]. The values given are for typical running conditions (120 °C).

Species	k_{se}	k_{sr}	References
Rb-Rb	Not applicable	4.2×10^{-13}	[5]
Rb-^{129}Xe	3.9×10^{-16}	4.7×10^{-15}	[89]
Rb-^{3}He	7.1×10^{-20}	1.0×10^{-18}	[5]
Rb-N_2	8×10^{-19}	9×10^{-18}	[68] , [91]

Table 3.2: Spin Exchange and Spin Rotation Coefficients k

The three-body contribution for xenon is strongly pressure dependant [8], but in the regime appropriate to our cell it is

$$k_3 = \frac{\xi}{[Xe] + b_{N_2}[N_2] + b_{He}[He]} \tag{3.74}$$

Given that $\xi = 5.2 \times 10^3$ [8], $b_{N_2} = 0.275$ [8], and $b_{He} = 0.15$ [71], we find that $k_3 = 9.8 \times 10^{-16}$ for 120 °C.

Adding together the binary and three-body contributions gives $\mathcal{K}_{\rm se}$. By then multiplying by the rubidium density we obtain $\gamma_{He} = 1.42 \times 10^{-6}$ and $\gamma_{Xe} = 0.020$ at 120 °C

Below is a table containing all the rate constants that appear in the previous section. Experimental values have been used when possible, and calculated values when necessary.

Constant	He	Xe
γ_{se}	1.42×10^{-6}	2.0×10^{-2}
$\mathrm{G_p}$	2.6×10^{-3}	5.4×10^{-4}
$\mathrm{G_m}$	2.5×10^{-3}	5.2×10^{-4}
$\frac{1}{\mathrm{T_1^p}}$	4.1×10^{-5}	4.0×10^{-4}
$\frac{1}{\mathrm{T_1^m}}$	4.1×10^{-5}	4.0×10^{-4}
F	0.994	0.75

Table 3.3: Rate Constants. All are given in $\mathrm{s^{-1}}$, except F which is dimensionless.

3.7 Estimates of Polarizations

With the rate constants in hand, the polarizations of the noble gases are known in terms of the rubidium polarization. $\mathrm{P_{Rb}}$, in turn, can be found if Γ_{sd} and γ_{opt} are known (recall equation 3.3). Technically both the spin destruction and the optical pumping are functions of position, but Γ_{sd} and γ_{opt} are taken to be averages over the pump bulb.

The rubidium relaxation rate Γ_{sd} is easy to estimate. At the pressures used in this experiment, the effect of wall collisions on the rubidium is negligible compared to collisions with other gases (making this assumption is equivalent to ignoring the spatial dependence of the spin destruction). The gas collisions can cause either spin exchange or just spin rotation. The complete expression is given by

$$\Gamma_{sd} = k_{sr}^{Rb}\,[\mathrm{Rb}] + \mathrm{k_{sr}^{He}}\,[\mathrm{He}] + \mathrm{k_{sr}^{Xe}}\,[\mathrm{Xe}] + \mathrm{k_{sr}^{N_2}}\,[\mathrm{N_2}] + \tag{3.75}$$

$$(P_{Rb} - P_{He})\, k_{se}^{He}\, [He] + (P_{Rb} - P_{Xe})\, k_{se}^{Xe}\, [Xe] + (P_{Rb} - P_{N_2})\, k_{se}^{N_2}\, [N_2]$$

A brief perusal of the numerical values in table 3.2 will reveal that Γ_{sd} is completely dominated by spin rotation with xenon. For cell E17, this gives Γ_{sd} of 16 kHz.

The pumping rate γ_{opt} for the rubidium is considerably more difficult to determine. It is set by the flux of incident photons and the cross-section for absorption, both of which are frequency dependent. The Rb resonance in the pump bulb is pressure broadened 19 GHz/amagat for the noble gases and 18 GHz/amagat for N_2 [75]. Inserting values from table 2.1 yields a width for the Rb absorption line of about 38 GHz (= 0.08 nm). Recall that the laser linewidth is greater than 1 nm, and possesses considerable smaller scale structure (refer to figure 2.7). Since the unpolarized rubidium will absorb and scatter the on-resonance light, both the photon flux and rubidium polarization are position dependent. A program to calculate this numerically has been developed in my lab group [90].

The program finds the Rb polarization for a single (sealed) spherical cell: corrections for the double bulb design are negligible for the rubidium, as described in section 3.4 . For typical running conditions the program gives $P_{Rb} = 0.85$. Given the broad profile of the laser diode arrays (refer to figure 2.7), the result is insensitive to small changes in beam structure. It is also has very little variation with temperature.

It is possible to obtain an estimate of the rubidium polarization experimentally as well. By measuring the noble gas signal as a function of laser power, it is possible to obtain a curve that can be fit to a $\frac{\gamma_{opt}}{\gamma_{opt}+\Gamma_{sd}}$ profile. This method assumes that the temperature control circuit can fully compensate for the changing laser power (refer to subsection 2.2.3). It also assumes that the frequency profiles of the two lasers are similar near the rubidium resonance. With these caveats, the Rb polarization is estimated to be 0.68. This is moderate agreement with the calculated value.

For the rubidium outside the laser light, both the spin exchange and the spin destruction are dominated by interactions with xenon. Spin exchange is given by equation 3.72 with the rubidium density replaced by the xenon density. Spin destruction will be the same as equation 3.76. Putting in the appropriate factors, we find that the rubidium polarization "in the dark" is 10% of the xenon polarization. The xenon polarization is determined below.

For the noble gases, one must be careful to specify the conditions when reporting

a polarization. The values will be different when the system is off-resonance (where most cell diagnostics occur) and masing (where EDM data is actually taken). There are also different polarizations in the pump and maser bulbs, due to the effects of the pick-up coils and transfer tube. When masing, the noble gases in the maser bulb also have a transverse polarization. The values below all reflect longitudinal polarization, however.

Before giving numerical results for the xenon polarization, there is one more correction that has thusfar been ignored. This is the dilution factor, which accounts for the fact that 10% of the xenon in the cell is not ^{129}Xe and so will not contribute to the signal. Equations 3.6, 3.44, and 3.47 should all be multiplied by 0.90 to obtain accurate numbers.

The first case to be considered is when the system is off-resonance. In this case the polarization in the pump chamber is given by equation 3.43; the rates that have been compiled in table 3.3 just need to be inserted. This results in a Xe polarization of 0.59 and a He polarization of 0.0083 (using $P_{Rb} = 0.68$). As explained earlier, when off-resonance the He polarization will be this same value throughout the cell because its $T_1 \gg \frac{1}{G_m}$. The Xe polarization undergoes a steady decline in traversing the transfer tube, and its off-resonance equilibrium value is given by equation 3.24. This yields $P_z = 0.23$ for the Xe in the maser bulb.

While masing, of course, Pz decreases by a factor of $\frac{\tau_{rd}}{T_2}$. This reduction can be verified experimentally as follows. First an FID is taken on-resonance but in the lower energy state. The size of the amplitude is therefore proportional to $P_\circ$. Then the system is switched to the upper energy state and the resulting maser is allowed to equilibrate. The transverse polarization is abruptly killed through application of large magnetic field gradients, and another FID is immediately taken. The initial signal is proportional to the equilibrium masing P_z, which is seen to be less by the factor $\frac{\tau_{rd}}{T_2}$ mentioned above. This reduction puts the on-resonance Xe maser chamber polarization at 0.015, and the on-resonance He polarization at 0.0016. The reduction in P_z also reduces the pump bulb polarization, as described in section 3.4. Referring to equation 3.43 and inserting the new value for P_z, one predicts an 73% reduction in the He P_p and a 2% reduction in the Xe P_p. Numerically this results in an on-resonance He pump chamber polarization of 0.0019, and an on-resonance Xe pump

chamber polarization of 0.58.

All of these calculated values are summarized in table 3.4.

Off-Res	He	Xe
Pump	0.0083	0.59
Maser	0.0083	0.23

On-Res	He	Xe
Pump	0.0019	0.58
Maser	0.0016	0.015

Table 3.4: Calculated Polarizations, based on $P_{Rb} = 0.68$

A second means to estimate the polarization is to derive it from the size of the observed signals in the pick-up coils. The equation for the current induced in the coil (see equation 3.19) is easily converted to voltage measured.

$$V = \text{Gain}\ \eta\prime\ \frac{A}{LC}\,\mu_\circ\,\mu_{ng}\,[ng]\,P_T\,\left(\frac{\omega_z}{\omega_\circ}\right)^2\,\rho(\omega_z) \tag{3.76}$$

Typical voltages while masing are 23 μV for the xenon and 11 μV for the helium. FID signals are about 1.2 μV xenon and 3.4 μV for the helium.

The principal limitation of the method is its dependence on the filling factor, which must be calculated. The filling factor is found by integrating the flux through a nearby coil from a cylindrical volume of magnetic dipoles. The contribution of dipoles in transfer tube is ignored. The calculation performed is

$$(\eta' A) = \frac{1}{4\pi}\int_{z=0}^{2.0}\int_{r=0}^{.635}\int_{\theta=0}^{2\pi}\int_{p=0}^{1.88}\int_{\phi=0}^{2\pi}\frac{(r\sin\phi + p\cos\theta)(z - p\sin\theta)}{((s - r\cos\phi)^2 + (r\sin\phi + p\cos\theta)^2 + (z - p\sin\theta)^2)^{2.5}} \tag{3.77}$$

and is evaluated numerically (refer to figure 3.3). This results in a value of 0.53 +- 0.01 cm^2 for the average loop, given a spacing of 0.2 cm between the edge of the coil and the axis of the cell. The filling factor is this value times the number of turns (3550 for each species). A more careful calculation that averaged over the coil's range in ρ gave very similar results.

In order to determine the longitudinal polarization from this, it is also necessary to know the tip angle. This can be calibrated for FID experiments by measuring the

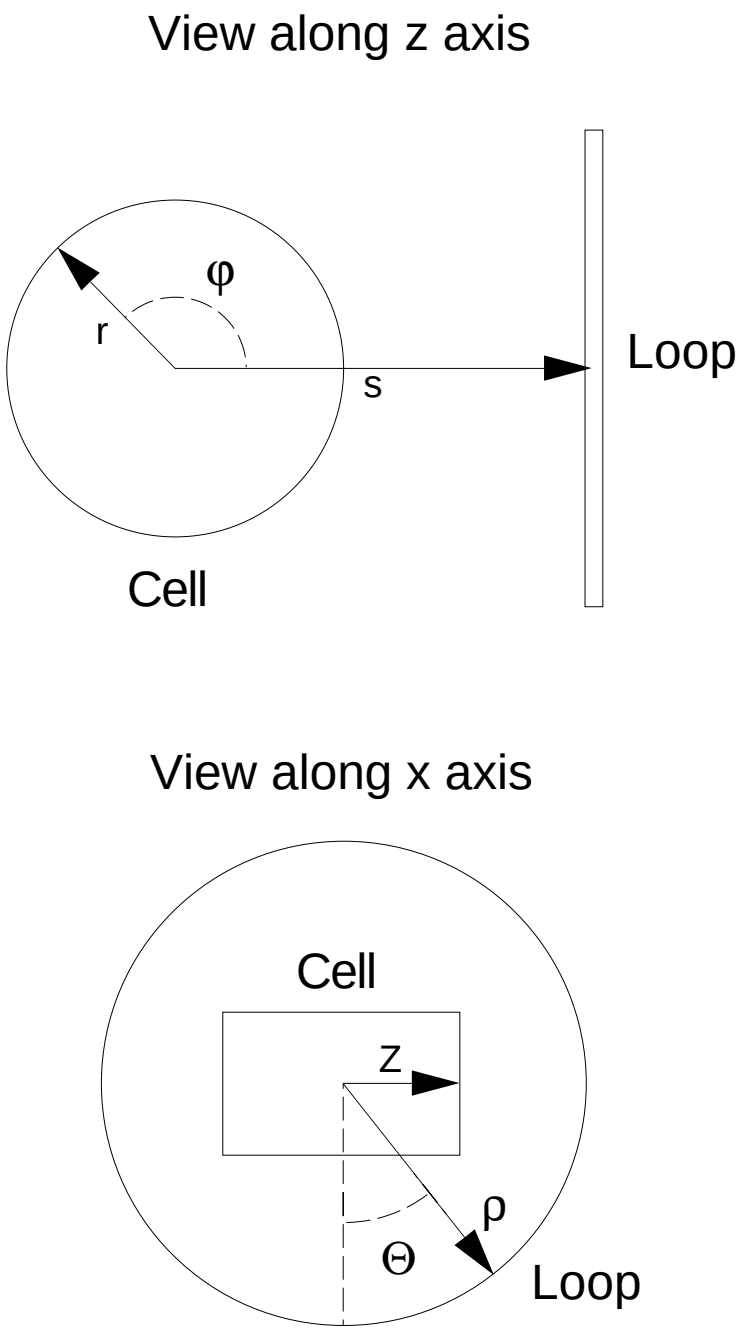

Figure 3.3: Calculation of cell filling factor η'A

signal amplitude as a function of the voltage applied to the pulse coil, and fitting to a sine wave. As previously reported, this gives a 4° Xe tip and a 6° He tip. While masing, the tip angle is just the inverse tangent of $\frac{P_x}{P_z}$. From equation 3.40, it can be seen that

$$\frac{P_x}{P_z} = T_2\sqrt{(G_m + \frac{1}{T_1})(\frac{1}{\tau_{rd}} - \frac{1}{T_2})} \tag{3.78}$$

This gives me a masing tip angle of 62° for the xenon and 47° for the helium.

With the tip angle calibration in hand, the longitudinal polarization derived from the signal size S is

$$P_z = \frac{S}{\mu_\circ \mu_{ng}[ng]\eta' A\omega_z \rho(\omega_z) f_{tip}} \tag{3.79}$$

The values for P_z off resonance in the maser bulb ($P_\circ$) are 0.16 for the xenon and 0.0017 for the helium. The on-resonance longitudinal polarizations in the maser cell are 0.0096 for the xenon and 5.3×10^{-5} for helium.

These values are somewhat lower than the numbers calculated above. The xenon is low by a factor of 1.5 to 2, while the helium is low by a factor of 3 to 5. The discrepancy may be due to difficulties in correctly determining the polarization transport, or in obtaining an accurate value for f_{tip}. Another possible source of the error is the uncertainty in the rubidium density. This is suggested by the helium discrepancy being greater than the xenon. If the rubidium density of the pump bulb was a factor of three lower than the value used in equation 3.72, then the two calculations would be in agreement. A factor of three difference corresponds to an error of 20 °C in the pump bulb temperature, which seems large but is not out of the question. The shifts calculated in Chapter Four all make use of the higher, calculated values.

CHAPTER IV

Stability, Noise and Frequency Shifts

One principal advantage of the maser is that it can be used to take measurements continuously for months. The system can certainly run for this long; it has maintained dual species masing for weeks at a time without difficulty. However, this does not guarantee a good EDM measurement. The system must also remain stable, so that the expected frequency shifts remain constant with time. Furthermore, the level of noise in the system must be kept small to in order to have low statistical errors. This chapter presents the criteria for maser stability and the size and origin of various frequency shifts. It then goes on to discuss the sources of noise and various drifts that make it difficult to make a high quality measurement in a timely fashion.

4.1 Measurements of Stability

The masers are used as a tool to measure the noble gas precession frequencies. To make such a measurement, I obtain the phase of each maser as a function of time and then fit the data points to a line. Assuming that each of the N data points has the same error σ_i, the frequency is [4]

$$\nu = \frac{12}{2\,\pi\,\tau^2 N}\left(\sum_{i=1}^{N}\phi_i t_i - \sum_{i=1}^{N}\phi_i \sum_{i=1}^{N} t_i\right) \tag{4.1}$$

and the uncertainty in the frequency is

$$\nu_{ng} = \frac{1}{\tau}\sqrt{\frac{12}{2\,\pi}\frac{\sigma_i^2}{N}} \tag{4.2}$$

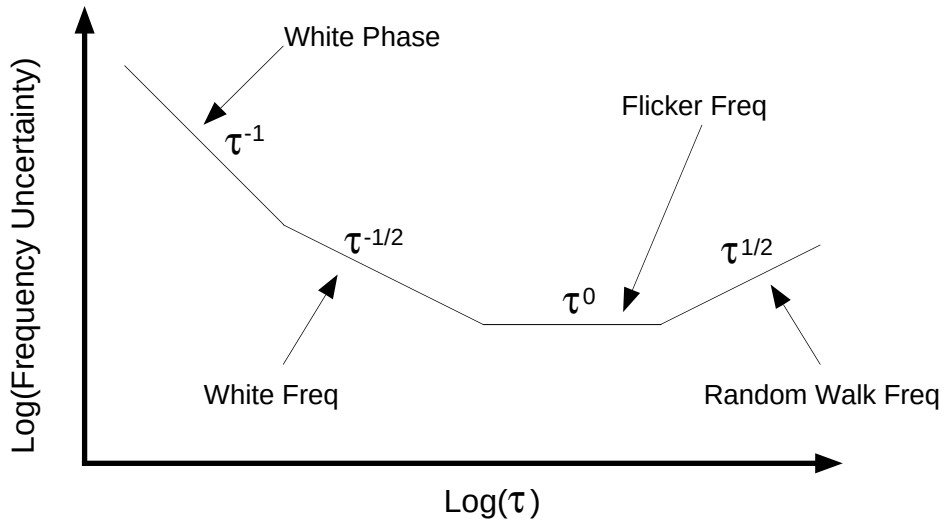

Figure 4.1: Frequency uncertainty of a generic precision oscillator as a function of observation time for various types of noise and fixed bandwidth

both in the limit of large N. Therefore, the frequency precision is determined by the observation time τ and the noise that sets the uncertainty in the individual data points. It turns out that statistical noise for a precision oscillator is often well modelled by power law spectral densities [38]. Consider figure 4.1, which plots precision versus τ. The plot has several sections with different slopes: each slope is considered a different type of noise. For observation times less than 5000 seconds the masers are generally dominated by phase noise (trending as $\tau^{-\frac{3}{2}}$, see below) and frequency noise ($\tau^{-\frac{1}{2}}$) . There are several potential sources for each of these types of noise, as explained below.

The first kind of noise to consider is phase noise. Most of the phase noise in the system arises from the magnetic field fluctuations in the solenoid current that are faster than the control loop can manage. Such fluctuations could be the result of the vibration of the pick-up coil with respect to the cell or high voltage discharges. Another source of white phase noise is the temperature fluctuations of the pick-up coils. This thermal noise of the coil (so-called Johnson noise) introduces a frequency uncertainty of [39]

$$\sigma_\nu = \frac{1}{2\pi\tau}\sqrt{\frac{\mathrm{k_B T\,bw}}{\mathrm{W_{ng}}}} \tag{4.3}$$

for a fixed bandwidth bw; since our bandwidth effectively decreases with time our

precision actually goes as $\tau^{-\frac{3}{2}}$ (W_{ng} is the steady state output power of the maser). However, a quick evaluation of equation 4.3 reveals that the Johnson noise is only a small fraction of the total phase noise.

Next to be considered is white frequency noise. This is caused by blown air moving the pick-up coils within the solenoid's field, by picking up external noise, and also thermal contributions arising from the blackbody radiation of the resonant coils. This radiation interferes with the feedback generated by the coils and causes fluctuations in the magnetic field. The uncertainty from such thermal white frequency noise is [39]

$$\delta\nu_{ng} = \frac{\gamma_{ng}}{\pi}\sqrt{\frac{k_B T}{2W_{ng}\tau}} \tag{4.4}$$

The method used to quantify the precision is the Allan Deviation (or Allan Variance), which is just the standard deviation of the point-to-point frequency differences

$$\text{Allan Deviation} = \sqrt{\frac{\sum_{i=1}^{N}(x_i - x_{i-1})^2}{2(N-1)}} \tag{4.5}$$

Figure 4.2 shows the Allan Deviation of the two species versus τ. The lower data set is for the noble gas used to stabilize the magnetic field: it therefore compensates for frequency noise sources (and some phase noise sources), and trends down as $\tau^{-\frac{3}{2}}$. The upper set is for the data used for an EDM measurement. It trends as $\tau^{-\frac{1}{2}}$ beyond 100 seconds or so. Experimentally, it is clear that the EDM measurement is dominated by white frequency noise.

Note that an EDM measurement can be made with either species "phase-locked", leaving the other "free-running". This is a result of the magnetic field lock loop. If B is locked to the helium, and the applied electric field shifts the xenon frequency, then this change is seen directly in the free-running xenon species. If instead B is locked to the xenon, the electric field still affects the xenon. However, the magnetic lock loop immediately compensates, so the observed result is a change in the helium frequency. Since the helium gyromagnetic ratio is larger than that of xenon (by a factor of 2.754080286 [68]), the absolute shift is actually larger when locked to the xenon than to the helium. Of course, this assumes that the lock-loop performs equally well for either species, with their different amplitudes and frequencies: this

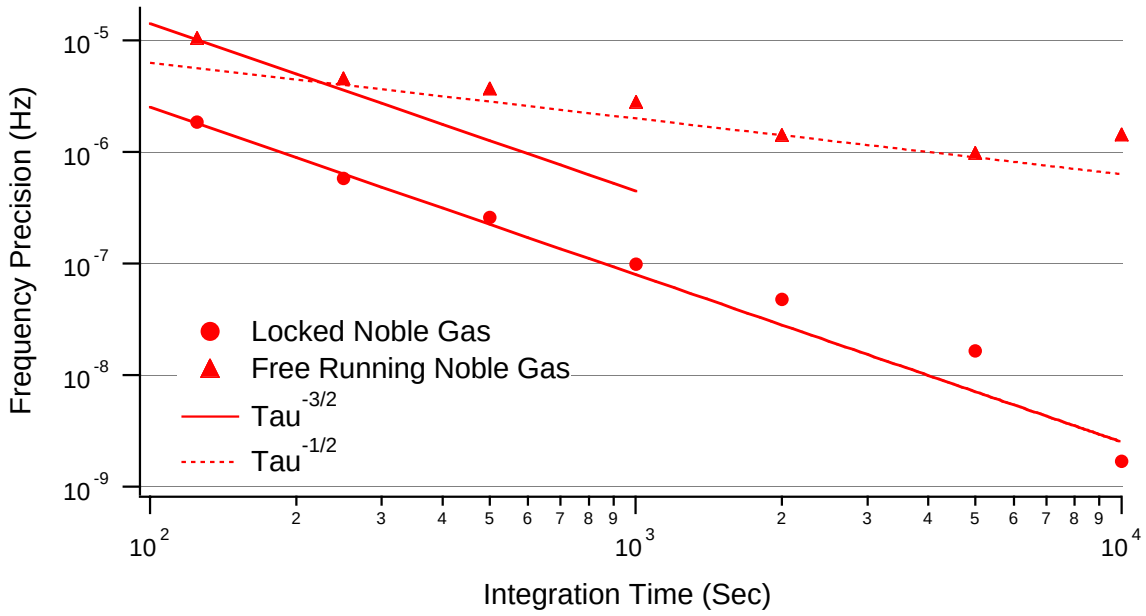

Figure 4.2: Allan Deviation of Typical Data Set

assumption has been confirmed experimentally. Therefore the xenon is the phase-locked species in all the EDM data-taking runs.

Ultimately the stability is limited by the quality of the reference frequencies being used. To determine this, one has a "clock run", a data set where the "data" is generated by two sets of DS-345 synthesizers beating against one another. In this case the precision trends as τ^{-1}. Such a trend indicates that the frequency synthesizers have a fixed phase error with time. The downward trending levels out at the ultimate precision of the DS345's, which is around 5×10^{-9} Hz. This is sufficiently low to have no effect on the free-running species, though it makes a discernable contribution to the phase-locked maser stability at long tau.

4.2 Frequency Shifts

4.2.1 E-dependent Effects

The most dangerous error in the system is one that mimics an EDM, causing a shift that is correlated with the electric field. This could cause the system to perceive an EDM that did not exist, or mask an EDM that was truly present. Fortunately,

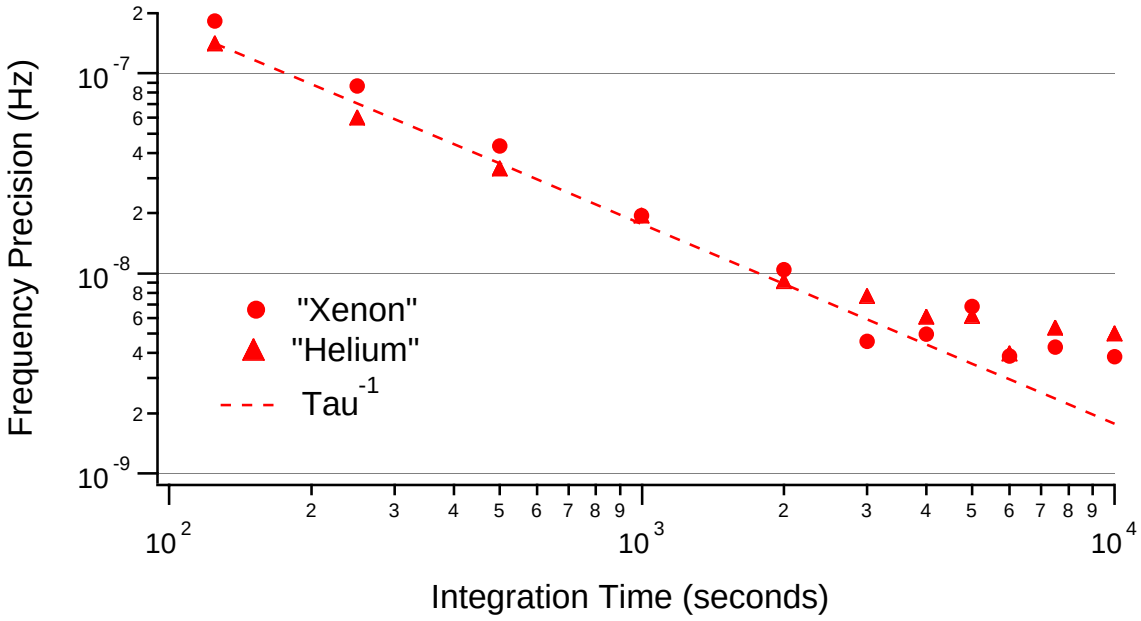

Figure 4.3: Allan Variance Plot of a Clock Run

there are only a few ways that this can occur. The most important of these is a leakage current that wraps at least partially around the cylindrical maser bulb. To estimate the size of this effect, consider the additional magnetic field generated by a single loop around the cell.

$$\mathrm{B_{leak}} = \frac{\mu_o \mathrm{I}}{2\mathrm{R}} \tag{4.6}$$

in the direction of the applied E field. Using the cell's inner radius of 0.25 inches means that it requires a one amp current to obtain a one gauss field.

$$\mathrm{B_{leak}} = \frac{(1.26 \times 10^{-02}\mathrm{Gs\,m/A}) \times (1\mathrm{A})}{0.0127\mathrm{m}} = 0.989\mathrm{Gs} \tag{4.7}$$

It is not possible to measure the actual path of the leakage current, but its maximum value is known. Furthermore, locking to the second noble gas species compensates for this effect to the extent that one species determines the frequency of the other. Two separate tests were performed to determine how effectively the lock-loop compensated for the leakage current.

In the first test, the magnetic field was changed by up to 1 mG and the corresponding changes in the ratio of the noble gas frequencies were recorded. The

difference between the measured ratio and the known ratio was 20 μHz/mG, mostly due to difficulties in fully compensating for cavity pulling effects (refer to section 4.2.4 below). Still, since the typical leakage current values in the EDM runs are 200 pA, this means that the frequency error after the control circuitry is no larger than

$$\Delta\nu_{err} = 200\text{pA} \times \frac{1\text{Gs}}{1\text{A}} \times \frac{20\mu\text{Hz}}{\text{mGs}} \tag{4.8}$$

This introduces a frequency error of 4 pHz, or about 4 $\times 10^{-31}$ e cm for an EDM measurement. This is quite negligible. However, this test assumes that the additional magnetic field will be extremely uniform across the entire cell, which is not actually the case.

The second test for leakage current shifts was more direct. A single wire was wrapped around the outside the maser bulb of the cell. The field that the wire generated was calibrated from the frequency shifts observed when the system was off-resonance. Then the system was turned on-resonance, the masers were locked up, and the change in frequency was determined for a set change in the wire current. The result is no more than 50 μHz in the He maser (with the xenon phase-locked) for a current of 1 μA (which corresponds to a 4 mHz change in the He with no phase-locking). Using this, a 200 pA leakage current means a 10 nHz change in the He frequency, or a change of 10^{-27} in the xenon EDM. This is much larger than the effect measured above, but still below the statistical error of the EDM experiment. Furthermore, as explained in Chapter Five, 200 pA is a very generous overestimate of the current that actually travels across the cell; 20 pA is much more reasonable.

Another mechanism that could generate an E dependent shift would be through a change in the diamagnetic shielding. This shielding reflects the screening of the applied magnetic field due to the atom's electrons. The result is that the atom's observed magnetic dipole moment is slightly different from the true nuclear magnetic dipole moment [33]

$$\mu_{obs} = (1 - \sigma)\mu_{true} \tag{4.9}$$

The shielding constant σ is quite small, being 6.00×10^{-5} for ^{3}He and 7.04×10^{-3} for ^{129}Xe. In most cases its effects can be ignored, because the observed moments are the measured quantity in any case. However, if σ changes as a function of the electric field, then there is a problem. The precession frequency of both noble gas species

would now shift with E. Furthermore, since the helium and xenon frequencies may change to a different degree, the second species magnetometer may not compensate for the effect.

Determining the dependence of $\sigma(\mathrm{E})$ is a complex theoretical task. However, the systematic checks of the maser frequency versus E^2 indicate that the difference between the two electric field directions is well below our statistical precision. See Chapter Five for more details.

There is a third effect that can theoretically cause a frequency shift that correlates with E. This is the motional magnetic field effect. Recall that a particle moving with respect to a static electric field sees a magnetic field in its frame of reference given by

$$\mathrm{B_m} = \frac{\vec{\mathrm{v}} \times \vec{\mathrm{E}}}{\mathrm{c}^2} \tag{4.10}$$

in SI units. Given that the experiment is in a sealed cell at rest with respect to the electric field, the average v is zero. However, it has been pointed out by Lamoreaux [56] that the motional magnetic field will still contribute for times short compared to the collision time of the atoms. These extremely rapid fluctuations do wind up contributing to the atomic frequencies at some level, adding an amount

$$\Delta\nu = \left\langle \frac{\gamma {\mathrm{B_m}}^2}{2\mathrm{B_\circ}}(1 - \cos(2\pi\nu\tau_c)) \right\rangle \tag{4.11}$$

where the brackets denote ensemble averaging and τ_c refers to the time between collisions. For our cell, τ_c is far smaller than the atomic oscillation period, and the shifts are about 8×10^{-17} Hz for the He and 8×10^{-18} Hz for the Xe. Thus this effect can be ignored entirely.

4.2.2 Magnetization Shifts

One concern for uncertainties in the measurement are changes in the frequencies due to the magnetic fields generated by the atoms themselves. These turn out to be a major source of instability in the system. There are many effects to keep track of, because the longitudinal and transverse polarizations of each species act on both the maser ensembles. In addition, the polarized rubidium will shift the masers, particularly the xenon. Since the phase-locking cancels out fields that both species

perceive equally, some but not all of the shifts in the maser bulb are eliminated. The phase locking completely eliminates shifts due to magnetization in the pump bulb.

In this section I assume that the magnetization of each species is uniform within the maser bulb. This ignores the effects of the walls and the pick-up coils, both of which introduce a modest spatial dependence to the magnetization vector. It also assumes the validity of the classical picture for an ensemble of atoms.

The system is measuring a precession frequency of the atomic magnetic moment ($\vec{\mu}$) around the static field $\mathrm{B}_\circ\,\hat{\mathrm{z}}$. The precession is caused by the torque, $\vec{\mu} \times \vec{\mathrm{B}}$, but the precession frequency does not depend on the angle between $\vec{\mu}$ and $\vec{\mathrm{B}}$. This is in exact analogy to a gyroscope. When the field due to the atoms in added in, the direction of the field changes slightly. This alters the torque, but since the added field is generated by the atoms is much smaller than the solenoidal field, it shall be assumed that the z axis will remain unchanged. Using the principle of superposition to look at the effect of just the atomic B, the shift in the precession frequency is found to be

$$\Delta\nu = \frac{|\vec{\mu} \times \vec{\mathrm{B}}_{\mathrm{atoms}}|}{\mathrm{I}\sin\theta} \tag{4.12}$$

where θ is the angle between $\vec{\mu}$ and the z axis.

$\vec{\mathrm{B}}_{\mathrm{atoms}}$ can be further broken down into the field generated by the same species (self-shift) and the field generated by the other noble gas species (cross-shift). The cross-shift, or the effect that one species has on the other, is the easiest to calculate. Since the transverse magnetizations precess at very different rates, in the rest frame of one species the magnetization of the other appears to rapidly precess around z. Over many cycles, the species at rest tends to principally see just the longitudinal component of the other, shifting the frequency an amount $\gamma\,\mathrm{B_L}$.

In the calculation of the self-shift, one finds that the transverse magnetization does not average away. In fact the transverse component torques the magnetic moment in the opposite direction to the longitudinal one. Thus the self-shift can be written

$$\Delta\nu = \gamma(\mathrm{B_L} - \mathrm{B_T}\frac{\cos(\theta)}{\sin(\theta)}) \tag{4.13}$$

Note that for a spherical cell, the magnetic field is always aligned with the magnetization. In this case $\mathrm{B_L} = \mathrm{B_T}\frac{\cos(\theta)}{\sin(\theta)}$ and the self-shift is zero, a result that can be

found by integrating the field of a dipole over a sphere.

The EDM cell I employ is cylindrical. This gives me a uniform electric field, but now the magnetic field generated by an arbitrary magnetization will not be parallel to **M**. This is because an infinitely long cell with uniform magnetization along the axis has a field $B_L = \mu_\circ M$, a known result of elementary electrodynamics. For the same cell with a transverse magnetization, the field is $B_T = \frac{\mu_\circ M}{2}$. Thus the total magnetic field vector is closer to the axis of the cylinder than the magnetization vector.

Of course I am not using an infinitely long bulb. The maser bulb has a diameter comparable to its length: therefore corrections need to be made to the idealized case. A numerical integration program was written to find the field at each point within the cell and then the average field over the cell. The result for the present maser bulb (L=2.0 cm , D=1.27 cm) is $B_L = 0.778\,\mu_\circ\,M_L$, still not far off from 1. The transverse field is $B_T = 0.611\,\mu_\circ\,M_T$. Since the transverse magnetization is just $\mathbf{M}sin(\theta)$, the self-shift can be rewritten as $\gamma(0.778 - 0.611)\,\mu_\circ\,M_L$.

In the absence of phase locking, the combined self-shift and cross-shift of the two species are

$$\begin{aligned} \Delta\nu_{Xe} &= \gamma_{Xe}\mu_\circ((0.778 - 0.611)M_L^{Xe} + 0.778M_L^{He}) \\ \Delta\nu_{He} &= \gamma_{He}\mu_\circ((0.778 - 0.611)M_L^{He} + 0.778M_L^{Xe}) \end{aligned} \tag{4.14}$$

The effect of phase locking is to keep the locked species at constant frequency, so only the free-running species will shift. If xenon locking is employed, then the observed helium shift is

$$\begin{aligned} \Delta\nu_{obs} &= \gamma_{He}\mu_\circ[(0.778 - 0.611)(M_L^{He} + 9.78M_L^{Xe}) - (0.778 - 0.611)(M_L^{Xe} - 9.78M_L^{He})] \\ &= \gamma_{He}\mu_\circ(0.611)(M_L^{Xe} - M_L^{He}) \end{aligned} \tag{4.15}$$

For helium locking, one must instead use γ_{Xe} and change the sign.

Note that phase-locking has cancelled out the longitudinal fields, because both species are affected by these. Only the transverse fields, which only affect the frequency of their own species, wind up contributing to the result.

The polarizations were determined in section 3.6, and from these the magnetizations are easily obtained (see equation 3.12). The values calculated for the observed

(helium) shift when both species are off-resonance are about +80 mHz due to the xenon magnetization and -90 mHz due to the helium. On-resonance, the shifts should be smaller: +5.5 mHz for the Xe and -18 mHz for the helium. Since the spatial averaging shift (described in the next section) is also dependent on the magnetization size, both effects are combined before being compared to experimental results: read on for details.

Be aware that the averaging out of the transverse cross-term is not perfect, though it was small enough to neglect in the above discussion. The effect can be viewed as a small correction, and can be found using the formula given by Ramsey [70] for the shift away from the Larmor frequency due to a rotating field at frequency ν_T

$$\Delta\nu = \frac{(\gamma \mathrm{B_T})^2}{2(2\pi)^2(\nu_\circ - \nu_T)} \tag{4.16}$$

This gives a -81 pHz shift of the Xe and a 58 nHz shift of the He under masing conditions.

The rubidium in the maser bulb also has an effect on the maser frequencies. Although the rubidium density is very low in the transfer tube, the larger magnetic moment of the rubidium atom partially compensates. More importantly, when considering the shift due to the rubidium there is a multiplicative factor that arises because the polarized rubidium electron and the noble gas nucleus are actually allowed to coexist in the same point in space. The shift is therefore

$$\Delta\nu = \kappa\gamma_{NG}(0.778\,\mu_\circ\,\mathrm{M_{Rb}}) \tag{4.17}$$

where κ is 5 for He and 726 for the xenon [68]. Inserting the maser bulb polarization found in Chapter Three, this corresponds to a 40 nHz shift for the helium and a 2 μHz shift for the xenon (at 40 °C). Although small, this shift is of some concern for two reasons. First, the contact factor κ prevents the magnet lock-loop for compensating for these shifts. Second, the shift is a very sensitive function of the maser bulb temperature, increasing by 50% at 50 °C, for example.

4.2.3 Maser Position Dependence

Inherent in the *in situ* magnetometer scheme is the assumption that the two noble gas masers experience the same average field B. The average B is given by

$$\mathrm{B_{avg}} = \frac{\int \omega_\mathrm{z}(\vec{\mathrm{r}})\mathrm{M_x}(\vec{\mathrm{r}})\eta\prime(\vec{\mathrm{r}})\mathrm{d^3r}}{\gamma_\mathrm{ng}\int \mathrm{M_x}(\vec{\mathrm{r}})\eta\prime(\vec{\mathrm{r}})\mathrm{d^3r}} \tag{4.18}$$

Given the different Q's, polarizations, and densities, one would expect a slight difference even for a single bulb cell and a single pick-up coil. The use of two different pick-up coils exacerbates the problem, and the contributions of the transfer tube increase it still further.

Since the two masers experience slightly different average fields, there will be a frequency shift in one of the species with respect to the other. The size of this shift is found below. The physical separation of the masers will also limit the effectiveness of the phase-locking, and may be a source of the maser instability.

For the off-resonance case, equation 4.18 is integrated over the entire cell volume. The transverse magnetization is generated by the pulse coils, and so it falls steadily in the transfer tube. $\eta\prime$ determines the flux that the pick-up coil intercepts, and so it falls off approximately as a loop of wire along its axis [32].

$$\eta\prime(\mathrm{y}) = \frac{\eta\prime(0)\,\mathrm{R_{loop}^3}}{(\mathrm{R_{loop}^2} + \mathrm{y^2})^{\frac{3}{2}}} \tag{4.19}$$

along the transfer tube axis. The one-dimensional approach is reasonable because the coils are displaced from one another along the y axis, and so it is this dimension that is of most concern.

For the on-resonance case, the limit of integration for equation 4.18 is set by how far the maser ensemble extends up the transfer tube. Essentially, the maser ensemble exists everywhere that $\mathrm{T_2(y)} \geq \tau_\mathrm{rd}\mathrm{(y)}$ (see section 3.3). $\mathrm{T_2}$ and τ_{rd} have only been defined as average quantities, however, so their spatial dependence must now be specified. τ_{rd} is dominated by the factor η, which represents the atoms generating the pick-up coil current that then feeds back to keep the atoms precessing. Each of these terms has a spatial dependence as given in equation 4.19, but when determining the spatial dependence of τ_{rd}, these two steps must be considered separately. Atoms close to the coil will generate most of the current. Then, this current generates

the field seen by all the atoms. The $\tau_{rd}(y)$ written above therefore falls off as the field (k) and not as the product k $\eta\prime$. The spatial dependence of τ_{rd} is as given in equation 4.19.

The T_2 is principally determined by the gradients. These tend to be rather complicated, since the solenoids, the shields, and the polarized atoms all contribute. Once the gradient $\frac{dB_z}{dy}$ is calculated (as described below), the local T_2 in the transfer tube is taken to be proportional to the inverse of the square of this gradient. Putting in the appropriate values, one finds that the xenon maser ensemble extends 3.05 cm from the pick-up coils, and the helium extends 2.6 cm. Note that these limits are with respect to the two different pick-up coils, with the xenon coil being 1.3 cm above the helium. Therefore the xenon is integrated to a point 1.75 cm further up the transfer tube than the helium.

The gradients of B_z were calculated within the cell using the program Biot-Savart (produced by Cirrus Software [14]). The solenoid's field (including end corrections and trim coils, as well as estimates of the effects of the magnetic shielding) gradually increases as one goes further off axis. Added to this was the gradients caused by the atomic magnetizations, calculated as a by-product of determining the magnetization shifts in section 4.2.2 . The fields due to the magnetizations naturally depend on the longitudinal polarization of the atoms, which change dramatically when the system changes from a non-masing to a masing state. In general the fields due to the magnetizations tend to counteract the solenoidal gradients over most of the cell. It is important to note that the magnetization gradients become very strong near the transfer tube as the contributions from the pump bulb and transfer tube become important.

It turns out that in the off-resonance state, most of the gradient comes from near (and within) the transfer tube. Consequently, since the xenon coil is closer to the transfer tube, a larger fraction of its ensemble is at a higher magnetic field. Therefore it sees an average B about 5 μGs higher than what is experienced by the He, corresponding to a shift of about -16 mHz. In the masing state, the stronger contribution comes from within the cell, where the solenoidal fields force the helium to be at a higher magnetic field, and cause an increase of about 30 mHz. (This corresponds to a 1.8 mm separation of the weighted averages of the two maser positions, mostly

due to contributions from the transfer tube. For comparison, if the maser ensembles did not extend into the transfer tube, then the separation would be about 0.6 mm.) Given the uncertainty in the exact nature of the effects of the shielding, the numerical values here may be off by a factor of two or more.

The combination of the two M-dependent calculations, the direct effect of the magnetization shift as well as the change in gradient affecting the spatial shift, can be compared with the measured experimental numbers. Typically, when off resonance the Xe M increases the observed frequency about 5 mHz and the He M decreases it about 9 mHz. Note that these numbers have the predicted signs. On-resonance, the total is a 1.2 mHz increase. This change in sign shows the changing direction of the shift due to maser position. However, the absolute numbers for the off-resonance state seem an order of magnitude off from the predictions, and the components of the on-resonance value do not seem to add up to the experimental result. Part of the problem is the difficulty of properly modelling the maser position shift, which is very sensitive to the gradients in the cell. Recall also the uncertainty in the polarizations (as described in chapter three) that could dramatically affect matters: these values are calculated for the on-resonance numbers from table 3.4.

4.2.4 Other Shifts

Another frequency shift was explicitly seen in the maser equations: the shift arising from cavity pulling. The magnitude is given by equation 3.36. If the difference between the coil resonance and the atomic resonance is small, then we can approximate 3.36 as

$$\Delta\nu_z = \frac{\mathrm{Q}}{\pi \mathrm{T}_2}\frac{\delta\omega_z}{\omega_\circ} \tag{4.20}$$

The crucial parameter here is naturally the amount that the coil is off-resonance, $\delta\omega_z$. This is set by the degree to which I can adjust the capacitors to be in precisely the correct ratio, as well as the thermal stability of the system. Typically the coil resonance is off by a Hz or two on both species: this results in an absolute shift of about 20 μHz. The phase locking can not compensate for this, because the pulling is nearly independent for each species.

The last important shift is that caused by the static gradients across the cell. This

includes gradients of the magnetizations, which are nearly constant under running conditions. The size of the shift is estimated from the shift in a high pressure spherical cell [68]

$$\Delta\nu = \gamma \frac{R^2}{20\pi} \frac{|\nabla B_x|^2 + |\nabla B_y|^2}{B_\circ} \tag{4.21}$$

Calculations indicate that the solenoid introduces a negligible gradient of B_x in the maser bulb and that the gradient of the B_y is completely dominated by $\frac{dB_y}{dz} \approx 2.3\times10^{-5}$ Gs/cm. To this must be added the gradients due to the static (longitudinal) magnetizations of the cell. When these are considered, the total gradient becomes about twice as large. The absolute shift of the helium is therefore about 100 nHz: with the phase lock the effect is undetectable.

4.2.5 Summary of Shifts

A table of the shifts discussed above is presented here. The values are for the masing state in the absence of phase-locking.

Source of Shift	^{3}He	^{129}Xe	Correlates w/ $\vec{E}$	Removed by PLL?
Leakage Current	0.65 μHz	0.24 μHz	Yes	Yes
Diamagnetic Shielding	?	?	Yes	No
Motional B field	80 aHz	8 aHz	Yes	No
M_L^{He}	23 mHz	8.2 mHz	No	Yes
M_L^{Xe}	7.0 mHz	2.5 mHz	No	Yes
M_T^{He}	-18 mHz	-81 pHz	No	No
M_T^{Xe}	58 pHz	-5.5 mHz	No	No
M_{Rb}	40 nHz	2 μHz	No	No
Maser Position	30 mHz	$\equiv 0$	No	No
Cavity Pulling	20 μHz	-15 μHz	No	No
Static Shifts	100 nHz	36 nHz	No	Yes

Table 4.1: Maser Shifts

It is clear that the magnetization shifts dominate all the other effects.

4.3 Sources of Maser Frequency Instability

The previous section outlined the sources of shifts in the free-running maser frequency. As long as these shifts remain constant in time, they have no effect on the EDM measurement. If the shifts change in magnitude, however, the uncertainty will affect the precision. The magnetization shifts are a particular concern, since they are quite large and vary with many different parameters. The cavity pulling can also be a problem, because to first order the change in the shift is not dependent on how well it is initially tuned. Next the effects of the magnet lock-loop on the frequency stability are considered. Finally, experimental checks of correlation between the maser frequency and the maser amplitudes or the temperatures, etc., are presented.

First of all, consider the magnetization shifts. If the drifts in the system are occurring slowly enough that the maser polarizations remain in equilibrium, then the magnetization shifts only change with T_2 or η. (Both the densities and $P_\circ$ do not appear explicitly when calculating the magnetization shifts in equilibrium.) The T_2's are set by the gradients of B_z. Unfortunately, it is difficult to accurately determine these gradients for running conditions. This is because the static field (generated by the solenoid, correction coils, shields, etc.) and the atomic magnetizations both contribute to the gradients. When a cell is first installed, it is tuned up in the "off-resonance" state. Here the T_2 is measured quite precisely, from the exponential decay of the signal. Once the system is put "on-resonance", however, the masers start up, changing the gradients substantially. Since the signal no longer decays, a direct measurement of T_2 is not possible. It can be deduced by determining the P_z, but this measurement is inherently destructive. Therefore one can only estimate the on-resonance T_2 and its change with time.

Indeed, there are many possible ways that the gradients of B_z can change. First of all, there are the trim coils that maximize T_2 in the first place. Fortunately, the optimum trim coil settings have wide maxima, so that a small drift in their voltage has a modest effect on T_2. A typical drift of 1-2 mV will not shift T_2 by more than a few parts in 10^{-5}, which does not shift the frequency discernably. Next there are concerns about the density, which affects the diffusion constants D (discussed in detail in Chapter 3) that determine T_2 (see equation 2.1). Changes in density or

laser power also affect the longitudinal magnetizations of the pump bulb and transfer tube. Although the magnet lock-loop compensates for the fields these generate, the additional gradients are not cancelled. This is why the Coherent laser described in Chapter Two is preferable to the Opto-Power units; maser amplitude drifts with the Coherent are about five times less than when the Opto-Powers are used.

Changes in the coupling between the cell and the pick-up coil can also affect the magnetizations. Given the coils' location, a 1mm shift in vertical position will change the coupling by 4% or so: enough to have a dramatic effect on the maser tip angle. One millimeter would be a large movement, but since the oven is plastic and the cell is held in place with nylon screws and rubber, tenths of a millimeter are entirely possible. Experimental checks show that slow drifts of this type do indeed take place: the rate is something like a 0.03% change in coupling per hour of running. However. the motion is not a random walk: instead it tends to have a constant slope over several days of running. The Allan Variance above (as well as the EDM analysis routine in Chapter 5) are chosen specifically to render harmless the effects of a slow, linear drift such as this.

Cavity pulling is the other frequency shift that can change significantly. The cavity pulling will change if P_z changes, or if the resonant frequency of the coils change. The mechanisms for the longitudinal polarization to change were covered in the discussion above. Changes in the coil resonances can occur in response to changes in the temperature of the tuning capacitors or coils or drifts in the stray capacitance of the wires that connect the two. Even if the system starts perfectly tuned so that the initial cavity pulling is zero, a surprisingly small change in the resonance (one part in 10^5) will cause a 1 μHz change in the cavity pulling for typical T_2 values. Measurements and calculations based on equation 3.36 agree that the free-running helium frequency decreases about 5 μHz when the capacitor box temperature is raised 1 °C (with magnetic field locking). The effects of this are particularly pronounced in first half of the EDM data, before the capacitor box temperature control was built: see Chapter 5 for details.

Another source of frequency instability is variation in the performance of the magnetic lock-loop. The lock-loop performance is partially determined by the size of the locked maser amplitude. As described above, the maser amplitudes are quite

vulnerable to changes in the system. Drifts in laser power or frequency can change the rubidium polarization by several percent overnight. Changes in density can affect the transport rate G_m. The amplitudes in a given cell will also deteriorate as it approaches the end of its lifetime, due to changes in T_1 and the rubidium density. The sum of these effects shows up in the Allan Variance of the locked species, which varies by a factor of two from run to run, even given the same trim coil settings. The change in xenon frequency away from precisely 25 mHz is corrected for in the data: refer to section 5.3.2 for details.

So far, it has been assumed that the masers are operating in their equilibrium state as these drifts occur. As mentioned in Chapter Three, however, the masers may be perturbed from time to time, causing a transient response. If the longitudinal polarization is oscillating, then the maser frequencies will naturally oscillate, for all the reasons discussed above. Therefore, following a glitch, the maser frequencies and amplitudes will both oscillate, though they are 90° out of phase. (In the data gathered, it is easier to look at the phase of the maser, which is 180° different from the amplitude oscillations.) Often, the HV glitch itself is not observed in the collected data, but instead occurred as the electric field was being changed (see Chapter Five for a clearer description of the experimental procedure). Therefore the noise in the electric field can have a substantial effect on the maser stability.

Experimental measurements have determined the extent to which various system parameters change the measured frequency. These tests show that the free-running maser frequency changes by less than 40 μHz per Watt change in laser power (under running conditions). Similarly the frequency shifts less than 30 μHz per degree change in the maser chamber temperature, and less than 35 μHz per degree change in pump bulb temperature. Given the size of the drifts in these parameters in a typical run (see Chapters Two and Five) the maser temperature is usually well below our statistical precision, whereas the pump temperature and laser beam power are sometimes comparable.

CHAPTER V

Data and Results

5.1 Introduction

This chapter is designed to show how the data collected was converted into an EDM measurement. The data-taking and analysis procedures are described in detail. The collected EDM data is presented, along with the results of various systematic checks. Finally the obtained value for d_{Xe} is given.

There were 125 data runs for this experiment, which took place between April and December of 1999. Each data run is considered an independent measurement of the ^{129}Xe EDM, because the system is very sensitive to the conditions of the experiment: room temperature, laser power, etc. These changes cause the size of the systematic effects discussed in Chapter Four to vary on a scale that is large compared to the frequency variation within a run. Therefore, each run is separately analyzed, and the variation of the free-running maser frequency with measured system parameters is determined for every run.

Another reason to treat the runs as independent is that the apparatus evolved somewhat during the data taking. There were several significant changes in the system that tended to improve the performance. The first of these involved the use of the Coherent laser, which was consistently more stable than the Opto-Power units. Some of the Opto-Power runs were quite good, but most of the lower-quality data was obtained using the Opto-Powers. In late July and early August the system ran with only one Opto-Power laser due to a shortage of available units, but the system performance was generally no worse than with two Opto-Powers.

The air flow and temperature control were modified slightly at several points. In June and early July, large fluctuations in room temperature caused problems with the maser chamber temperature control. The temperature was raised from its usual 40-43 °C to 50 °C, then later changed back. Late in July the maser "airflow" was switched over to N_2 to reduce the moisture in maser chamber in hopes of reducing the noise from the high voltage discharges. Also note that due to a lack of equipment, data taken prior to May did not record one or more of the system parameters referred to in section 5.3.1.

Certain runs had high voltage applied to only one plate of the cell. This gave half the usual electric field, which is useful for making checks for systematics that scale with E^2. In addition, these runs allowed a more careful measurement of the leakage current. For some of the runs, the magnetic field was reversed, along with the handedness of the laser light. This served as a further systematic check of the system. By convention, d_{Xe} is positive if it points parallel to the nuclear angular momentum.

5.2 Procedure

The data for this experiment were collected in runs, with each run being a separate measurement of d_{Xe}. A run lasted between seven hours and several days, with most runs being about 24 hours long. Each run consists of 12 or more individual scans. A scan is a section of data taken at one static value for the electric field. During the scan, the lock-ins acquire the in-phase (X) and out-of-phase (Y) traces of the beat frequency for each species. Simultaneously the computer monitors the leakage current and other parameters (refer to table 5.1). When the scan is complete, there is a pause in the data acquisition as the electric field is changed. The electric field alternates in direction, interspersed with periodic scans with no electric field. The pattern is shown in figure 5.1. The "no field" scans occurred after two, three, or four pairs of "live" scans, and are used to look for systematic effects that correlate with the magnitude of E. The sign of the high voltage is the same on either side of a E=0 scan, to reduce systematic effects.

The length of the individual scans was set for optimal performance. Long scans

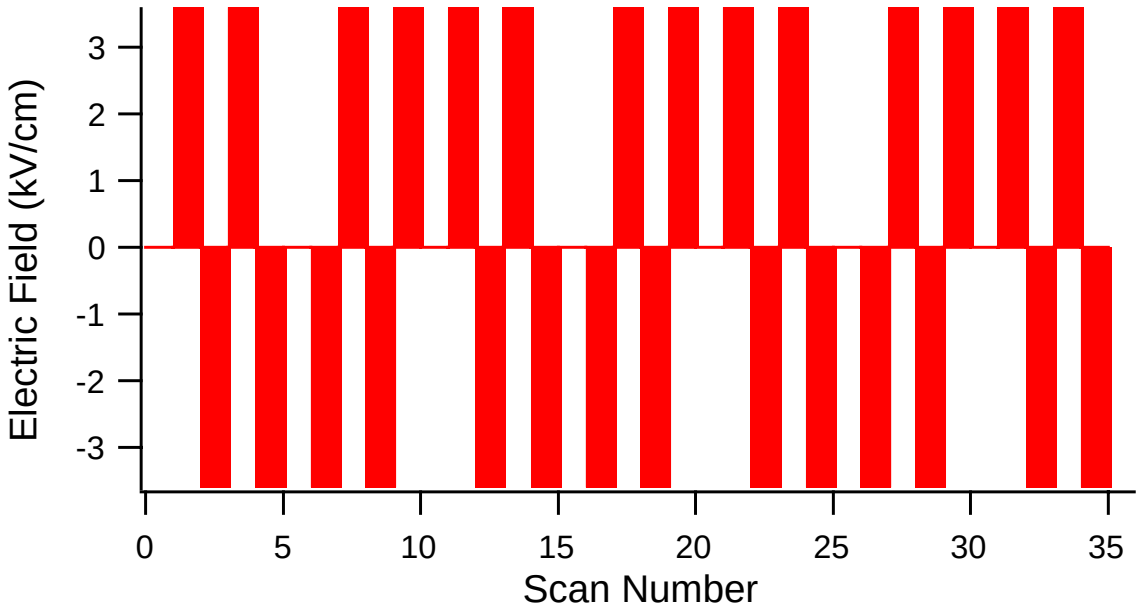

Figure 5.1: Electric field for jun1399

improve the sensitivity, up to some limit, as can be seen from the Allan Variance plot in Chapter 4. More scans mean that the sensitivity improves as $\sqrt{\mathrm{N}}$, where N is the number of scans. Combining these, any scan length between 250 second and several thousand seconds ought to be equally efficient. However, there is the issue of dead time. Approximately seven minutes are needed to change the electric field direction without causing a maser transient. This favors using the longest scan that still falls on the $\tau^{-\frac{1}{2}}$ line to obtain the highest duty factor. The best choice is then a scan length of 2000 seconds, giving 35 scans in a 24 hour period. This length was used for most of the runs taken.

Once a run is completed, the data is saved and analyzed. The analysis of each run proceeds in stages. First, the maser frequencies and other system values are found for each scan. Then, the free-running maser frequency is corrected by partially cancelling systematic effects and removing residual drift. Finally different methods are used to determine an EDM value from the corrected frequencies.

I have selected the run that took place June 13, 1999, to be a typical example of the data, and use it to demonstrate the analysis procedure. This run was taken using the Coherent laser. The magnitude of the electric field was 3.6 kV/cm, and

the pattern is shown in figure 5.1. The run contained 36 scans, each 2000 seconds long. All the examples below were taken from scan 9 of this run, which was selected arbitrarily. For scan nine the electric field was set anti-parallel to the magnetic field.

5.3 Data Analysis

5.3.1 Determining frequencies

As explained in section 2.2.4, the data are the X and Y traces of the beat frequency between the DS345-generated reference frequency and the atomic frequencies. Specifically, take the X and Y traces to be

$$\begin{aligned} \mathrm{X} &= \mathrm{X0} + \mathrm{R}\,\cos(2\pi\,\nu\,\mathrm{t} + \mathrm{X1}) \\ \mathrm{Y} &= \mathrm{Y0} + \mathrm{R}\,\sin(2\pi\,\nu\,\mathrm{t} + \mathrm{Y1}) \end{aligned} \tag{5.1}$$

The traces are generated by the noble gas (SR850) lock-ins. Figure 5.2 shows the helium Y trace for a typical scan. Both noble gas lock-ins acquire data every two seconds, as set by a separate frequency synthesizer. The atomic frequencies are always higher than the reference signal, to insure that a positive shift in the beat frequency means a positive shift in the atomic frequency.

The next step of the analysis is to combine the X and Y traces into a continually increasing phase. This step can introduce spurious noise if the offsets of the amplitude or phase of the X and Y traces are not the same. The data analysis routine therefore removes such offsets before making the phase trace. To do so, the parameters in equation 5.1 are obtained through a non-linear least squares fit to a sine wave. Then the amplitude offsets (X0, Y0) are removed by making new traces

$$\begin{aligned} \mathrm{X}' &= \mathrm{X} - \mathrm{X0} \\ \mathrm{Y}' &= \mathrm{Y} - \mathrm{Y0} \end{aligned} \tag{5.2}$$

These amplitude offsets are inherent to the SR850's that acquires the data.

Next the program checks that X1 = Y1. This is usually the case, but sometimes the SR850 starts one trace one "trigger" ahead of the other. Since the triggers are generated every two seconds, and the beat period is about 40 seconds, this causes

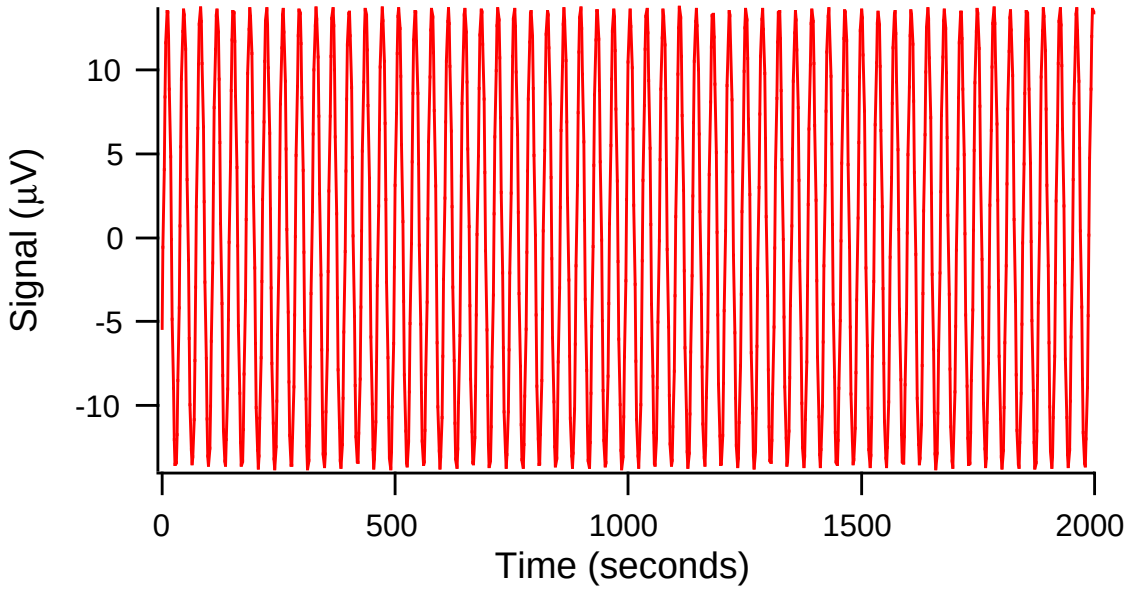

Figure 5.2: Typical Raw Data: Free-Running Maser Y channel

the traces to be about 0.33 radians out of phase. The program solves this problem by deleting the first point from the trace that started early and the last point from the trace that started late. The resulting traces are now just

$$\begin{aligned} X'' &= R\cos(2\pi\nu t) \\ Y'' &= R\sin(2\pi\nu t) \end{aligned} \tag{5.3}$$

Now it is trivial to combine these into a phase, simply by taking the arctangent of (Y"/X"). Each time the phase completes a cycle, the analysis program adds 2π. The program can misinterpret when a complete cycle has occurred if the data is very noisy, but for the noise level of the EDM data taken, the program performed well.

The quantity I wish to measure is actually the frequency. To obtain this, I plot the phase versus time and fit to a line to determine the slope. Figure 5.3 shows the helium phase trace for scan 9 of the jun1399 run. The fit to the data is also included, but the difference between the two can not be discerned on this scale: see figure 5.4 for the difference of the data and the fit.

It is clear that the phases obtained are very nearly linear, reflecting a nearly constant frequency. However, the phase residuals (after a linear fit) were found to correlate strongly with the maser amplitudes. This is not surprising in view of the

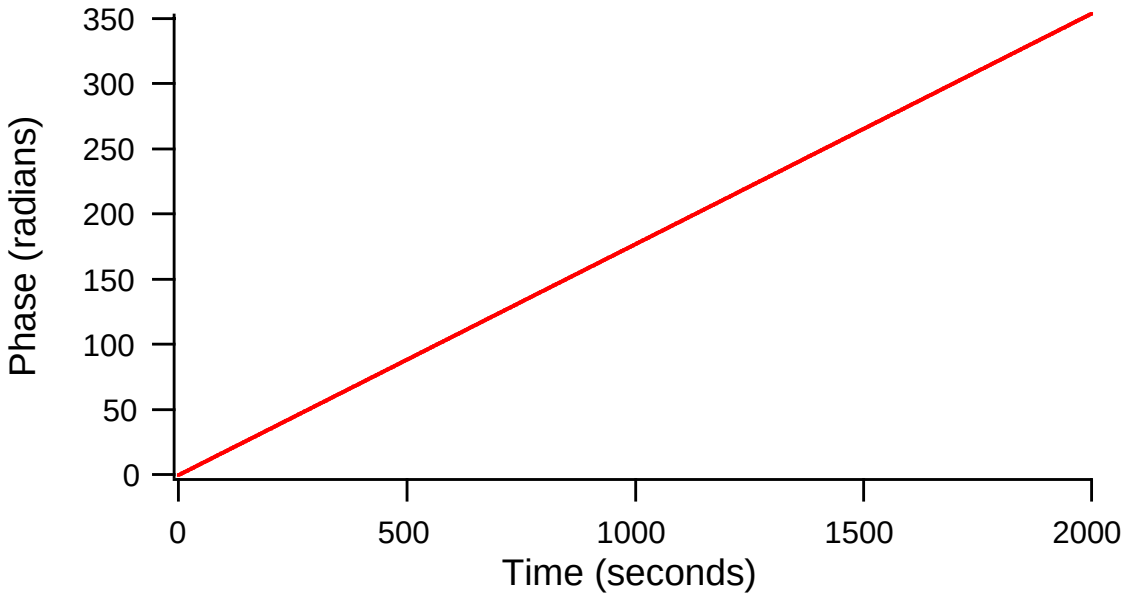

Figure 5.3: Typical He Phase vs Time, With Fit

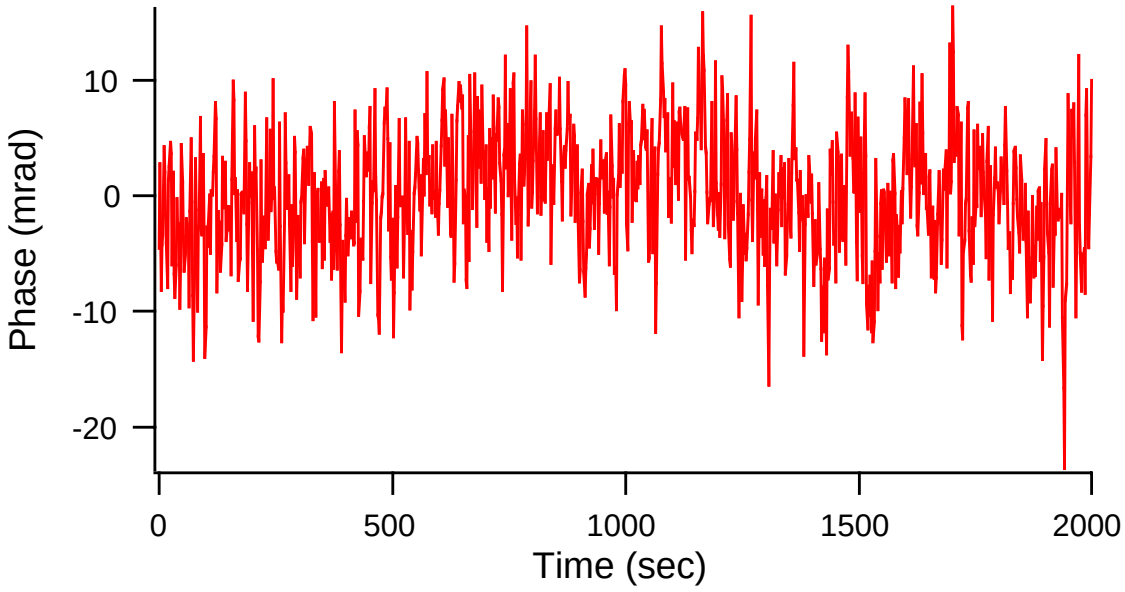

Figure 5.4: He Phase Fit Residual for scan 9, where maser amplitude corrections are used. Sample Rate .5 Hz, Bandwidth .125 Hz

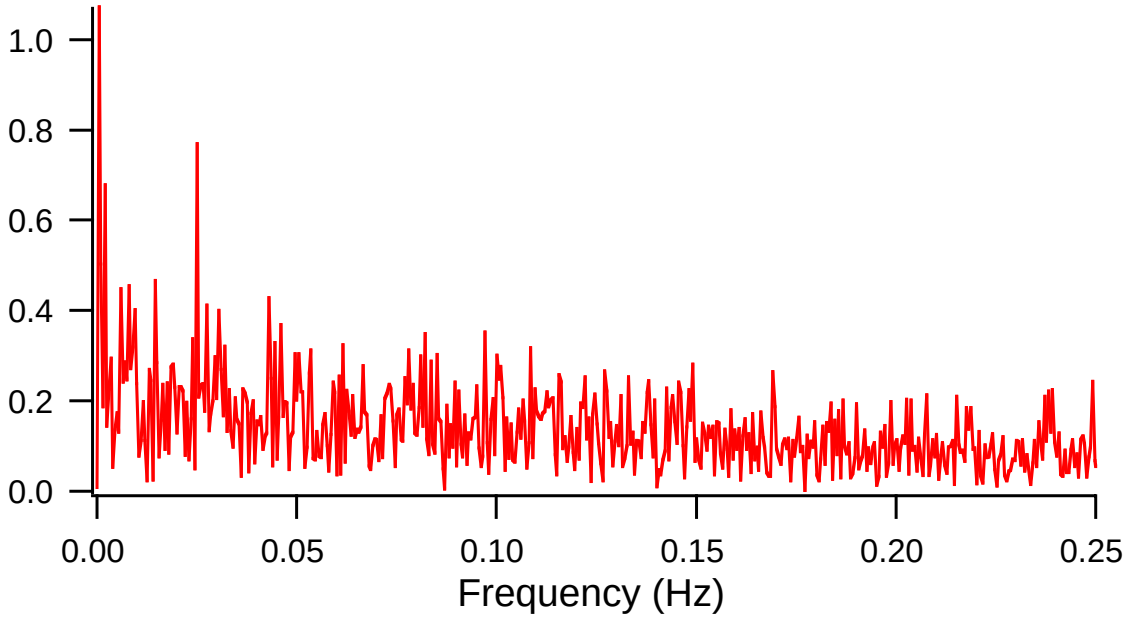

Figure 5.5: FFT of above Phase Fit Residual. The xenon beat frequency (25 mHz) is weak but visible

maser's near equilibrium behavior (refer to section 3.5 for details), but it means that the fits to the line may not be quite correct. In light of this, the helium phase for each scan was fit twice, once to a line and once to a function that combined a line with the maser amplitudes. If adding the amplitudes significantly improved the fit (as determined by the F-test, described in section 5.3.2), then the linear coefficient from the latter fit was used; if it failed the F-test, the linear coefficient was taken from the former fit. In either case the recorded frequency is the coefficient divided by 2 π. For most runs, adding the maser amplitudes significantly improved the fit for about 90% of the scans. For jun1399, the fit significantly improved for 30 of the 36 scans.

In some cases a burst of high voltage noise would briefly disrupt a scan without actually breaking the lock-loop. In this case, the maser phase would jump by an arbitrary amount. When this occurred the longer section of the scan would be fit, and the remaining section eliminated. Such disruptions occurred in about 10% of the runs, and usually for only one scan of that run.

The fit to the phase also gives me an estimate of the error for the frequency, using

the appropriate formula for a linear least-squares fit and assuming that all of the N points of the scan have the same error [4].

$$\sigma = \sqrt{\left(\frac{\sum(y_i - a - bx_i)^2)}{N - 2}\right)} \tag{5.4}$$

Unfortunately, the errors obtained are much smaller than the average change in the frequency (see figure 5.6). Apparently the change in frequency is dominated by

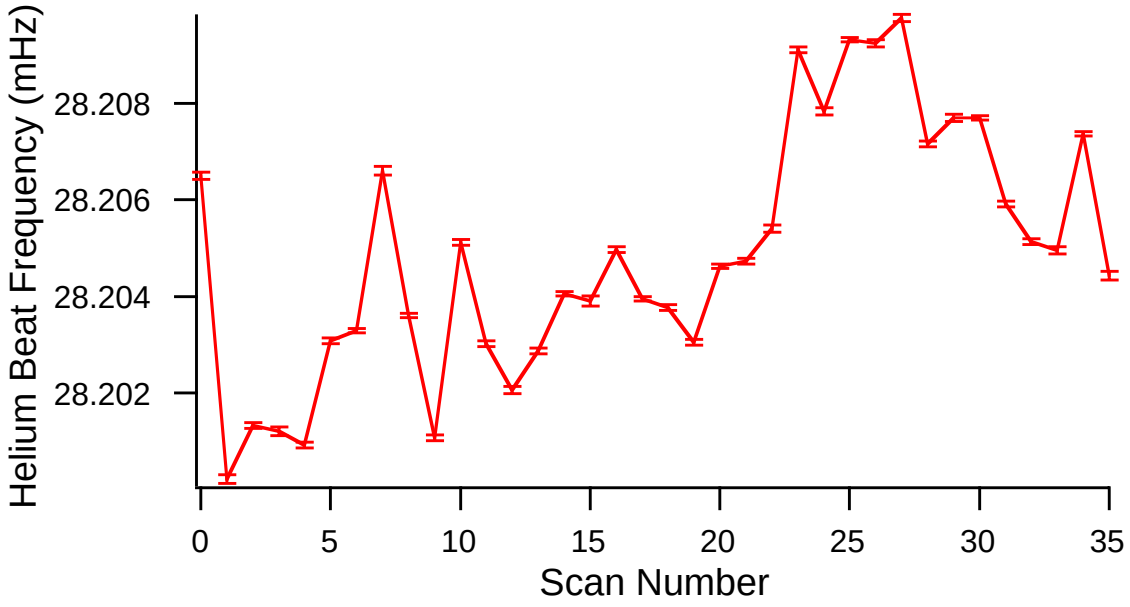

Figure 5.6: Free-Running Maser Frequencies for jun1399, with errors from linear fits to the phase

long-term instability, of order μHz on the scale of hours. Some effects that may be causing this instability will be discussed in section 5.2.2. Since these changes are so much larger than the errors from the phase fit, the latter are considered meaningless and are not used in the analysis, and all data scans are given equal weight.

In addition to the free-running maser frequencies, many other parameters are recorded during the run. These include the locked maser frequency, the temperatures of the pump chamber, maser chamber, and capacitor box, the leakage current, and sometimes the room temperature, laser beam powers and output voltage of the

magnetic field PLL. The locked maser frequencies are determined in exactly the same manner as the free-running frequencies. The other parameters are all recorded by the computer (through HP multimeters), at a rate of between 1 and 6 points per minute. Since there is generally little drift in these values through a scan, the scan is characterized by its average value. Finally, the raw X and Y maser data can be trivially combined to provide the maser amplitudes. These, too, are averaged over the scan.

The first set of graphs presented are for one particular scan of the run. Most of these graphs are quite typical of the data taken. Some scans have a larger or smaller variance, but only by a factor of two. The maser amplitudes are an exception, with drifts four or five times larger being possible when the Opto-Power lasers were employed. The noise seen on the maser amplitudes is mostly white noise from the pick-up coils. In these scans, the leakage current is the only one that is clearly not flat, tending to drift downward as the system settles. The maser temperature does show some oscillatory behavior, but these did not correlate with changes in frequency (see table 5.2 and subsequent discussion), and since the long-term stability was good the problem was not addressed.

The second set of graphs show how the parameters change over the entire run. Remember that the values shown are the average for each scan. Again, the plots are representative of all data runs taken. The locked xenon frequency rarely drifted and had about 20 nHz rms noise, except for a few runs where the magnetic lock-loop was set improperly. The maser amplitudes were somewhat different from run to run, and were less stable when the Opto-Power lasers are employed (refer to section 2.2.2). The correlation between the two amplitudes is even more evident in that case. Both the pump chamber and maser chamber temperatures were constant with time. The pump chamber temperature instability varied from about 15 mK rms to 50 mK rms. The maser was more consistent, remaining between 3 mK rms and 10 mK rms. In earlier runs, including jun1399, the capacitor box temperature varied with the room temperature, and so drifted somewhere between 0.15 °Cpp and 1 °Cpp overnight. Once the capacitor box temperature control system was completed in early August, the box temperature typically remained constant to within 5 mK rms.

The measured leakage current was the one parameter that changed dramatically

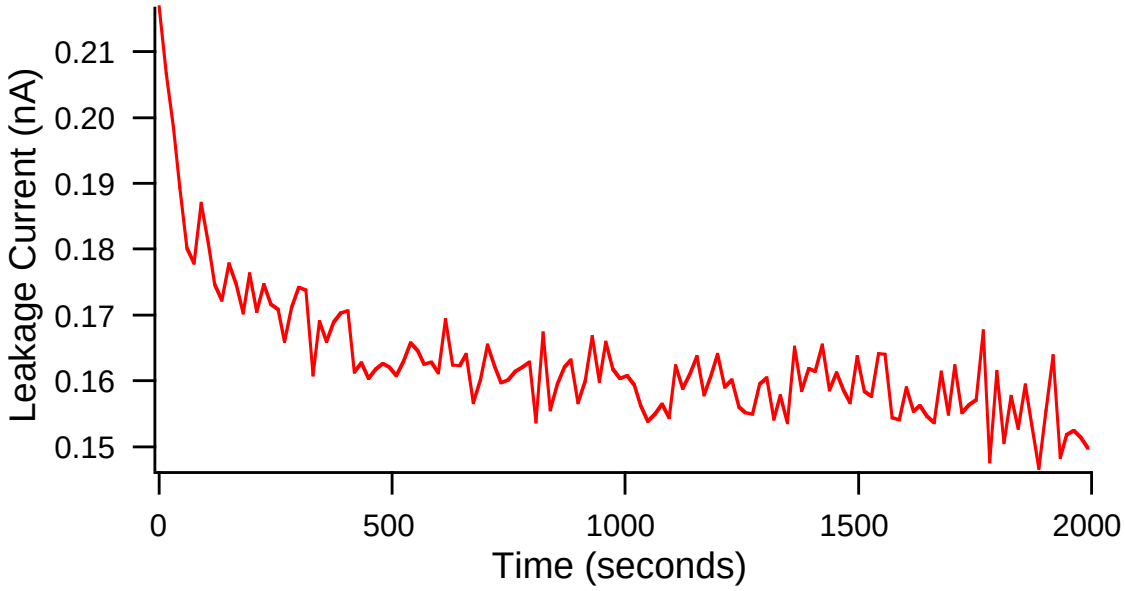

Figure 5.7: Keithley Leakage Current during scan 9

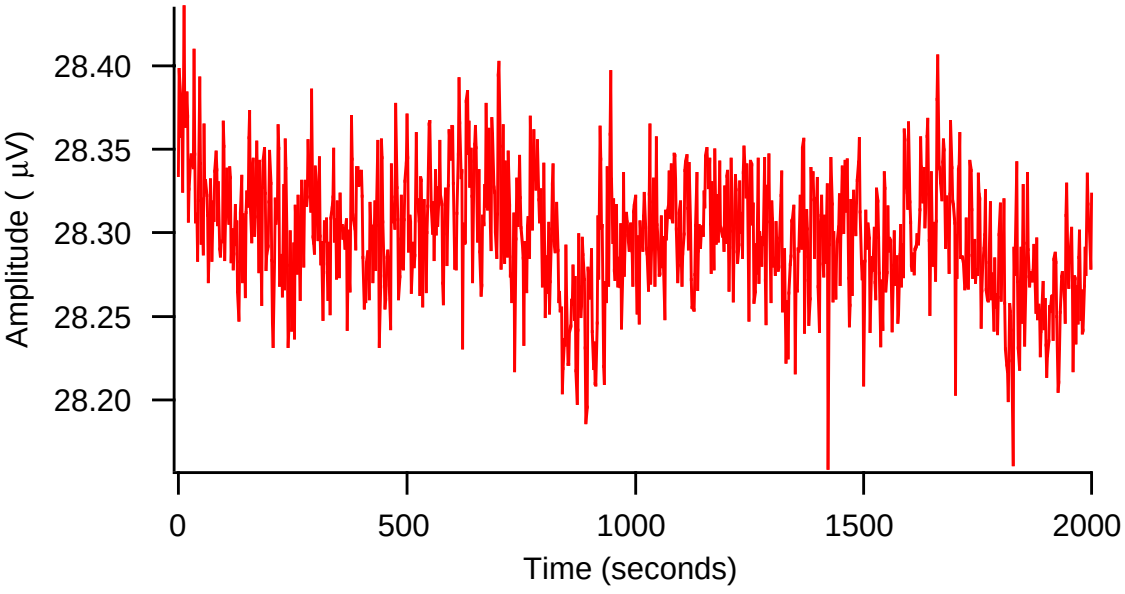

Figure 5.8: Xenon Maser Amplitude during scan 9

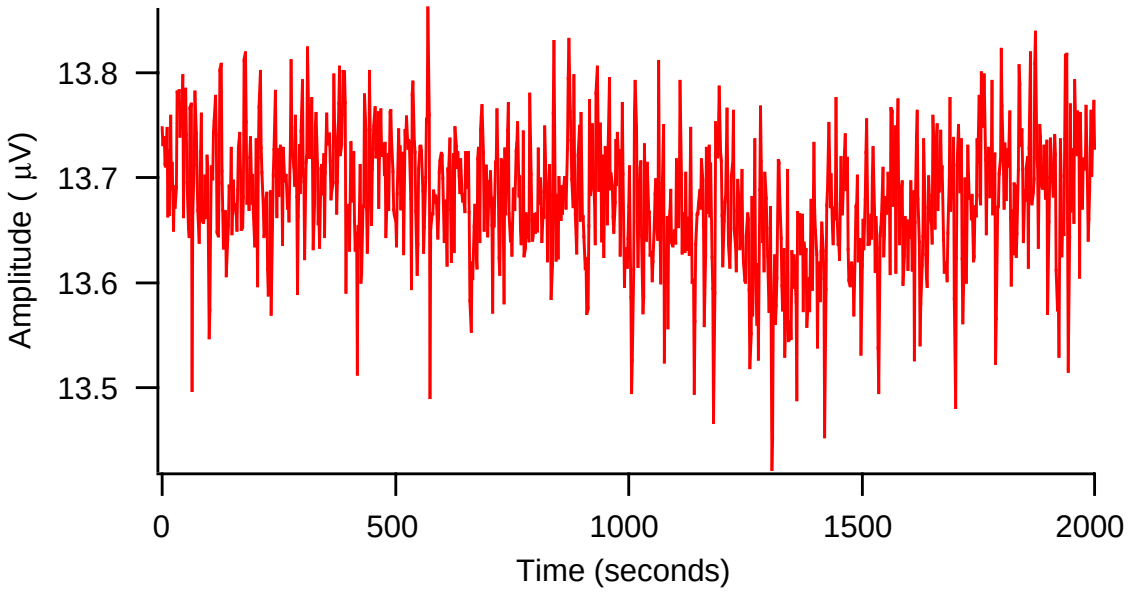

Figure 5.9: Helium Maser Amplitude during scan 9

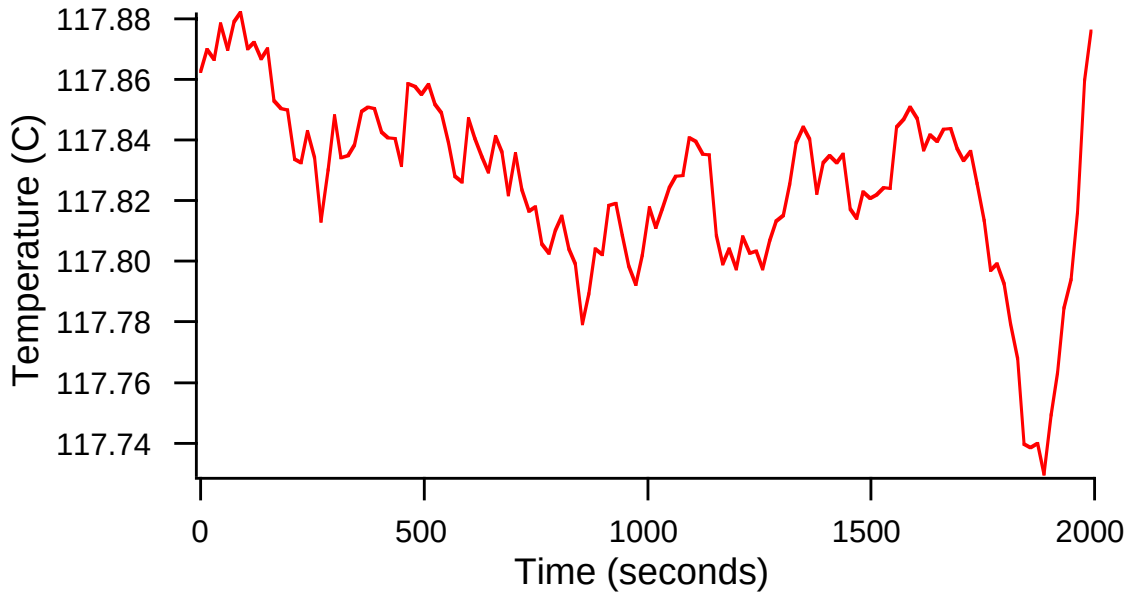

Figure 5.10: Pump Chamber Temperature during scan 9

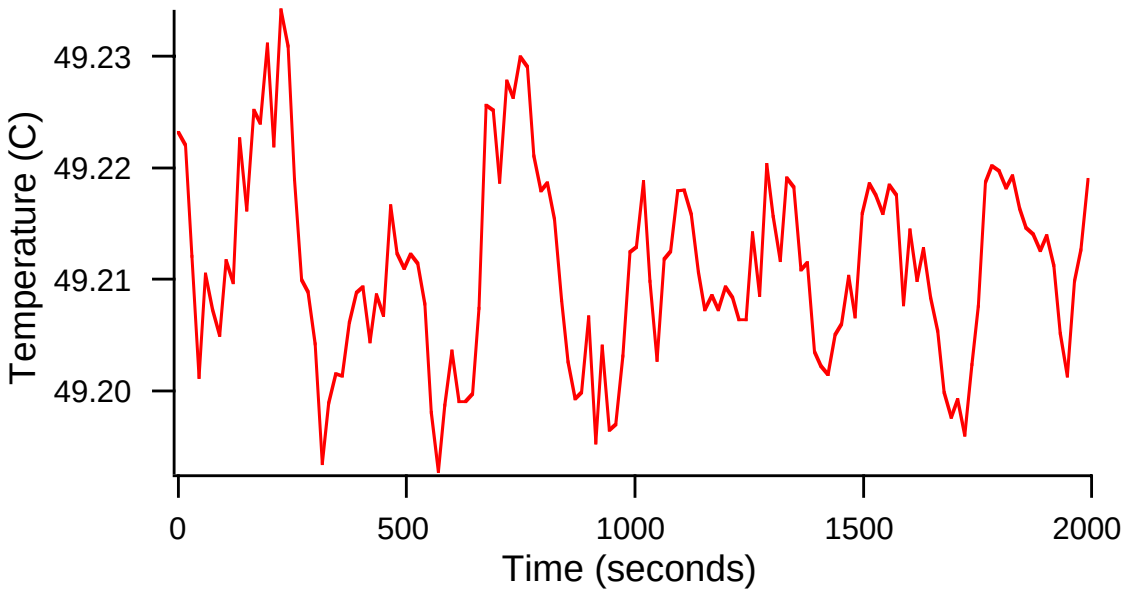

Figure 5.11: Maser Chamber Temperature during scan 9

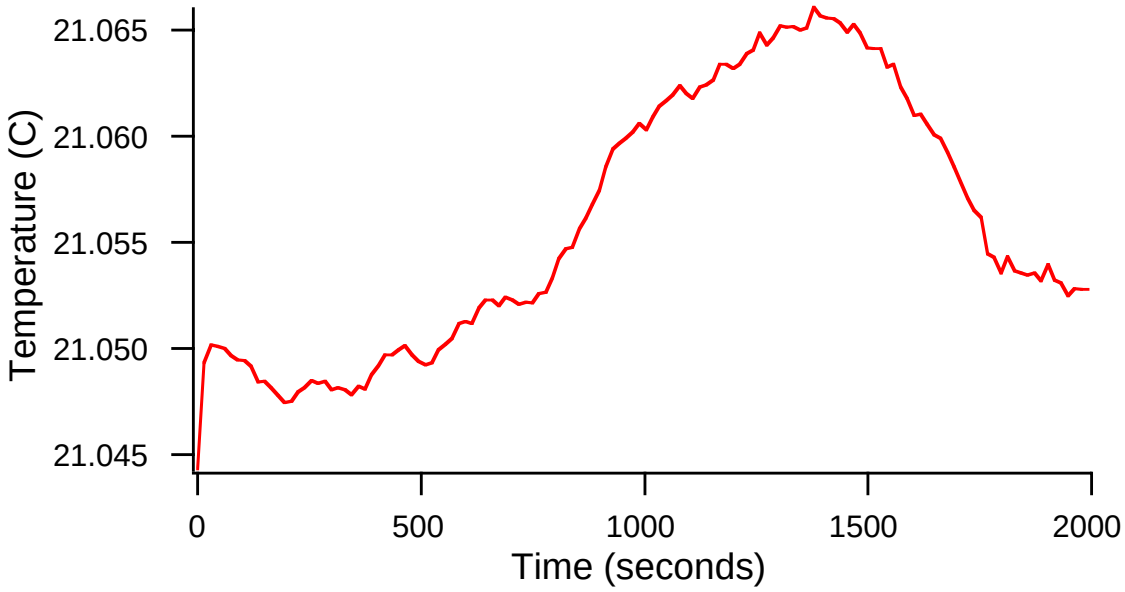

Figure 5.12: Capacitor Box Temperature during scan 9. Since this is prior to implementation of the box temperature control, this drifts with room temperature

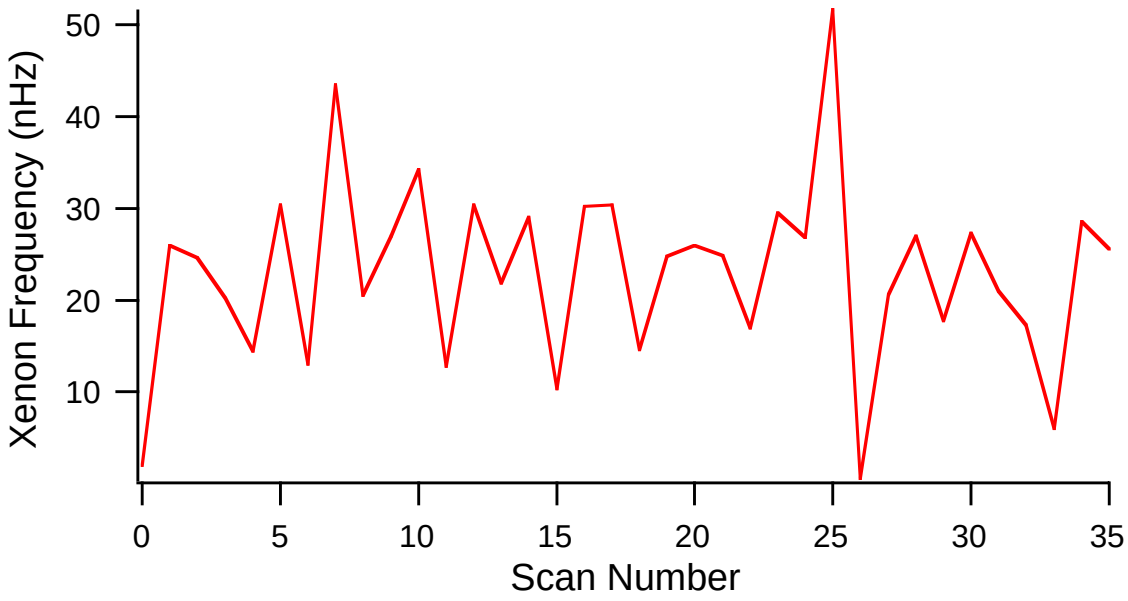

Figure 5.13: Locked Maser Frequency during the run

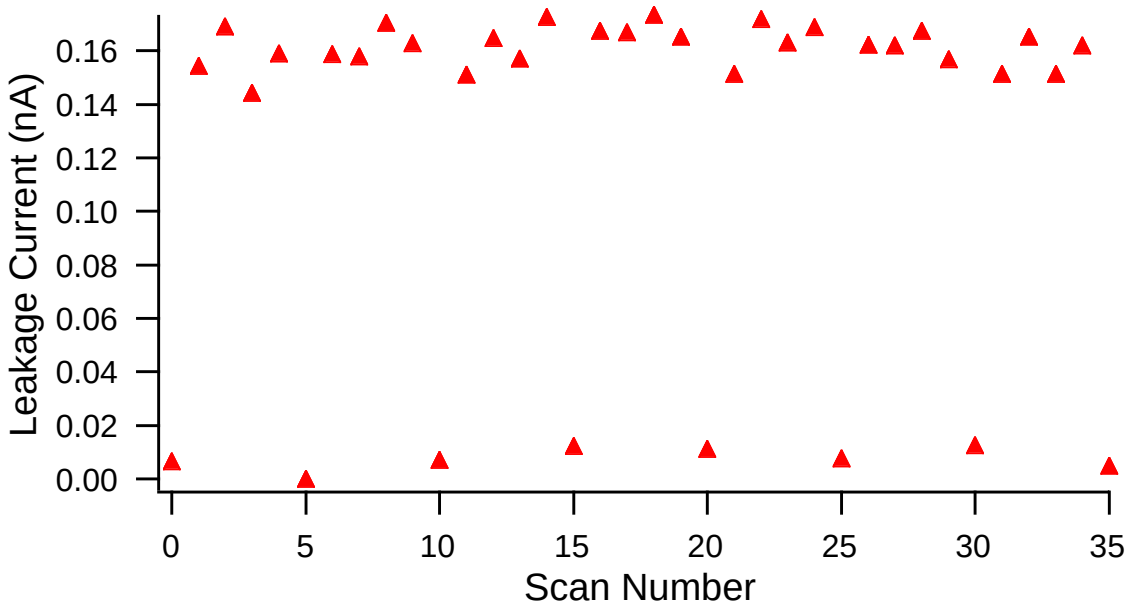

Figure 5.14: Keithley Leakage Current during the run. Refer to figure 5.1 for electric field polarity

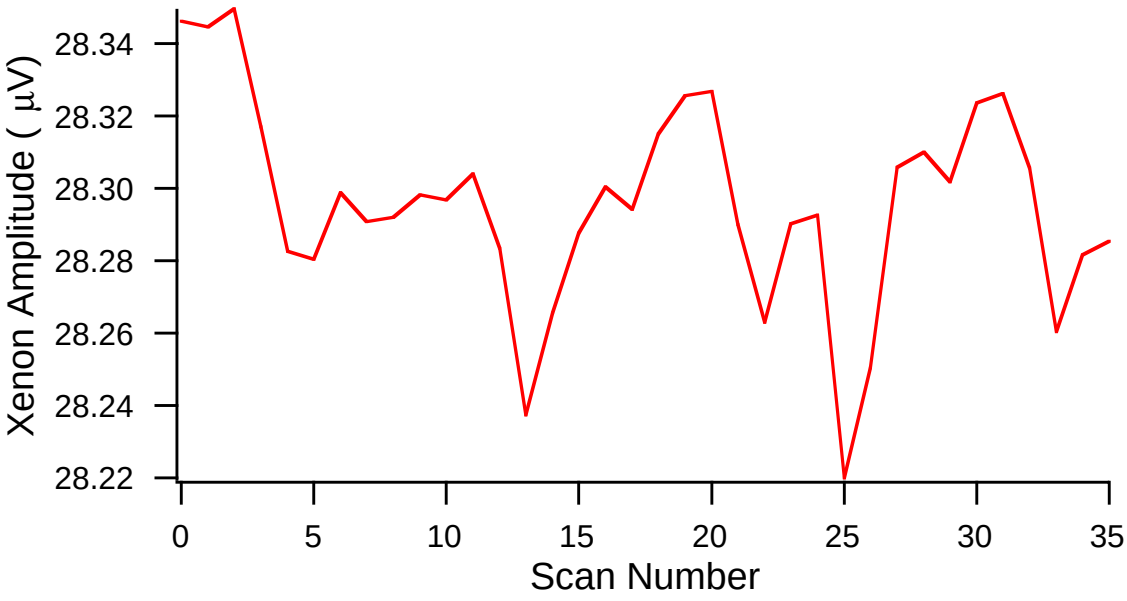

Figure 5.15: Xenon Maser Amplitude during the run

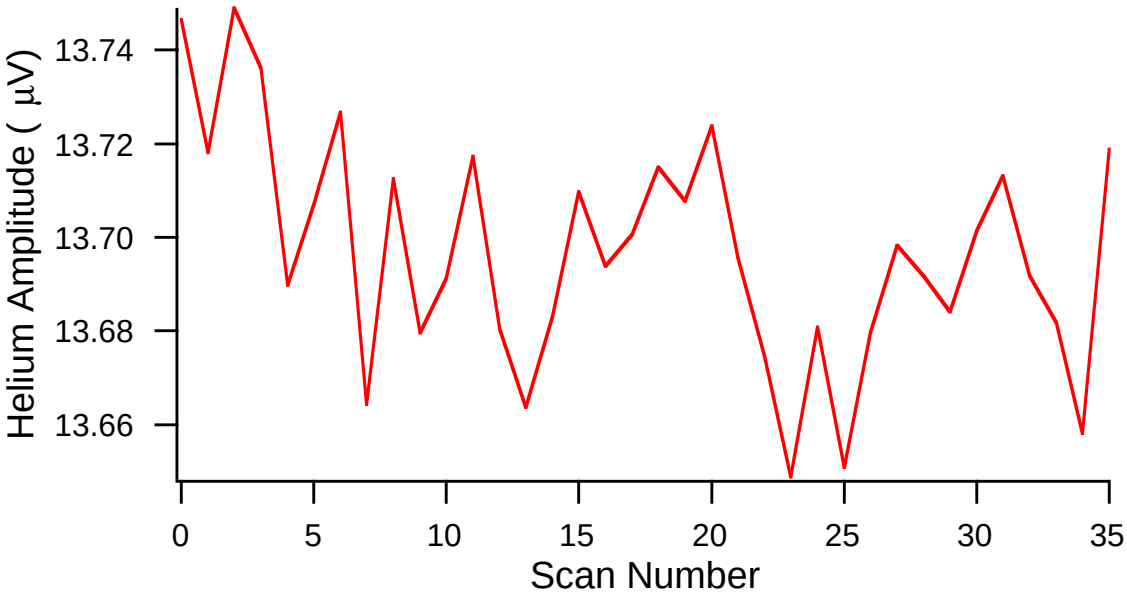

Figure 5.16: Helium Maser Amplitude during the run

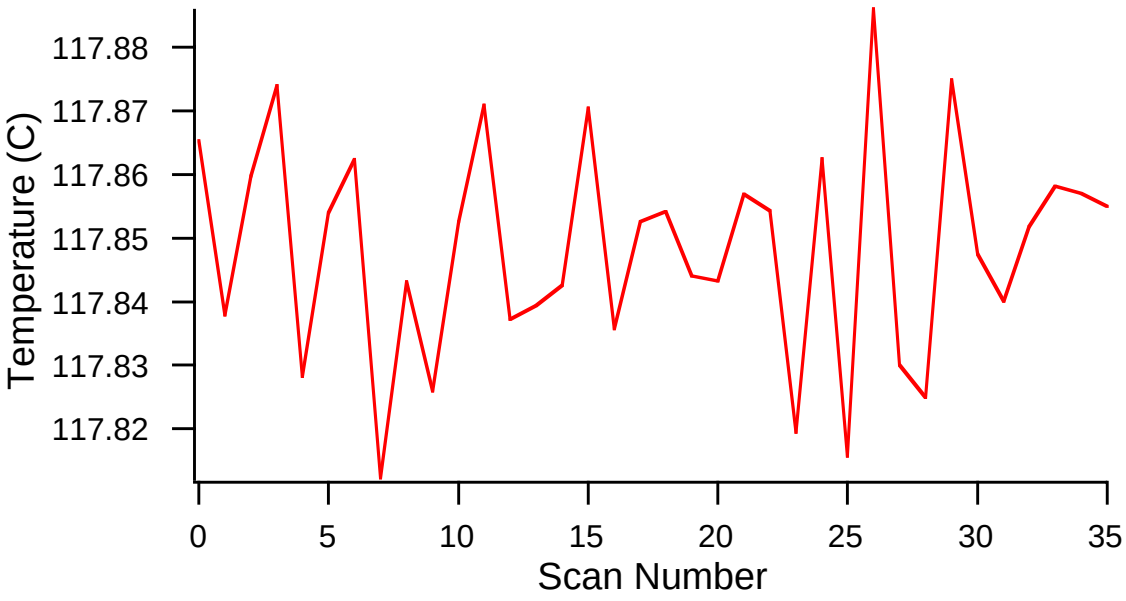

Figure 5.17: Pump Chamber Temperature during the run

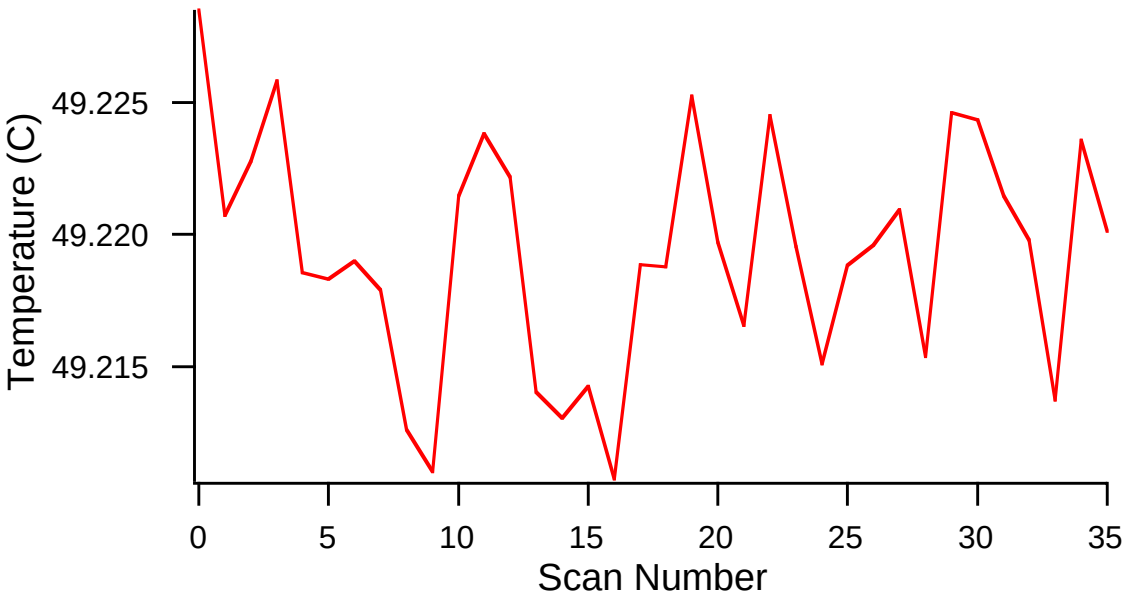

Figure 5.18: Maser Chamber Temperature during the run

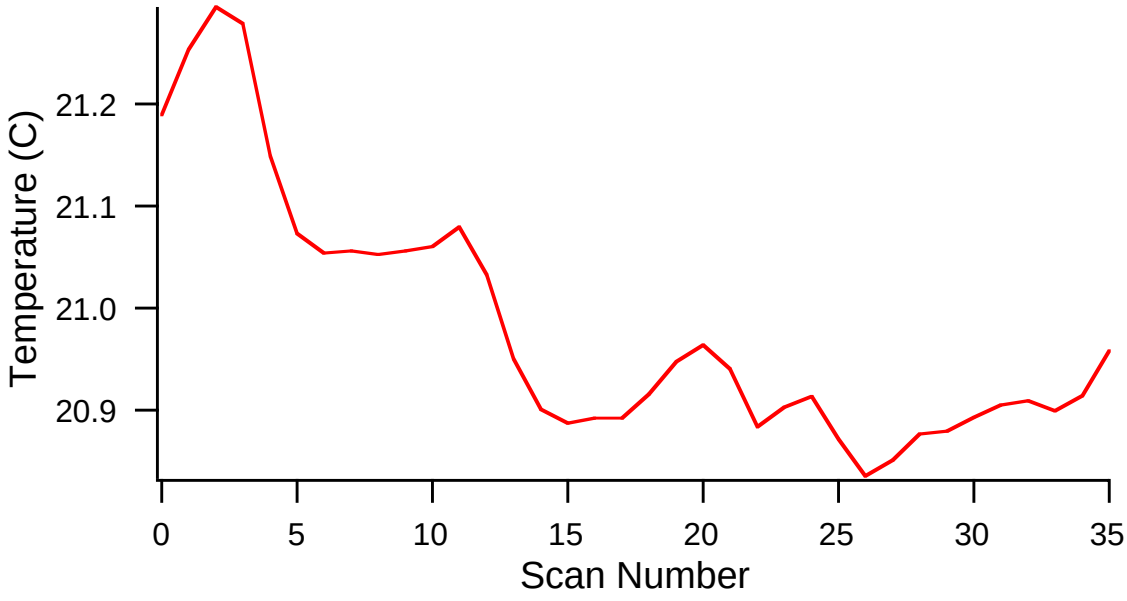

Figure 5.19: Capacitor Box Temperature during the run. Again, this drifts with room temperature.

from run to run. In addition to the room temperature instabilities above, the size of the leakage current would change dramatically as the filter capacitors or new protective diodes were conditioned. In the above run, the size of the leakage current is taken from the dips for the E=0 scans compared to the scans with high voltage. These give a typical leakage current of about 150 pA. Some runs had a measured leakage current of less than 100 pA; a few had up to 7 or 8 nA. However, other experiments have confirmed that most of this leakage actually goes through the capacitors that filter high voltage noise; the capacitors for each side have slightly different properties, as can be seen from the variation in leakage current as the relays are switched. Runs where the high voltage was only applied to one side of the cell show that the leakage current through the cell is less than about 20 pA for a 4.0 kV/cm field. The small amount of leakage current that actually does travel through the cell is probably transported by the OTS coating or rubidium on the glass: the bulk resistivity of the glass itself would limit the current to a few fA. These runs also determined that the leakage current was not linear in E, rising more like a quadratic. This supports the view that much of the leakage is due to the rubidium in the cell,

which will rearrange itself as E is increased, thus changing the resistance. An example of this is given in figure 5.20. This figure illustrates the leakage current with high voltage applied to only one side of the cell, and where the magnitude of the electric field was increased from 600 V/cm to 1.2 kV/cm to 1.8 kV/cm. The pattern of the electric field is as given in figure 5.1.

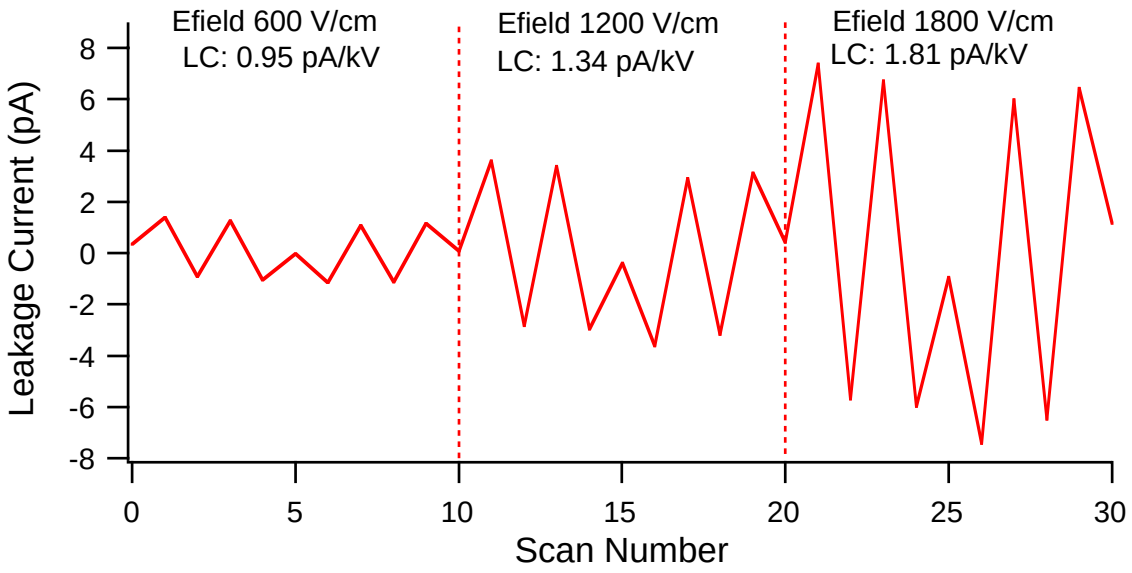

Figure 5.20: Keithley Leakage Current during a run with HV applied only to one side

5.3.2 Correlations and Corrections

Once the raw free-running frequencies are determined, they can be corrected. Section 4.3 covered some of the possible effects (besides an EDM) that could influence the measured frequencies. The best way to tell if any particular effect is causing a problem is to look for a correlation between the effect and the free-running maser frequencies. If the correlation is weak, the effect is probably unimportant. However if it is strong, this indicates where a problem lies. Ideally such a problem would be eliminated at the source. Failing that, however, the measured frequencies can still be corrected for the known variations in the systematics.

There are a number of possible methods to quantify the correlation between two

sets of numbers. Two have selected for the work here: the linear correlation and the Spearman Rank-Order correlation [65]. Each method determines a correlation coefficient from the data, and then determines the probability that such a coefficient is meaningful: i.e. that the correlation does not simply arise through random chance. The linear correlation coefficient is easy to determine, but the method is less reliable because the parent distribution of the measured quantities is unknown. The linear correlation coefficient for two sets of measurements x_i, y_i, is [4]

$$r = \frac{\sum(x_i - \overline{x})(y_i - \overline{y})}{\sqrt{\sum(x_i - \overline{x})^2}\sqrt{\sum(y_i - \overline{y})^2}} \tag{5.5}$$

The magnitude of r determines the strength of the correlation: zero indicates no correlation and one represents complete correlation. r can be positive or negative.

The Spearman Rank-Order coefficient is the more rigorous method because the parent distributions are determined. To accomplish this, every measurement x_i is replaced with its rank R_i among the others; the smallest measurement receives rank 1, the second smallest rank 2, up to the largest number which is rank N (for N values). The Spearman Rank-Order coefficient is determined from these ranks using equation 5.5, simply replacing $x_i \rightarrow R_i$ and $y_i \rightarrow S_i$ [65]. A new parameter t is then determined from r

$$t = r\sqrt{\frac{N-2}{1-r^2}} \tag{5.6}$$

t can take on any value, with $t = 0$ being no correlation and $|t| = \infty$ being complete correlation.

The size of the coefficients determine if the correlation is statistically meaningful. First consider the linear correlation coefficient. For a finite number of measurements N, the chance of obtaining a coefficient |r| through random chance is [4]

$$P(r, N) = \frac{1}{\sqrt{\pi}} \frac{\Gamma[\frac{N-1}{2}]}{\Gamma(\frac{N-2}{2})} \int_{|r|}^{1} (1 - x^2)^{\frac{N-4}{2}} dx \tag{5.7}$$

Since this chance exists for both positive and negative r, the chance that the correlation is meaningful is given by 1 - 2 P(r,N). The coefficient t for the Spearman Rank-Order test is approximately distributed as Student's distribution, F(t,N) [65]

[17]

$$F(t,N) = \frac{1}{B(\frac{N-2}{2}, \frac{1}{2})} \int_{-\infty}^{t} \left(1 + \frac{x^2}{N-2}\right)^{-\frac{N-1}{2}} dx \tag{5.8}$$

The probability that the measurement is not just the result of random chance can be expressed as the integral of this, properly normalized.

$$P(t,N) = 1 - F(-t,N)/F(0,N) \tag{5.9}$$

All of the experimental parameters recorded were checked to determine their correlation with the free-running maser frequency. Remember that the correlations were determined separately for each run. For jun1399. these include the locked maser frequency, the maser amplitudes, the temperatures of both oven chambers and the capacitor box, and the leakage current. Table 5.1 gives the correlation coefficients and corresponding confidence levels for jun1399.

Parameter	r	1- 2 P(r,N)	t	P(t,N)
Xe Freq	0.101	0.442	0.753	0.660
Xe Amp	-0.263	0.879	-0.755	0.661
He Amp	-0.465	0.996	-2.655	0.994
Pump Temp	-0.0692	0.312	-0.119	0.139
Maser Temp	0.102	0.446	0.524	0.512
Box Temp	-0.675	0.999994	-5.685	0.999999
Leakage Current	-0.135	0.568	-0.182	0.207

Table 5.1: Correlations with Free-Running Maser Frequency for jun1399

For both methods the correlation with the temperature of the capacitor box is definitive. This is due in part to cavity pulling (as discussed in Chapter Four) and partially from other room temperature effects, such as changing the field generated by the shields. The other parameters checked have weaker correlations with the measured frequency, though the maser amplitudes are still high. Correlations with the maser amplitude reflect changes in the longitudinal magnetization that affect T_2

Generally the correlations that are clear in the jun1399 run are typical of all the 125 runs. The correlation with maser amplitude was fairly common: these were at least 90% correlated in about half the runs. The temperature of the capacitor box

was also correlated to 90% about half the time. In runs where the room temperature, the output of the magnet lock-loop, and the laser beam powers were recorded, it was found that these also correlated with the helium maser frequency at least 90% about half the time. This is not too surprising, since the room temperature and the output of the PLL usually correlated with box temperature, and the laser beam powers tended to correlate with maser amplitude. Other parameters were less correlated: maser and pump correlations reach 90% in about a quarter of the runs. Finally the leakage current correlated to 90% in a fifth of the runs, and the xenon frequency correlated to 90% in only 10% of the runs. These last two parameters were not used in the correction procedure described below, since the xenon frequency is corrected for explicitly (see below) and the leakage current strongly correlates with the electric field.

For a few of the runs, the correlations between the free-running maser frequencies and the system parameters were checked within each scan, in addition to the checks over the entire run. This required breaking the scan into shorter (typically 100 second) regions, and then determining the values for each region. This was done for all the parameters in table 5.1.

Parameter	r	1- 2 P(r,N)	t	P(t,N)
Xe Freq	0.0452	0.150	-0.0191	0.0228
Xe Amp	-0.0549	0.182	0.384	0.392
He Amp	0.197	0.595	0.547	0.519
Pump Temp	-0.374	0.896	0.377	0.386
Maser Temp	0.102	0.331	-0.301	0.319
Box Temp	0.328	0.842	-0.241	0.262
Leakage Current	-0.0488	0.160	0.258	0.278

Table 5.2: Correlations with Free-Running Maser Frequency for scan 9 of jun1399

No significant correlations with the free-running maser frequency were found for this scan. Looking at the entire run, which contains 36 scans, there are 36 sets of 7 coefficients when the analysis is complete. These also showed no significant correlations.

Given that some parameters had strong correlations when the entire run was

considered, it is somewhat surprising that no strong correlations are seen on smaller timescales. No experiments have been performed to specifically investigate the issue. However I present here some educated guesses as to why this might be the case. It seems likely that there is no correlation with maser amplitudes because the amplitudes tend to oscillate slightly during a scan, in response to small perturbations. Only by averaging over a larger region can any correlated effect be seen. As for the capacitor box temperature, there may be a time delay involved, with the temperature of the capacitors lagging behind the temperature of the sensors. This would confuse the correlation on a 2000 second scale but allow it to be seen over the much longer run.

As mentioned above, some of the runs were also checked for a correlation between the free-running maser *phase* and the recorded parameters. Using the same 100 second regions for jun1399, one obtains

Parameter	r	1- 2 P(r,N)	t	P(t,N)
Xe Freq	0.101	0.328	-0.556	0.525
Xe Amp	-0.101	0.328	-0.873	0.710
He Amp	-0.129	0.412	-1.115	0.807
Pump Temp	-0.182	0.557	-1.186	0.830
Maser Temp	- 0.157	0.491	-1.353	0.874
Box Temp	0.155	0.486	0.718	0.628
Leakage Current	-0.322	0.834	-0.547	0.519

Table 5.3: Correlations with Free-Running Maser Frequency for a scan 9 of jun1399

In this case, the correlations are slightly stronger. The phase in this particular scan did not show obvious correlations with the maser amplitudes, though other scans generally did.

Now that the correlations have been determined, the next step is the corrections. The first correction is for the locked maser frequency. Although nominally locked at exactly 25 mHz, drifts in reference frequency, the lock-loop parameters or the signal size may cause it to vary by 10's of nHz over the course of a run. For xenon locking, the frequency of the free-running helium is corrected for this by adding in $\frac{\gamma_{He}}{\gamma_{Xe}}(\text{xefreq} - .025)$. This is a very small effect.

The next step in the corrections is to remove drift. These drifts arise from systematics that were not specifically checked for above, and so can not be accounted for through a correlated parameter. However, since the drifts are due to long term instabilities and not the alternating E field, it is safe to remove them using a polynomial (of order much less than the number of scans). Each run is therefore fit to a cubic function (of the scan number), which generally works well to remove such drifts.

After the cubic fit subtraction, the changes in correlated parameters must be accounted for. Those parameters whose correlation probability passes a certain threshold are tested to see if correcting for the parameter improves the measurement. In many cases the previous step of fitting to a cubic obviates the need for such a correction. For example, if the correlated parameter drifts linearly with time, then the cubic fit will already have removed it. To see if including the correlated parameter is still necessary, the so-called F-test is employed. The F-test determines if adding the correlation to the fit makes a statistically significant improvement. A coefficient F is determined based on how much a fit to the data improved when a new parameter is added. This coefficient, for a certain number of degrees of freedom, sets the probability that the change actually improved the fit.

There is no *a priori* method for determining what the threshold for testing a correlation should be, nor for deciding what probability is sufficient to pass the F-test. Therefore the data taken was analyzed in three separate ways. Method One set high thresholds, applying the F-test only to parameters that reached at least 98% probability of meaningful correlation for both tests. This same 98% probability was used to see if the correlated parameter passed the F-test. Method Two had a threshold of 90%, again for both probabilities. Method Three was the least stringent, requiring a minimum of 70% probability for acceptance.

The procedure for determining F is outlined below. The first step is to note the χ^2 for the cubic fit to the data. Then the frequencies of the free-running species are fit to a new function that combines a cubic polynomial and the correlated parameter. For instance, the example run, jun1399, was fit to the function

$$\mathrm{func} = \mathrm{a} + \mathrm{b\,x} + \mathrm{c\,x^2} + \mathrm{d\,x^3} + \mathrm{e\,boxtemp(x)} \tag{5.10}$$

From the χ^2 for the new fit it is possible to obtain F_χ. The size of F_χ determines if the addition of a new term in the fit genuinely improved it.

$$F_\chi \;\; = \frac{\delta\chi^2}{\chi^2_f} \;\; = \frac{\chi^2(\mathrm{p}) - \chi^2(\mathrm{p+n})}{\frac{\chi^2(\mathrm{p+n})}{(\mathrm{N-p-n})}} \tag{5.11}$$

where $\chi^2(\mathrm{p})$ is for the fit to the original model of p=4 parameters and n=1 is the number of parameters added. The distribution of F can be found from tabulated values [4].

This process is repeated for all parameters that were sufficiently correlated to be tested for that Method. The parameter that passes with the highest F is added to the fit function. The process is then repeated for the remaining parameters, until no more parameters pass the F-test at the level set by that Method. When proceeding to a new Method, the procedure is begun again.

It is of some concern that the parameters corrected for do not correlate with the electric field, which would bias the EDM value obtained. Fortunately such correlations were very rare and could be attributed to random chance. If a parameter is correlated with E^2, then correcting for it will alter the coefficient that looks for variation of the EDM with E^2, as described below. Correlations with E^2 were more common than correlations with E, but even so only 20% of the data runs corrected for a parameter that correlated with E^2 at 70% or higher probability, and only 8% corrected for a parameter that correlated with E^2 at 90% or more. Therefore it is safe to assume that no significant biasing occurred.

Let me emphasize that it is the F-test that determines if a parameter is added to the fit of the maser frequency. The measurement of correlations only determines which parameters are checked. This selection is important in order to greatly reduce the time needed to confirm the optimum fit. If every combination of the (up to) nine parameters available for correction in each run was checked, for each of the three Methods, the analysis time would be increased by a factor of four or more.

For the jun1399 run, adding the capacitor box temperature to the fit yielded an F_χ of 7.466. This means that it is 99.0% probable that the fit genuinely improved. (The helium amplitude generated an F that was lower than this.) Then the amplitude of the helium maser was added as a second parameter. In this case the new F_χ was 3.114, so it is 91.2% likely that the fit really improved. As can be seen in table 5.1

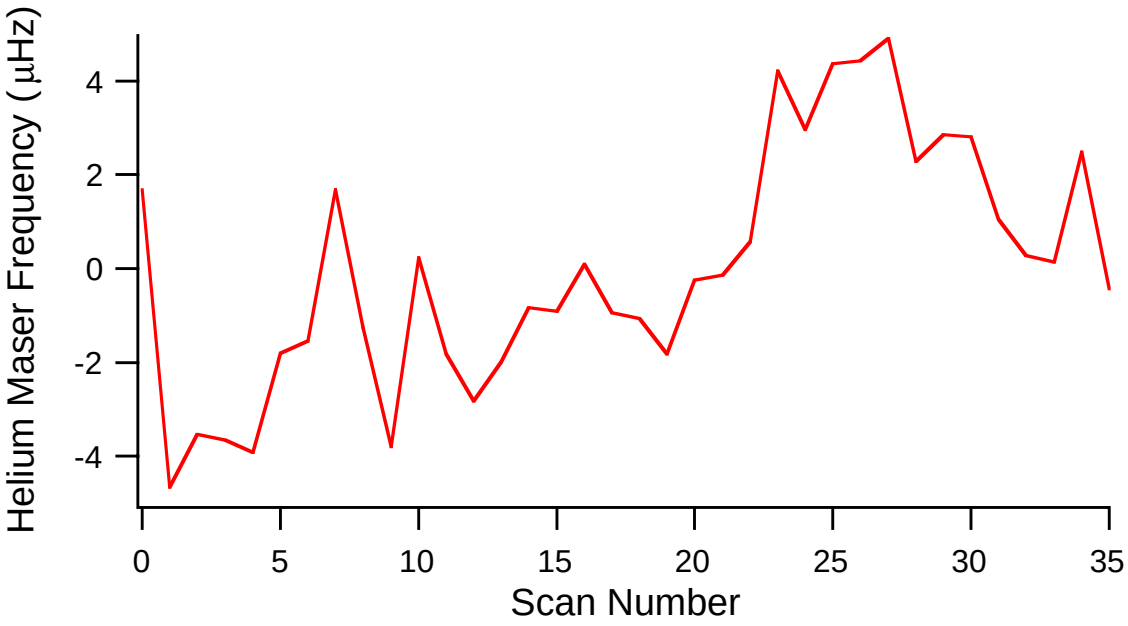

Figure 5.21: Free-Running Maser Frequencies, corrected for xenon drifts and with mean set to zero

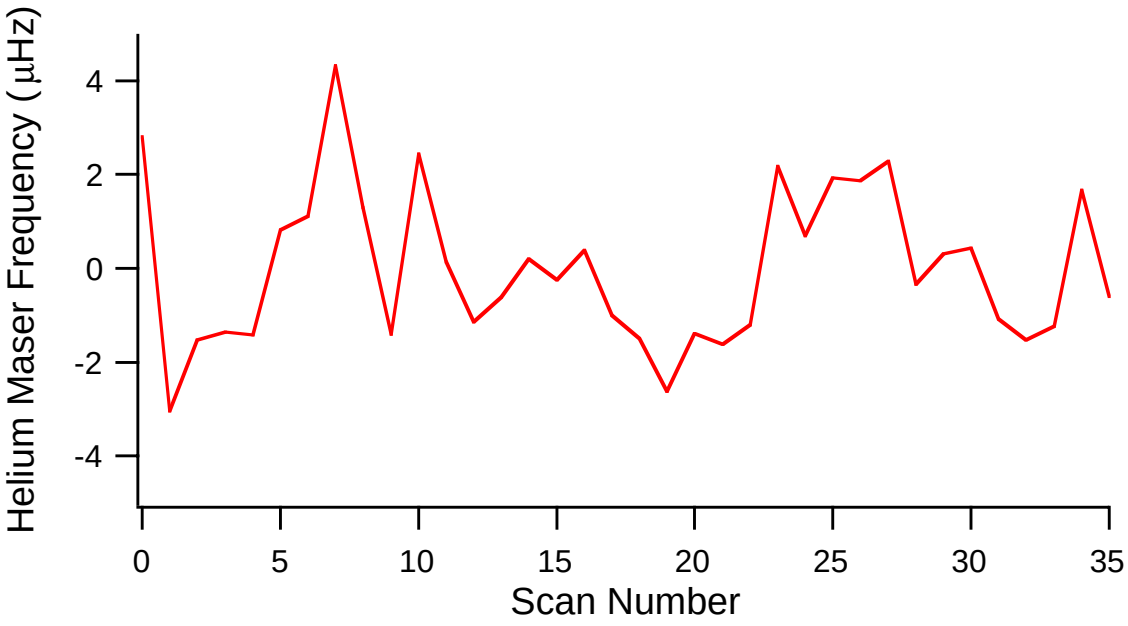

Figure 5.22: Free-Running Maser Frequencies after cubic fit subtraction

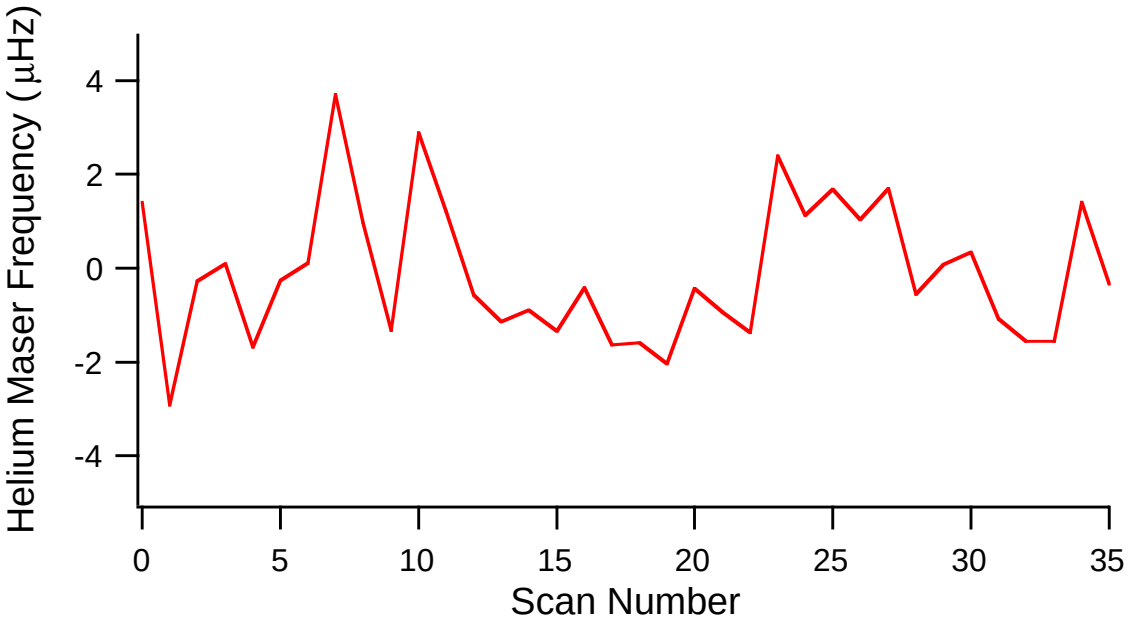

Figure 5.23: Free-Running Maser Frequencies after cubic fit subtraction and boxt correlation removal

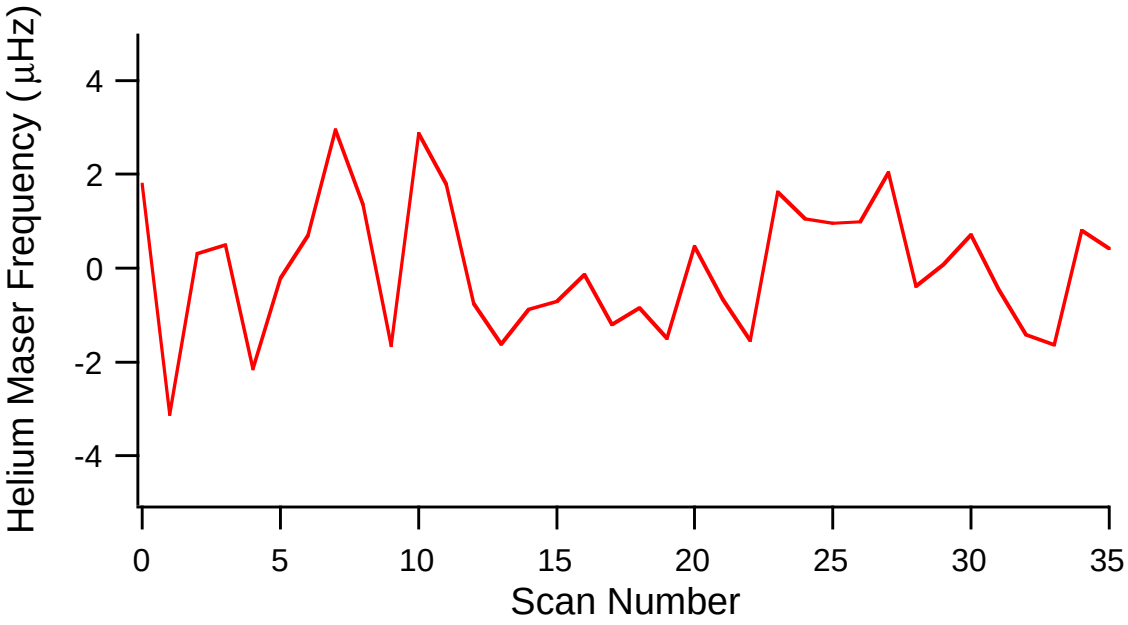

Figure 5.24: Free-Running Maser Frequencies after cubic fit subtraction and boxt and heamp correlation removal.

these are the only two parameters that have correlations greater than 70% for both types of correlation calculation, so no other parameters need to be checked. Method One corrects for only the box temperature. Method Two and Method Three give identical results for this run: both correct for the capacitor box temperature and helium amplitude.

As the last stage of the corrections, the run is checked for bad points to remove. Such bad points result from sudden perturbations that the system managed to recover from. Two separate checks are made. The first one looks for an abrupt change in the corrected free-running maser frequency, $\delta\nu$. If this change is large enough that

$$\delta\nu \geq 3\sqrt{2}\,\sigma \tag{5.12}$$

where σ is the standard deviation of the frequency points, then the difference is considered too large to be acceptable [43]. No strings or point-to-point differences that include this difference will be included in determining the result (see the next section). The second check searches for points that are far from the mean of the values. The standard procedure here is to discard a point if one expects less than half an event to be further from the mean than the suspect point. This is Chauvenet's criterion [4], and it is tested mathematically as

$$\mathrm{erf}\left(\frac{\nu}{\sqrt{2}\,\sigma}\right) \geq 1 - \frac{0.5}{\mathrm{N}} \tag{5.13}$$

for each of the N frequencies ν of the run. If the above test condition is met then the data point will not be used in any of the analysis methods given below. The example run, jun1399, had one bad point for Method One but no bad points for Methods Two and Three. In all the runs taken, about half had a single bad point, and five percent had more than one. This elimination of bad points was the only way a data scan would be discounted in a run; runs were never cut short due to laser or temperature fluctuations, for example.

Before extracting the EDM value, the corrected frequencies are plotted versus the electric field and fit to a quadratic. The linear term is one measure of the EDM value, but the principal reason for the fit is learning the quadratic coefficient. This is a measure of any systematic frequency shifts caused by the magnitude of E (or E^2).

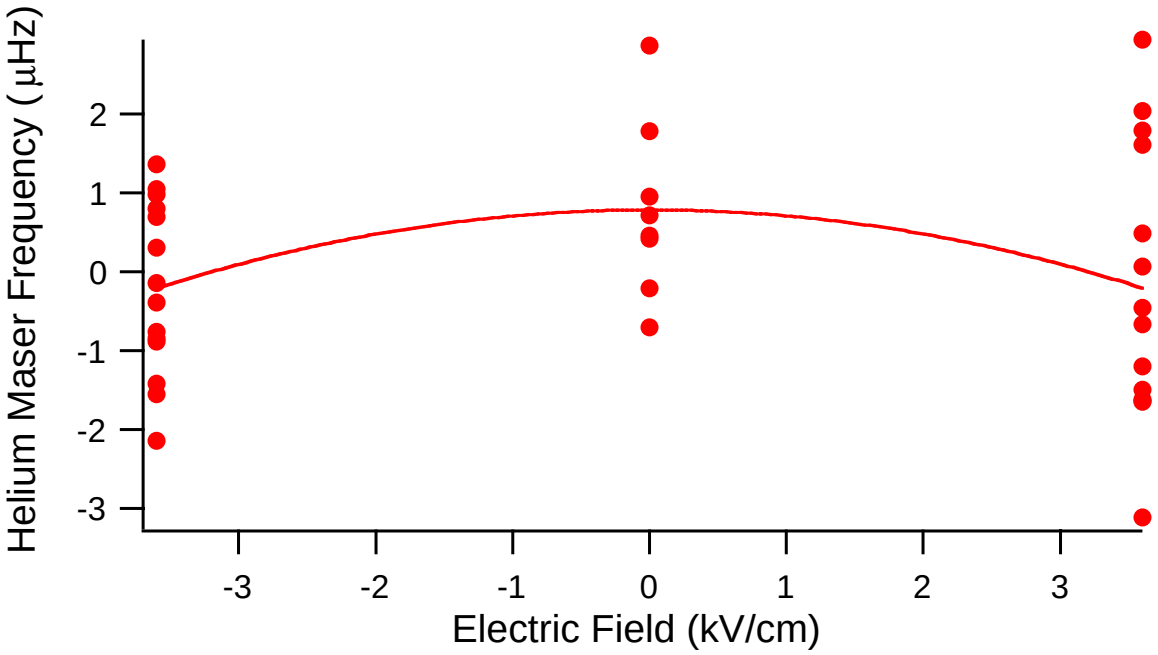

Figure 5.25: Free-Running Maser Frequencies, corrected as per Method Two, for Plus, Minus, and Zero Scans during a run, with quadratic fit

The quadratic coefficient for June 13, 1999 was (-7.116 +- 4.177) $\times 10^{-8}$ Hz/(kV/cm)^2 for Method One. It is (-7.657 +- 4.338) $\times 10^{-8}$ for Methods Two and Three.

5.3.3 EDM Extraction

Finally everything is ready to determine the EDM value for the run. As explained in section 2.1, the needed parameter is the change in frequency when the electric field is reversed with respect to the magnetic field. The most straightforward method to do this (the "zeroth order" method) is to determine the mean and standard deviation of the mean separately for the scans with E parallel to B (the left-hand side of figure 5.25) and those with E antiparallel to B (the right-hand side of figure 5.25). The two means are subtracted to obtain the EDM for the run, and the standard deviations of the mean are added in quadrature to give the uncertainty.

$$\begin{aligned} \delta\nu &= \nu_{anti} - \nu_{para} \\ \sigma_{mean} &= \sqrt{(\sigma_{mean}^{anti})^2 + (\sigma_{mean}^{para})^2} \end{aligned} \tag{5.14}$$

At a minimum, five scans of both E field orientations must be taken for the run to be considered valid. This is based on the need for enough points to have a reliable estimate of the standard deviation. The rule was stretched a little for the scans with no field: if there were at least four scans assigned to each orientation of the electric field (at least eight no field scans all told), then the zero field scans are also analyzed to determine their EDM limit. (Each such scan is assigned the E field value of the two points around it) This gives us a systematic check of the measurement.

The second method of determining the xenon EDM is to calculate the difference in frequency between two (or several) successive scans, and find the mean and variance of these. Using the point-to-point differences gives the Allan Variance that was described in Chapter Four. A linear combination of more than two points, referred to as a string, may also be used. The advantage of these methods is that they reduce the effect of drifts on a timescale short compared to the length of the run [43]. In creating these kinds of frequency difference most of the data points are used more than once. This means that the series of differences is no longer linearly independent, and so the final uncertainty must be multiplied by the appropriate factor. Furthermore, in order to use all of the data, the scans with no electric field are included in the series. To obtain a valid EDM result, the weight of each difference must be included, so that a change from no field to 3.6 kV/cm is less important than a change from 3.6 kV/cm to -3.6 kV/cm.

The derivation of the differences and their weighting factors is as follows. For the Allan Variance case, the frequency points are

$$\begin{aligned} \nu_i &= &= +2\,\alpha_i\,\mathrm{d}^{\mathrm{j}}_{\mathrm{Xe}}\,|\mathrm{E}| \\ \nu_{i+1} &= &= -2\,\alpha_{i+1}\,\mathrm{d}^{\mathrm{j}}_{\mathrm{Xe}}\,|\mathrm{E}| \end{aligned} \tag{5.15}$$

where $\alpha_i = 1$ if the high voltage is on and $\alpha_i = 0$ if it is off. Note that the fits described in the previous section have already set the mean of the frequencies to be zero. Solving for $\mathrm{d}^{\mathrm{j}}_{\mathrm{Xe}}$ gives

$$4\,\mathrm{d}^{\mathrm{j}}_{\mathrm{Xe}}\,|\mathrm{E}| = 2\,\frac{(\nu_{\mathrm{i}} - \nu_{\mathrm{i+1}})}{\alpha_{\mathrm{i}} + \alpha_{\mathrm{i+1}}} \tag{5.16}$$

The error for point j is

$$\sigma_j \;= \frac{\sqrt{\sigma_i^2+\sigma_{i+1}^2}}{\alpha_i+\alpha_{i+1}} \;= \frac{\sqrt{2\,\sigma_i}}{\alpha_i + \alpha_{i+1}} \tag{5.17}$$

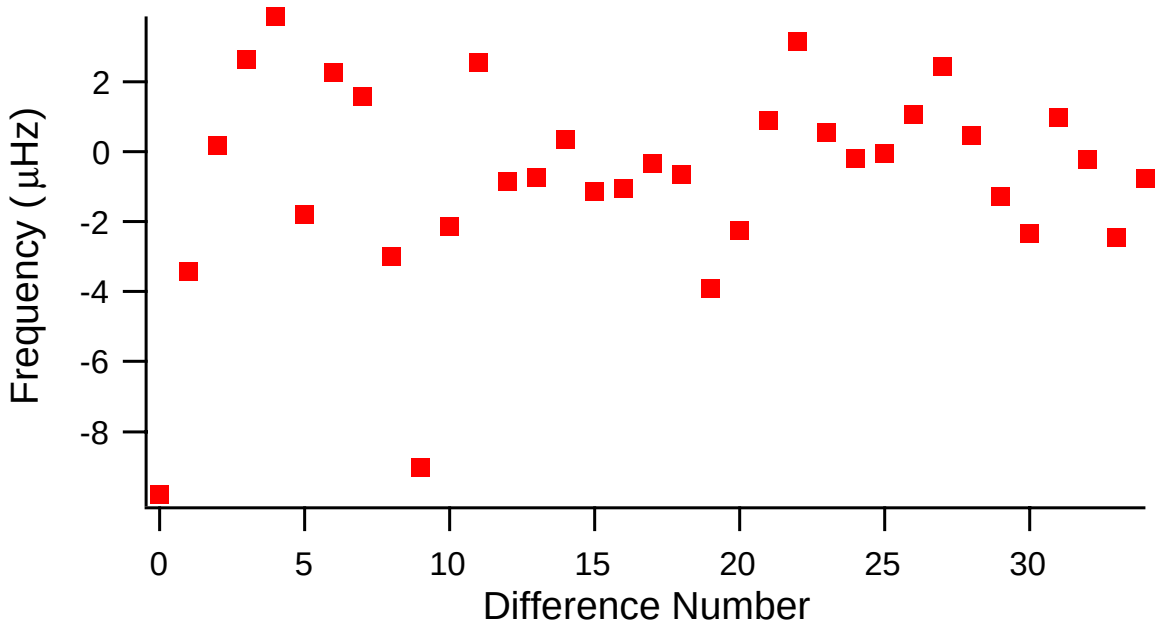

Figure 5.26: Point-to-Point frequency differences for a run

since by my earlier assumption all the σ_i's are equal to σ. The correction factor for overcounting is just the inverse of the average of the errors

$$\text{Correction} = \frac{1}{\overline{\sigma_{\mathrm{j}}}} \tag{5.18}$$

Note that if there were no scans at zero electric field (i.e. all the differences had equal weight), this correction would reduce to $\sqrt{2}$.

Exactly the same steps apply to the string variance, although the solution looks a bit more complicated. In the string analysis, it is assumed that the frequency points include linear and quadratic drifts in addition to the EDM shifts

$$\begin{aligned}
\nu_i &= +2\,\alpha_i\,\mathrm{d}^{\mathrm{j}}_{\mathrm{Xe}}\,|\mathrm{E}| \\
\nu_{i+1} &= -2\,\alpha_{i+1}\,\mathrm{d}^{\mathrm{j}}_{\mathrm{Xe}}\,|\mathrm{E}| + \Delta + \Delta^2 \\
\nu_{i+2} &= 2\,\alpha_{i+2}\,\mathrm{d}^{\mathrm{j}}_{\mathrm{Xe}}\,|\mathrm{E}| + 2\Delta + 4\Delta^2 \\
\nu_{i+3} &= -2\,\alpha_{i+3}\,\mathrm{d}^{\mathrm{j}}_{\mathrm{Xe}}\,|\mathrm{E}| + 3\Delta + 9\Delta^2
\end{aligned} \tag{5.19}$$

Solving for $\mathrm{d}^{\mathrm{j}}_{\mathrm{Xe}}$ gives

$$4\,\mathrm{d}^{\mathrm{j}}_{\mathrm{Xe}}\,|\mathrm{E}| = 2\,\frac{(\nu_{\mathrm{i}} - 3\,\nu_{\mathrm{i+1}} + 3\,\nu_{\mathrm{i+2}} - \nu_{\mathrm{i+3}})}{\alpha_{\mathrm{i}} + 3\,\alpha_{\mathrm{i+1}} + 3\,\alpha_{\mathrm{i+2}} + \alpha_{\mathrm{i+3}}} \tag{5.20}$$

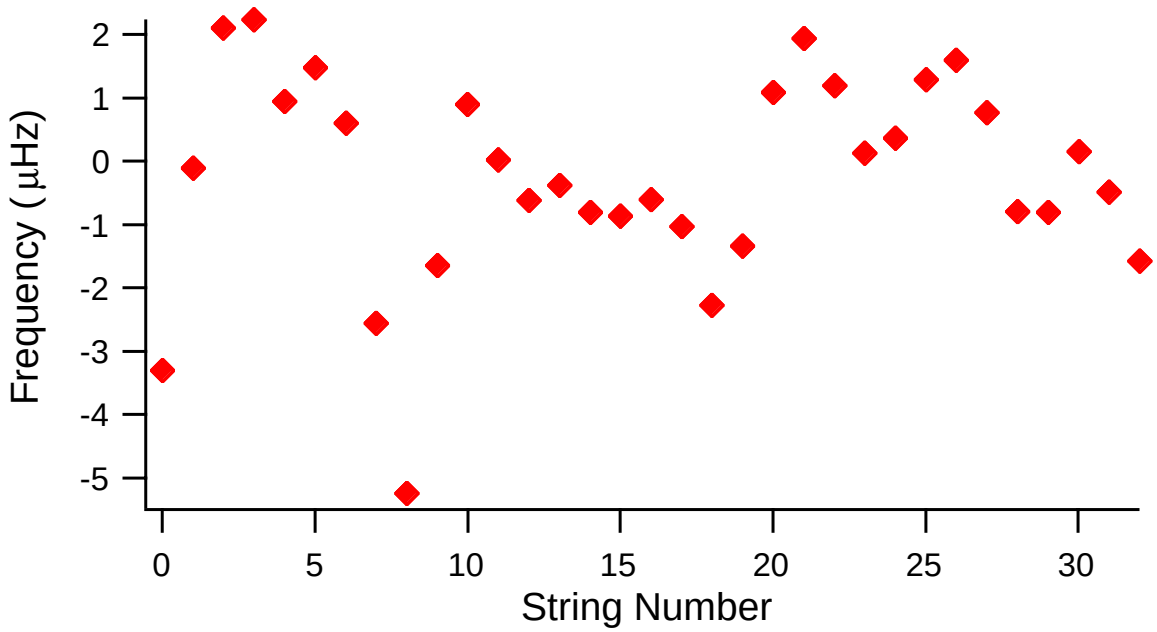

Figure 5.27: String frequency differences for a run

The error for point j is

$$\sigma_j = \frac{\sqrt{20}}{\alpha_i + 3\alpha_{i+1} + 3\alpha_{i+2} + \alpha_{i+3}}\sigma_i \tag{5.21}$$

and the final correction factor is again

$$\text{Correction} = \frac{1}{\overline{\sigma_j}} \tag{5.22}$$

If there were no scans with zero electric field, this would reduce to a correction factor of $\frac{8}{\sqrt{20}}$ to the uncertainty.

Once these values are obtained, the reported frequency splitting for the run is just the weighted average of the differences. A weighted average is calculated as [4]

$$\mathrm{d_{run}} = \frac{\sum \frac{\mathrm{d_j}}{\sigma_j^2}}{\sum \frac{1}{\sigma_j^2}} \tag{5.23}$$

with an error (including the correction factor) of

$$\sigma_{run} = \frac{\overline{\sigma_j}}{\sum \frac{1}{\sigma_j^2}} \tag{5.24}$$

All of the above methods actually measure the frequency splitting corresponding to the energy difference when the electric field is reversed, $\delta\nu_{Xe} = 4\ \mathrm{d_{Xe}}\,|\mathrm{E}|$ (refer to figure 2.1). To obtain a value for $\mathrm{d_{Xe}}$ requires some basic algebra

$$\mathrm{d_{Xe}} = -\frac{\mathrm{h}\,\delta\nu_{\mathrm{Xe}}}{4\,\mathrm{E}} = -1.034 \times 10^{-18}\,\frac{\delta\nu_{\mathrm{Xe}}}{\mathrm{E}} \tag{5.25}$$

where the electric field E is given in kilovolts/cm. However, as described in section 4.1, the helium is actually the free-running species. Therefore the helium frequency is divided by the ratio of the gyromagnetic moments (2.75408) to obtain the equivalent frequency for xenon, and the sign is flipped.

$$\mathrm{d_{Xe}} = \frac{\mathrm{h}\,\delta\nu_{\mathrm{He}}}{(2.75408)\,(4\,\mathrm{E})} = 3.754 \times 10^{-19}\,\frac{\delta\nu_{\mathrm{He}}}{\mathrm{E}} \tag{5.26}$$

The uncertainty in the xenon EDM is obtained using the same equation, since the fractional uncertainty of the electric field is negligible in comparison to the fractional uncertainty in the frequency.

Table 5.4 lists the EDM determined by the three methods described above for jun1399.

Method One	EDM Value	Error
Zeroth Order	2.287×10^{-26}	5.433×10^{-26}
Point-to-Point	2.078×10^{-26}	3.908×10^{-26}
String	5.537×10^{-27}	4.070×10^{-26}

Methods Two and Three	EDM Value	Error
Zeroth Order	-4.643×10^{-28}	5.823×10^{-26}
Point-to-Point	6.893×10^{-27}	4.127×10^{-26}
String	6.807×10^{-27}	3.908×10^{-26}

Table 5.4: $\mathrm{d_{Xe}}$ for jun1399 for each analysis method

All the methods give consistent results. The methods that rely on differences have lower errors, since they are less sensitive to short-term frequency drift. Of these two, I favor using the string variance, since it should do the best job of reducing the sensitivity to drifts. Therefore, all the EDM values reported below are for the string variance analysis method.

5.4 Systematic checks

This section describes several kinds of systematic checks that were made. First of all, certain runs were taken with fabricated data, beating two sets of frequency synthesizers against one another as for the clock runs described in Chapter Four. Insofar as possible, the system was the same as it was for actual running conditions. The only change was that the signal into the SR850's was from a frequency synthesizer, rather than from the pre-amps. This check helps to find mistakes in the analysis routine, or spurious effects such as the high voltage supplies broadcasting noise to the lockins, frequency generators, etc. The analysis proceeded in the same manner as for real EDM data, but no correlations were used (or found). The errors for each run are about what one would expect from the Allan Variance plot of the frequency generators (see figure 4.3)

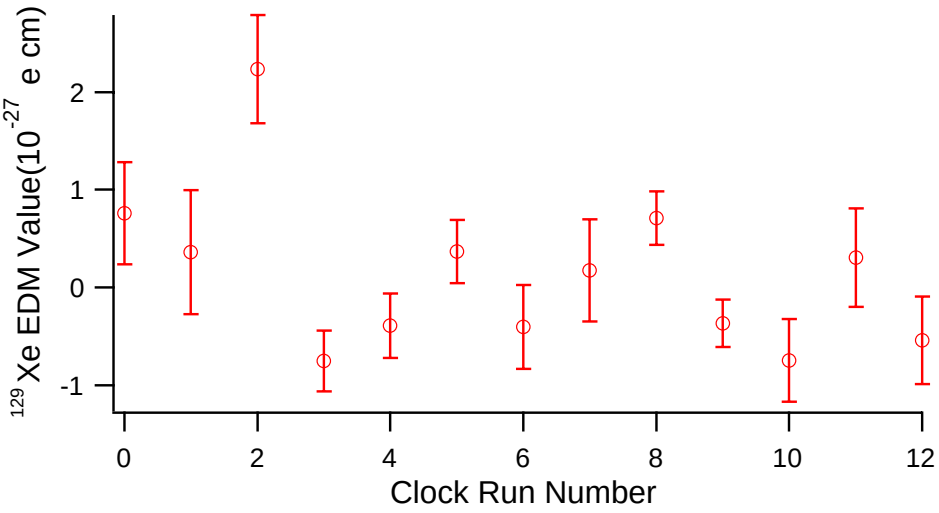

Figure 5.28: "EDM" results with simulated data

The result from these simulated runs is $(-0.1067 + -1.039) \times 10^{-28}$, with a χ^2_ν of 3.51. This indicates that the high voltage supplies and associated electronics are not biasing the result.

The second check determines the coefficient of the helium frequency vs E^2. This could arise due to changes in the diamagnetic shielding (see section 4.2.1) or changes in the magnetic field due to the magnitude of E (presumably from changes in shielding). The values listed are in terms of frequency, rather than the equivalent EDM

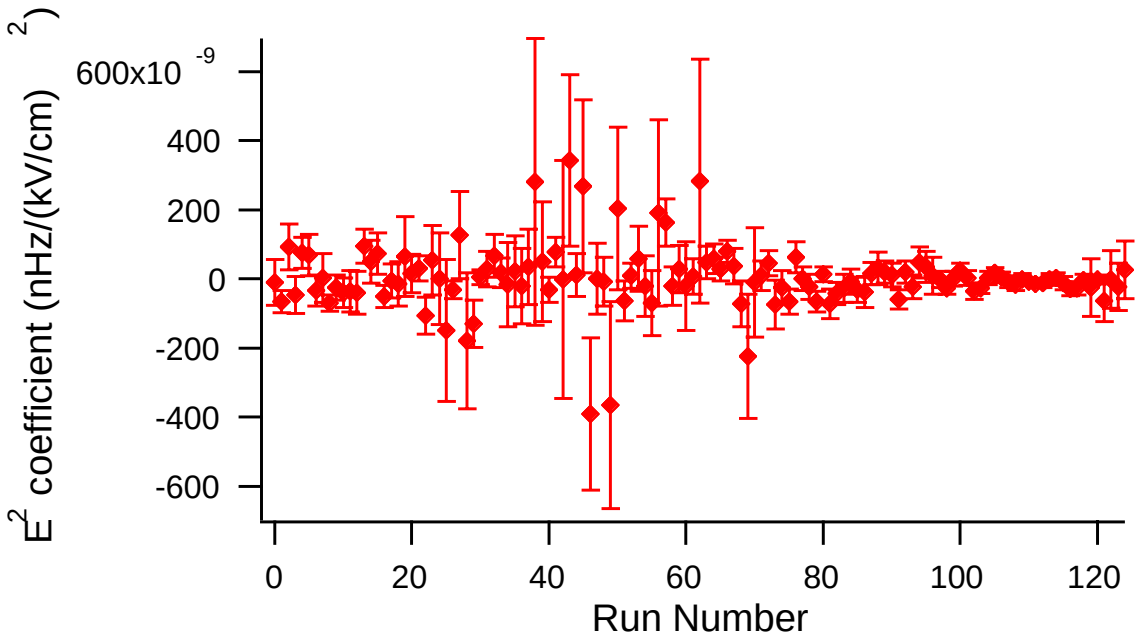

Figure 5.29: Coefficient of measured frequencies vs E^2 for Method Two Analysis

value, for convenience in making corrections.

Method	E^2 Coef	E^2 Coef Error	χ^2_ν
Method One	-8.565×10^{-09}	2.900×10^{-09}	0.950
Method Two	-6.731×10^{-09}	2.787×10^{-09}	0.992
Method Three	-7.009×10^{-09}	2.697×10^{-09}	1.017

Table 5.5: Weighted Averages of He Freq vs E^2 for each analysis method

Bench tests have directly measured that the electric field was switched to within 1 V/cm. Therefore the difference in frequency between the E parallel to B vs E antiparallel to B is fHz and can be ignored. However, the difference between the HV on and HV off can be a concern. The negative coefficient means that the scans with the HV off are effectively at higher frequency than they should be. This effect does not impact the Zero-Order analysis, which does not use these scans at all. However, it does lead to a small correction to the Allan Variance and String Variance Methods for some of the runs. The size of this correction depends on the E field pattern for the run, and existence of any bad points. For runs with no bad points, the systematic

will cancel out if the run begins and ends with HV off scans, and there are an even number of the HV off scans. For runs where this was not the case, a correction of up to a few percent was made to the result.

The third form of check was the switching of the magnetic field with respect to the laboratory coordinate frame. This should reveal if the electric field interacts with the shields or some other part of the system and produces a consistent bias. The EDM data, broken down into West and East regions, are presented in tables 5.6, 5.7.

Method	EDM Value	Error	χ^2_ν
Method One	1.735×10^{-26}	5.693×10^{-27}	1.470
Method Two	1.981×10^{-26}	5.685×10^{-27}	1.317
Method Three	1.946×10^{-26}	5.561×10^{-27}	1.371

Table 5.6: Measured EDM values for magnetic field pointing West

Method	EDM Value	Error	χ^2_ν
Method One	-7.528×10^{-27}	3.368×10^{-27}	1.010
Method Two	-5.678×10^{-27}	3.281×10^{-27}	1.157
Method Three	-2.830×10^{-27}	3.242×10^{-27}	1.111

Table 5.7: Measured EDM values for magnetic field pointing East

These values are clearly different, by about four sigma. Even if the errors are corrected for χ^2_ν, it is still more than 99% likely that the difference is not statistical fluctuation. By analyzing smaller regions of the data (one month, for example) it was shown that the discrepancy is not due to a single aberrant section. Therefore, the data obtained in this measurement do not follow the expected pattern for an EDM (proportional to $\mathrm{E} \cdot \mathrm{B}$). The exact mechanism causing this systematic effect is unclear. Note that the shift due to E^2 presented above was the same for both magnetic field orientations; therefore the difference between East and West is not proportional the *magnitude* of E. Further insights into the source of the effect follow in this section and in Chapter Six.

The fourth check was of the E=0 scans taken in the data. This check will reveal if there is an offset in the E field values, if frequency depends on the HV relay position,

or if the direction of the electric field somehow biases the results. For example, the current that flows through the HV circuit while the electric field is changed could change the residual field generated by the magnetic shielding. The data can also be analyzed separately for the East and West directions, to explore if the systematic seen above had any effect even when there was no electric field.

There were 41 runs that had sufficient data for an EDM measurement of these scans. These 41 scans were supplemented by 8 additional runs which had more frequent E=0 data, in order to improve the statistics of the values obtained. The example run, jun1399, had an E=0 EDM value of $(10.868 + -9.342) \times 10^{-26}$ for Method One, and $(13.073 + -6.433) \times 10^{-26}$ for Methods Two and Three. The weighted average of all the runs, for each Method, is presented in table 5.8.

Method	No Field EDM	Error	χ^2_ν
Method One	6.505×10^{-27}	8.549×10^{-27}	1.573
Method Two	-9.434×10^{-28}	7.980×10^{-27}	1.781
Method Three	-5.352×10^{27}	7.485×10^{-27}	1.714

Table 5.8: Weighted Averages of No Field run results for each analysis method

Analyzed for the two different magnetic field directions (as the EDM data was above) the result for each Method is given in table 5.9.

When the data are broken into East and West sections, there is again evidence of a discrepancy, though of course the statistics are not as good. Note that the signs are different than in the actual EDM data: this suggests that the systematic effect does not correlate with the high voltage relay position but instead with the *change* of E preceeding the scan. The effect clearly cancels out when results for the two directions are combined in a weighted average.

5.5 Result and Discussion

Table 5.13 at the end of the chapter gives some basic information for each of the data runs taken. N is the number of scans used, $\vec{B}$ indicates the direction of the magnetic field, and HV refers to the magnitude of the applied electric field. The value for HV has been corrected for the exact cell length of 1.979 cm and for small

Method One	No Field EDM	Error	χ^2_ν
West	-2.894×10^{-26}	1.750×10^{-26}	1.584
East	1.762×10^{-26}	9.788×10^{-27}	1.396

Method Two	No Field EDM	Error	χ^2_ν
West	-1.549×10^{-26}	1.585×10^{-26}	1.519
East	4.000×10^{-27}	9.237×10^{-27}	2.083

Method Three	No Field EDM	Error	χ^2_ν
West	-1.570×10^{-26}	1.565×10^{-26}	1.488
East	-2.283×10^{-27}	8.523×10^{-27}	1.987

Table 5.9: Weighted Averages of No Field run results for each Method

offsets in the HV supply program voltages. The table also lists the d_{Xe} obtained using the Method Two string analysis.

All of the values in table 5.13 have been corrected for the slight dependence of the frequency on E^2, but not for the much larger systematic that shows up when comparing the "East" runs to the "West" runs. Since the East and West runs are measuring different quantities, they can not be combined in a weighted average. To combine them into one measurement would require assumptions about how the systematic varies with orientation. If it is assumed that the systematic is the same for both directions, then the (unweighted) average of East and West could be used as the final result.

It is quite possible that the systematic frequency shift is not constant. It may depend on the magnetic field orientation, or the tuning of the gradients and resonators, or it may simply drift with time. The first possibility is supported at some level by the no field results, presented in table 5.9, where the systematic effect may have a different magnitude (as well as a different sign) for the two magnetic field directions. The tuning of the gradients and resonators is suspect because such tuning is performed each time the magnetic field is reversed. Therefore if the systematic were dependant on the tuning, it would likely cause a difference between the East and West results.

To study the possibility that it is the tuning that matters, rather than the magnetic field direction, the data are broken down into five regions. Each region is for one particular tune-up of the system, and so the regions make up subsets of the two magnetic field directions. The Method Two weighted averages for each region are presented in table 5.10. Note that West3 consists of only four data runs, and thus has

Region	EDM Value	Error	χ^2_ν
West1	2.368 $\times 10^{-26}$	1.026 $\times 10^{-26}$	1.118
East1	1.910 $\times 10^{-27}$	9.080 $\times 10^{-27}$	1.134
West2	2.024 $\times 10^{-26}$	6.999 $\times 10^{-27}$	1.429
East2	-6.818 $\times 10^{-27}$	3.519 $\times 10^{-27}$	1.209
West3	-2.507 $\times 10^{-26}$	3.136 $\times 10^{-26}$	1.678

Table 5.10: Method Two EDM Values for Different Tune-Up Regions

a large statistical error. The other two West runs are quite consistent, and the two East runs are also consistent. Thus the magnetic field direction may be the crucial parameter after all. Alternately, the statistics of these data may not be sufficient to resolve what is actually occurring.

The scans with no electric field can be broken down for these same regions, as presented in table 5.11. There is only a small amount of no field data in the first

Region	EDM Value	Error	χ^2_ν
West1	-4.040 $\times 10^{-26}$	1.084 $\times 10^{-25}$	0.775
East1	-9.040 $\times 10^{-26}$	4.604 $\times 10^{-26}$	1.630
West2	-2.091 $\times 10^{-26}$	1.800 $\times 10^{-26}$	1.513
East2	7.759 $\times 10^{-27}$	9.429 $\times 10^{-27}$	2.268
West3	7.717 $\times 10^{-27}$	3.510 $\times 10^{-26}$	1.882

Table 5.11: Method Two No Field Values for Different Tune-Up Regions

region, so the error there is quite large, and the statistics are not very good for the other regions either. However, it does appear that the results for the five different regions are not very consistent. It is not possible to say conclusively that there is a systematic that changes each time the system is retuned, but it remains a possibility that requires further exploration.

In summary then, the experiment performed thus far is almost certainly being affected by a systematic. What this systematic is or how it changes with time are unknown. It is possible that the systematic is a static quantity, and that the measurement of it simply needs better statistics. In this case the results of the East and West data (from table 5.6) could be averaged to obtain an EDM value. Since this is one possible outcome of the measurement, the averages are presented in table 5.12

Method	EDM Value	Error
Method One	4.911×10^{-27}	3.307×10^{-27}
Method Two	7.066×10^{-27}	3.282×10^{-27}
Method Three	8.315×10^{-27}	3.219×10^{-27}

Table 5.12: EDM values obtained by averaging East and West

If the systematic truly does change each time the system is retuned (or even more often), then I am simply unable to state the size of the systematic, and so the East and West directions, or their subsections, can not be combined, and no reliable EDM value is obtainable.

It is clear that more work needs to be done to extract a reliable value of the xenon EDM from this measurement. Chapter Six outlines some approaches to determine what is causing the systematic, which would determine the proper way to correct for it. I note that even though the systematics are not understood, I have demonstrated an impressive statistical precision for the maser system. This precision is set by the weighted average of all the data runs. Using the Method Two data gives a weighted average of

$$\mathrm{d_{Xe}} = (0.689 + -2.842) \times 10^{-27}\,\mathrm{e\,cm} \tag{5.27}$$

If the systematic discussed above could be eliminated, a result of this quality would be easily attainable.

Regardless of exactly how the systematic is affecting the measurement, the experimental value of the xenon-129 EDM is still much larger than the expected value of about 2 $\times 10^{-28}$ e cm or smaller. It is clear that this measurement still falls short of its goal to improve the limits on the parameters of elementary particle theory. Prospects for improving the present experiment are discussed in the next chapter.

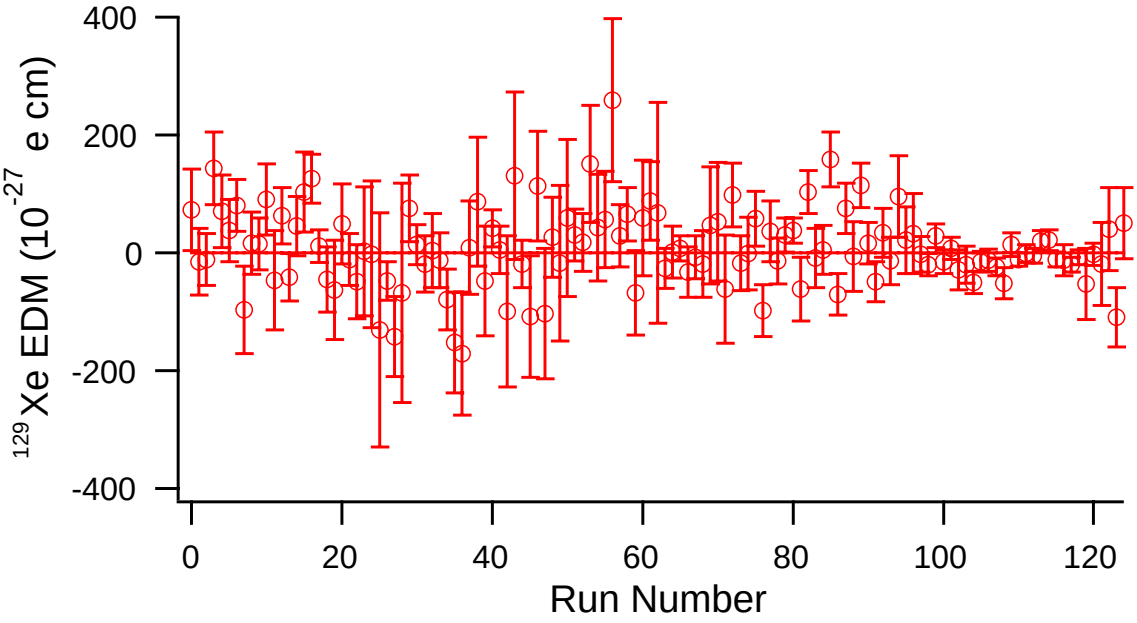

Figure 5.30: EDM's for each run (Method One String Analysis)

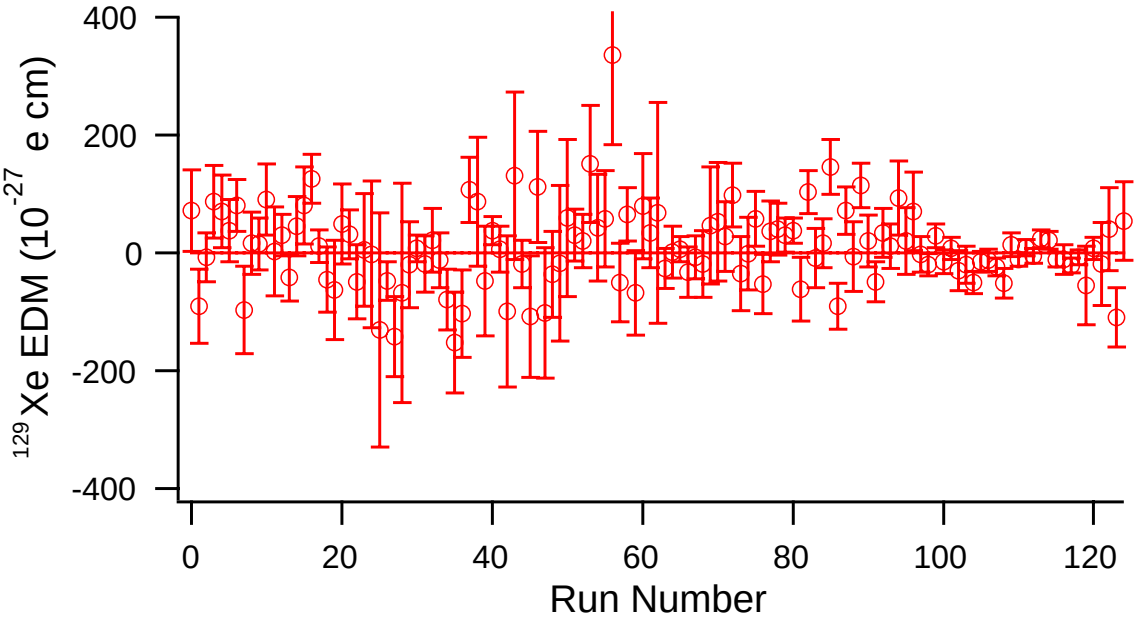

Figure 5.31: EDM's for each run (Method Two String Analysis)

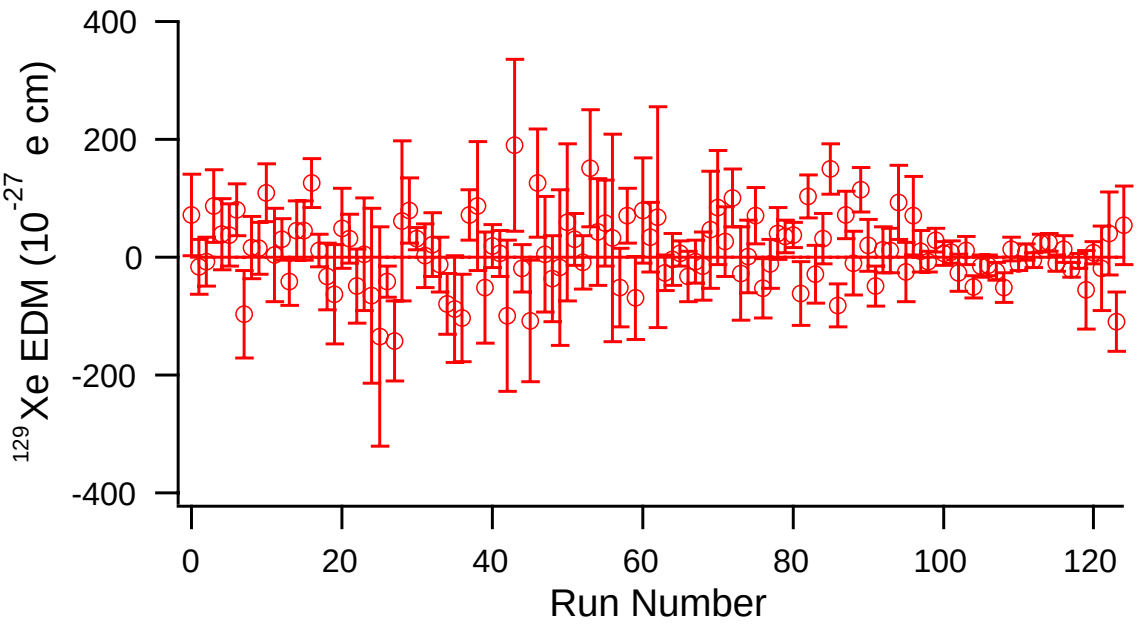

Figure 5.32: EDM's for each run (Method Three String Analysis)

Run Date	N	$\vec{B}$	HV	EDM Value	EDM Error
April0299	19	West	3.493	7.209e-26	6.883e-26
April0599	21	West	3.493	-9.025e-26	6.327e-26
April0699	16	West	3.493	-7.577e-27	4.146e-26
April0999	26	West	3.493	8.697e-26	6.150e-26
April1599	21	West	3.493	7.049e-26	6.222e-26
April1699	21	West	3.493	3.732e-26	5.29e-26
April1799	31	West	3.493	7.994e-26	4.345e-26
April1899	21	West	3.493	-9.700e-26	7.474e-26
April1999	21	West	3.493	1.593e-26	5.328e-26
April2299	25	West	3.584	1.507e-26	4.392e-26
April2799	21	West	3.560	9.070e-26	5.991e-26
April2899	25	West	3.593	2.826e-27	7.509e-26
April2999	28	West	3.593	3.044e-26	3.479e-26
April3099	37	West	3.593	-4.120e-26	4.035e-26

Table 5.13: d_{Xe} for each run (Method Two String Analysis)

Run Date	N	$\vec{B}$	HV	EDM Value	EDM Error
May0199	33	West	3.593	4.574e-26	5.040e-26
May0299	29	West	3.593	8.093e-26	6.603e-26
May0499	23	West	3.593	1.263e-25	4.132e-26
May0799	98	West	3.593	1.122e-26	2.785e-26
May1099	50	West	3.593	-4.485e-26	5.57e-26
May1199	46	West	3.593	-6.340e-26	8.409e-26
May1299	29	West	3.742	4.864e-26	6.763e-26
May1399	36	West	3.742	3.138e-26	4.195e-26
May1499	29	West	3.742	-4.905e-26	6.309e-26
May1599	32	West	3.593	5.404e-27	9.531e-26
May2299	21	East	3.593	-2.105e-27	1.246e-25
May2399	14	East	3.593	-1.314e-25	1.982e-25
May2499	26	East	3.593	-4.800e-26	3.220e-26
May2599	31	East	3.593	-1.424e-25	6.843e-26
May2699	29	East	3.593	-6.793e-26	1.857e-25
May2799	24	East	3.593	-1.993e-26	7.315e-26
May3099	36	East	3.593	6.930e-27	2.264e-26
June0199	36	East	3.593	-1.909e-26	4.763e-26
June0299	31	East	3.593	2.173e-26	5.382e-26
June0499	36	East	3.593	-1.296e-26	4.700e-26
June0599	26	East	3.593	-7.986e-26	5.103e-26
June0699	26	East	3.593	-1.516e-25	8.557e-26
June0799	29	East	3.593	-1.035e-25	7.45e-26
June0899	61	East	3.593	1.065e-25	5.492e-26
June1099	24	East	3.593	8.674e-26	1.098e-25
June1199	36	East	3.593	-4.805e-26	9.371e-26
June1299	23	East	3.593	3.805e-26	2.368e-26
June1399	36	East	3.593	6.807e-27	3.908e-26

Table 5.14: d_{Xe} for each run (Method Two String Analysis)

Run Date	N	$\vec{B}$	HV	EDM Value	EDM Error
June1499	26	East	1.796	-9.964e-26	1.288e-25
June1599	36	East	1.796	1.302e-25	1.417e-25
June1899	102	East	3.593	-1.922e-26	3.968e-26
June2299	31	East	1.796	-1.077e-25	1.030e-25
June2499	36	East	3.638	1.121e-25	9.377e-26
June2599	26	East	3.638	-1.025e-25	1.111e-25
June2699	36	East	3.638	-3.602e-26	7.274e-26
June2899	29	East	3.790	-1.793e-26	1.325e-25
June2999	26	East	3.790	5.907e-26	1.336e-25
June3099	31	East	3.790	2.974e-26	4.360e-26
July0199	31	East	3.790	1.998e-26	4.532e-26
July0299	21	East	3.790	1.506e-25	9.976e-26
July0399	36	East	3.790	4.241e-26	8.996e-26
July0499	31	East	3.790	5.743e-26	8.211e-26
July0599	31	East	3.790	3.357e-25	1.516e-25
July0799	31	East	3.790	-5.093e-26	6.634e-26
July0899	99	East	3.790	6.538e-26	4.586e-26
July1199	36	East	3.790	-6.835e-26	7.143e-26
July1299	21	East	3.790	7.887e-26	8.920e-26
July2899	24	West	3.638	3.443e-26	5.969e-26
July2999	21	West	3.638	6.762e-26	1.874e-25
July3099	26	West	3.638	-2.609e-26	3.422e-26
July3199	31	West	3.638	9.999e-28	4.448e-26
August0199	13	West	3.638	6.282e-27	2.120e-26
August0299	36	West	3.638	-3.287e-26	4.275e-26
August0499	26	West	3.638	-7.949e-27	3.632e-26
August0599	21	West	3.638	-1.912e-26	5.683e-26
August0699	21	West	1.819	4.671e-26	9.883e-26

Table 5.15: d_{Xe} for each run (Method Two String Analysis)

Run Date	N	$\vec{B}$	HV	EDM Value	EDM Error
August0899	26	West	1.819	5.241e-26	1.006e-25
August0999	16	West	3.638	2.712e-26	5.892e-26
August1399	31	West	3.638	9.813e-26	5.378e-26
August1499	35	West	3.638	-3.498e-26	6.243e-26
August1599	46	West	3.638	-7.819e-28	6.130e-26
August1699	53	West	3.638	5.813e-26	4.604e-26
August1799	35	West	3.790	-5.335e-26	5.044e-26
August1999	31	West	3.790	3.670e-26	5.132e-26
August2099	36	West	3.790	4.070e-26	4.371e-26
August2199	36	West	3.790	3.069e-26	2.847e-26
August2299	26	West	3.790	3.791e-26	2.121e-26
August2399	36	West	3.790	-6.162e-26	5.371e-26
August2499	36	West	3.790	1.034e-25	3.644e-26
August2699	29	West	3.790	-8.177e-27	4.970e-26
August2799	31	West	3.790	1.622e-26	4.103e-26
August2899	54	West	3.790	1.458e-25	4.706e-26
August3099	28	West	3.638	-9.048e-26	3.881e-26
August3199	36	West	3.790	7.167e-26	4.042e-26
September0299	26	West	3.790	-6.636e-27	5.882e-26
September0399	36	West	3.790	1.141e-25	3.728e-26
September0499	31	West	3.790	2.038e-26	4.403e-26
September0599	29	West	3.638	-4.946e-26	3.356e-26
September0699	31	West	3.638	3.377e-26	4.169e-26
September0799	36	West	3.638	1.186e-26	3.718e-26
September0899	26	West	3.638	9.300e-26	6.288e-26
September0999	31	West	3.638	2.074e-26	5.684e-26
September1099	36	West	3.638	7.014e-26	6.663e-26
September2699	26	East	3.638	-2.884e-27	3.021e-26

Table 5.16: d_{Xe} for each run (Method Two String Analysis)

Run Date	N	$\vec{B}$	HV	EDM Value	EDM Error
September2799	36	East	3.638	-2.034e-26	1.846e-26
September2899	36	East	3.638	2.849e-26	1.960e-26
September2999	36	East	3.638	-1.493e-26	2.061e-26
October0199	92	East	3.638	8.161e-27	1.852e-26
October0599	26	East	3.790	-2.957e-26	3.377e-26
October0699	26	East	3.638	-1.960e-26	3.187e-26
October0799	36	East	3.638	-4.999e-26	1.869e-26
October0899	26	East	3.638	-1.463e-26	1.789e-26
October0999	36	East	3.638	-1.242e-26	1.902e-26
October1099	36	East	3.638	-2.428e-26	1.454e-26
October1199	33	East	3.638	-5.182e-26	2.538e-26
October1299	19	East	3.638	1.414e-26	1.969e-26
October 1399	26	East	3.638	-1.183e-26	1.137e-26
October1499	46	East	3.638	8.610e-27	1.422e-26
October1699	26	East	3.638	-5.016e-27	1.290e-26
October1799	26	East	3.638	2.364e-26	1.562e-26
October2899	36	East	3.638	2.144e-26	1.481e-26
October2999	36	East	3.638	-1.134e-26	1.305e-26
October3099	32	East	3.638	-1.111e-26	2.544e-26
October3199	26	East	3.638	-2.094e-26	1.312e-26
November0199	36	East	3.638	-7.166e-27	1.305e-26
November0299	26	East	3.638	-5.498e-26	6.615e-26
November0699	33	East	3.638	7.79e-27	1.918e-26
November1999	36	West	3.638	-1.829e-26	7.094e-26
November2099	66	West	3.638	4.010e-26	7.056e-26
November2499	66	West	3.638	-1.089e-25	5.071e-26
December0199	56	West	3.638	5.435e-26	6.615e-26

Table 5.17: d_{Xe} for each run (Method Two String Analysis)

CHAPTER VI

Future Work

This experiment still falls short of a world-class EDM measurement. However, a great deal has been learned in six months of running, and further improvements are still quite probable. In addition, our collaborators at the Smithsonian Astrophysical Observatory have already begun a second measurement of the ^{129}Xe EDM that may be substantially better than the value reported here. The SAO experiment is very similar in most respects, since they studied most of the components of the Michigan apparatus prior to building an improved, second generation version. Therefore, the work that has been performed here may still develop into an experiment that sets new limits on the size of **T**-violating effects.

In this chapter I discuss some potential modifications to the apparatus that could yield an improved EDM value for the Michigan system. Some of these modifications have already been implemented by our SAO collaborators, others have been prototyped here at Michigan but not perfected, and a few are based on very preliminary tests or models. There are several routes to obtaining a better limit on d_{Xe}: eliminating systematic effects, increasing the electric field strength or reducing the instability in the maser frequencies. Some ideas for each approach are discussed below.

At the end of the chapter I discuss the option of using a different species to obtain a more stringent limit on the **CP**-violating parameters that are the motivation for the experiment. In particular, very heavy atoms such as radon or radium possess nuclear enhancements that should dramatically increase the size of their EDM's compared to xenon or mercury. A brief presentation of the advantages and limitations of using these atoms is given.

6.1 Short-term Work: Known Issues

The first issue in improving this measurement is to understand and eliminate the systematic effect that causes the measured frequency to in a manner that correlates with the electric field. In Chapter Five I presented some measurements of the size of this effect, but its physical origin remains unknown. Some hypotheses that are being considered are listed below.

An important part of understanding the origin of the systematic is to determine what, if anything, changes the size of the systematic. One approach is to measure the systematic for different T_2's and pick-up coil resonances, without changing the magnetic field direction. Another test would be to run with a different cell, to see if there is something peculiar about E17. I had intended to do this at an earlier point, but two cells failed abruptly, thwarting these attempts. In addition to changing cells or cell orientation, it should be trivial to switch the leads to the endplates or even exchange the roles of the positive and negative high voltage supplies, until all permutations have been tested. By running a sufficiently large number of measurements, any patterns pointing to a non-zero systematic will become apparent. These measurements are easy in principle, but it will require time to achieve the needed level of precision.

It would really be more satisfying to understand why the systematic is present at all. One idea is that when the electric field is changed some current (a few nA) flows in the HV wires. Since these wires make a loop through the system, a small magnetic field is generated. This could change the magnetization of the shields, leading to a small change in the frequency that correlates with the electric field direction, but not the magnetic field direction. However, the maximum effect that could be generated by such a small current would be 100 times smaller than the presently observed effect. Still, it would be worth investigating if the size of the systematic scaled with the current preceeding the scan instead of the total change in magnitude. To do so, one just has to change the rate at which the electric field is ramped up and down.

A second hypothesis is that the noise due to the electric field is different in the two orientations, and that this changes the performance of the magnetic phase locked-loop enough to shift the helium frequency. The change in noise characteristics is

actually an established fact: previous tests have shown that one HV plate of the cell tends to have more discharges than the other, and that the negative high voltage supply tends to be noisier than the positive. The question is therefore how much of an effect this has on the magnetic lock loop. This can be tested by changing the noise characteristics, most easily by changing the cell or HV filters as described above. Various conditioning tests can also be run, to see if the systematic effect changes if the electric field is left in one orientation for a long period of time.

Another way to determine if the noise in the lock-loop is the problem is to use some other method of stabilizing the magnetic field. If the locking did not rely on either maser signal. then this would also allow study of the two masers separately. Such study would greatly enhance our understanding of the magnetization shifts and the shifts due to different maser ensemble positions. Clearly an alternative form of locking could help unravel a number of mysteries.

A Rb magnetometer is one possible method to stabilize B. Just as with the noble gases, rubidium has hyperfine levels that separate in a magnetic field. Therefore, the energy of the transition between these hyperfine states has the same B dependence as the noble gases and can be used to lock the field in the same way. The rubidium magnetometer apparatus would be independent of the present system. To operate it, a small, single cell containing Rb and N_2 is placed in a separate, smaller oven that goes partway into the solenoid. This design has the advantages of using the present shielding to limit the noise and that the Rb cell sees the same magnetic field as the masers. The oven is kept at a modest 65 °C, and includes a photodetector that sits directly behind the cell. A low-power (30 mW) diode laser tuned to the Rb D2 resonance shines onto the cell and polarizes the rubidium. The use of 780 nm (D2) light, in conjunction with a light pipe, eliminates the background from the D1 pumping light. An rf field is then applied to the cell, generated by two small coils placed on either side of it. The rf signal comes from an SRS DS345 unit, which runs at 700 kHz. This is very close to the Zeeman splitting in the hyperfine sub-levels of ^{85}Rb in the solenoid's field. When the frequency is matched precisely, the hyperfine states are mixed, reducing the polarization of the Rb and making it possible for the newly unpolarized Rb to absorb laser light. The photodiode in the oven observes this dip in the transmission. By modulating the rf amplitude (around .5 Vpp), it is

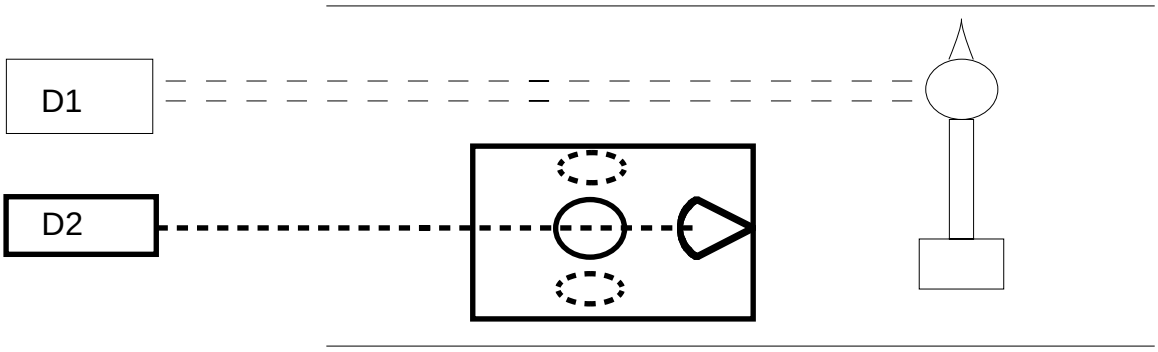

Figure 6.1: Rubidium Magnetometer within the Magnet

possible to obtain an AC signal.

Several years ago I built a prototype of this system used it to obtain rubidium signal. When used to lock up the magnetic field, the stability of the system improved by a factor of twenty when compared to data with no control loop. However, this is still a factor of thirty worse than achieved with the masers. The reasons for this were not clear, but the system probably just needed better control of the oven temperature, laser power, etc., to obtain a rubidium signal of the needed stability. A more vigorous second attempt might make it possible to study the maser frequencies (and so the magnetization shifts) in more detail.

The issue of what pick-up coil arrangement should be used also merits further study in the near future. One source of concern with the two pick-up coil arrangement is its greatly increased effect on the maser position shift (refer to section 4.2.3). One solution is to use one pick-up coil for both species. This technique was developed by our collaborators at the Smithsonian Astrophysical Observatory [77]. The SAO system uses a single pick-up coil within the oven, connected to an external "tuning" coil (refer to figure 6.2). The result is a single pick-up coil with two resonances.

Solving for the response of the circuit is straightforward in principle, though the impedance is considerably more complicated. In order to for the circuit shown in figure 6.2 to have resonances at desired angular frequencies ω_X, ω_H, one must set the capacitances to be [77]

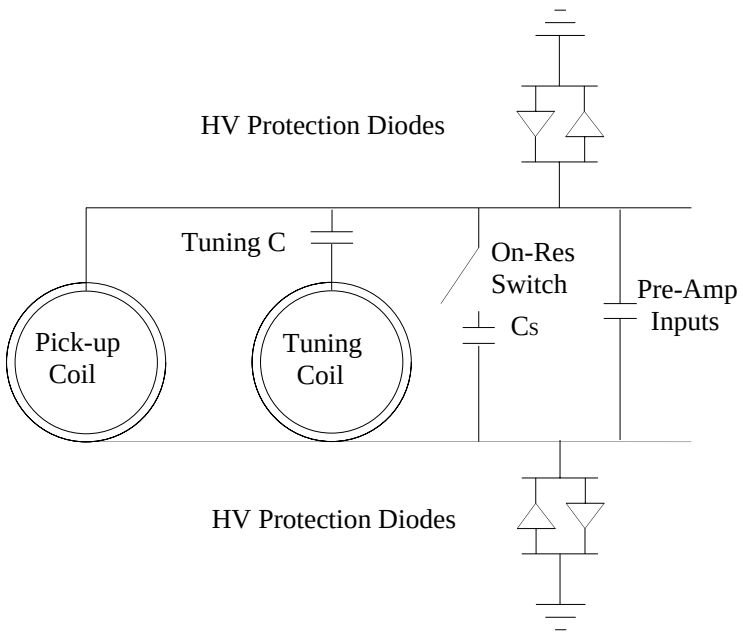

Figure 6.2: SAO Pick-up Coil Circuit

$$C_1 = \left(2L_1\left[\omega_H^2+\omega_X^2-\sqrt{(\omega_H^2+\omega_X^2)^2-4\omega_H^2\omega_X^2(1+\frac{L_2}{L_1})}\right]\right)^{-1} \quad (6.1)$$

$$C_2 = \left(2L_2(1+\frac{L_2}{L_1}\left[\omega_H^2+\omega_X^2+\sqrt{(\omega_H^2+\omega_X^2)^2-4\omega_H^2\omega_X^2(1+\frac{L_2}{L_1})}\right]\right)^{-1} \quad (6.2)$$

for some arbitrary choice of the inductances L_1, L_2. This value of the capacitance includes the stray capacitance of the coaxial cable and the pre-amps, and the "tuning" capacitance used to set the off-resonance peaks, so the amount of capacitance switched in (C_S) would be reduced by this amount. Determining the quality factor Q for these resonances involves still more algebra, and is best done numerically. Estimates of Q for this configuration are around 10 for the xenon and 25 for the helium. The use of this system should reduce the size of the maser position shift by a factor of at least three. It may also reduce the instability of the free-running maser, if the different maser positions make it harder for the magnet's PLL to compensate for various drifts.

Alternately, the pick-up coils could be switched. For the EDM data presented in this thesis the xenon-tuned coil is closer to the pump bulb than the helium-tuned coil: reversing them should also achieve a reduction in the maser position shift. However,

some preliminary measurements made with this configuration revealed that the upper coil is being affected by high voltage noise much more strongly than the lower coil is. The result was continuous perturbations that introduced substantial helium maser oscillations, reducing the frequency stability by a factor of 6 or so. This effect should also be investigated, by switching to a new cell and changing the HV leads.

The fluctuations in room temperature may also be a problem for the system. For example, the output of the PI controller that feeds back into the magnet PLL is almost always correlated with room temperature, probably due to the effect of the shield's magnetization. The spectrum of the lasers can also depend on the room temperature, and so might the resistance of the low-pass filters used on the high voltage leads. For this reason it may be advisable to enclose the entire table-top in styrofoam insulation, and control the interior temperature with an Omron (refer to section 2.2.3). This should easily reduce the temperature fluctuations by a factor of three.

6.2 Long-term Work: Possible System Improvements

The previous section dealt with problems that we know exist in the present system. The present section is intended to discuss more general improvements. Each of these tests a specific hypothesis for what is limiting our EDM measurement. It is true that, except for increasing the electric field, it is hard to say what modifications would actually improve the EDM sensitivity. However, there are some systems that clearly introduce noise of some kind or another. Eliminating such noise might very well improve the measurement, especially if the modifications discussed above have already improved the sensitivity.

The most direct way to improve the Xe EDM sensitivity is to run at a higher field. The presence of helium in the cell sets an upper limit of 7 kV/cm, but that still leaves room for a 75% improvement. The problem has been corona effects and discharge to the pick-up coils. To prevent this, a dielectric fluid can be placed around the maser bulb. One possibility is SF_6, a gas commonly used in high voltage work. Having such a gas would require a re-circulating system for the "airflow" that controls the maser temperature. Another possibility is transformer oil, for example type Diala

AX 68702 [24]. Some preliminary work indicates that the oil does dramatically reduce discharge effects, but it also vastly enhances the leakage current. To reduce the leakage current, separate compartments for the oil near each cell endplate would have to be used.

Next, there is class of improvements that concern attempts to improve our T_2. As discussed in Chapter Four, a better T_2 helps the system in a number of ways. The size of T_2 determines the size of P_z, and so the magnetization shift and the cavity pulling. A larger T_2 also means smaller gradients, which would mean a smaller maser position shift. A better T_2 also puts the maser further above threshold, reducing the size of near-equilibrium oscillations resulting from perturbations. Given all these effects, the importance of T_2 in obtaining reduced maser instabilities should be emphasized. Indeed, the better sensitivity of the East runs compared to the West runs (see Chapter Five) was due to the improved T_2 from mid-September to early November of 1999.

One procedural modification to improve T_2 values is to degauss and retune the gradients several times if necessary. The delay of several days is worth the improved quality of the data. Related to this tuning is the problem of the gradients in the transfer tube, which play a significant role in determining T_2 . Designing a suitable correction coil to trim away such gradients is difficult. One possible method to remove such gradients is a double cell oven which runs two cells (top-bottom-bottom-top) in an attempt to cancel out the gradients. This would involve considerable effort in building or acquiring the additional control electronics, but since the needed systems are already understood the project might be accomplished fairly quickly.

Another way to improve T_2's is to use "choke coils" near the maser bulb. (This is another innovation of our SAO collaborators [77].) The choke coils are simply four sets of wires, each wrapped around the transfer tube several times and then soldered to itself to form a closed loop. The loops act to oppose the field generated in the transfer tube, so that the total signal has a smaller contribution from the atoms within the transfer tube. Improvements of 20-30% in the Xe T_2 have been experimentally verified in the SAO apparatus.

The oscillations of the maser amplitudes (described in Chapter Five) are also a source of concern. It is possible to reduce the effect of the P_z oscillations on

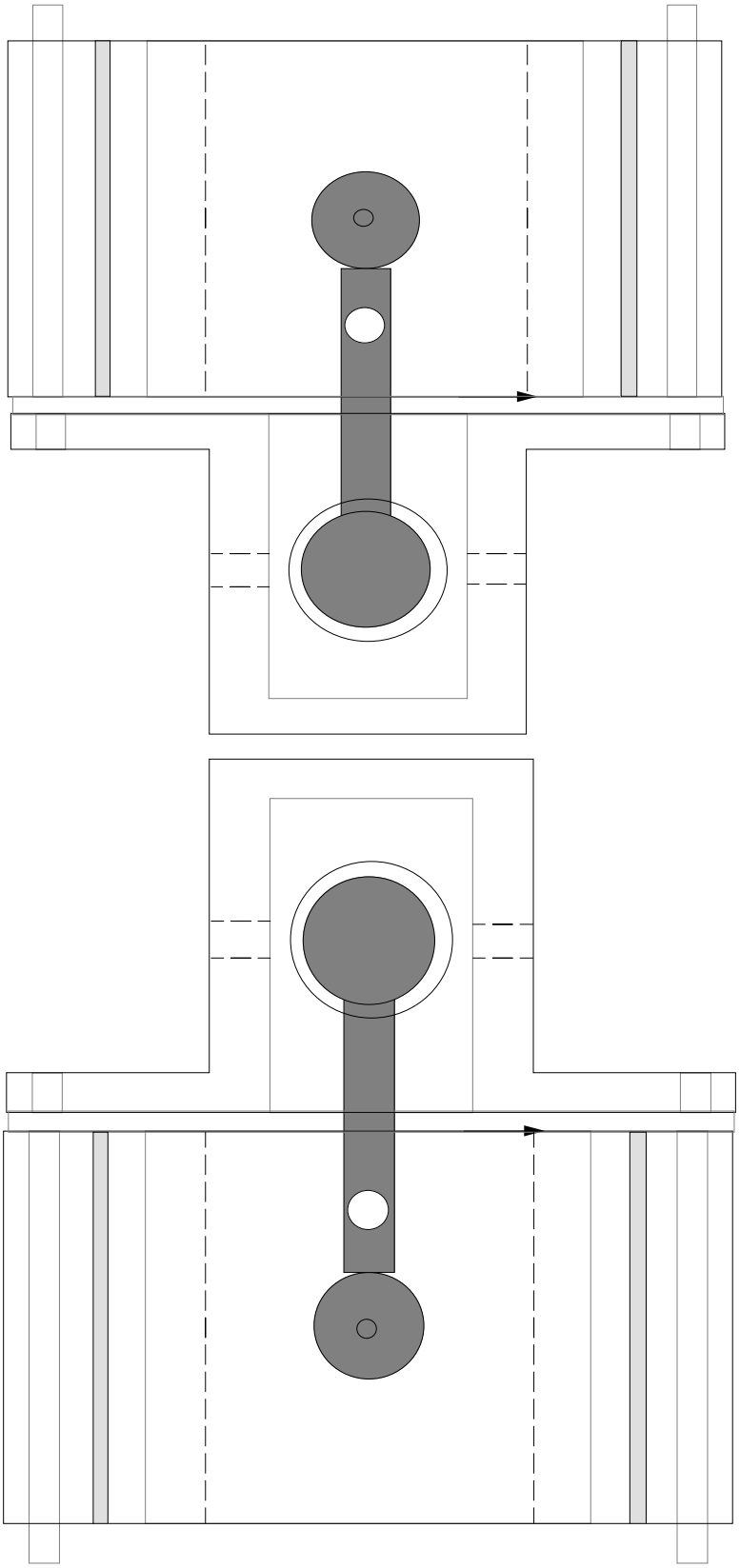

Figure 6.3: A top-bottom-bottom-top double cell arrangement

the frequency. Recall from Chapter Four that P_z shifts the frequency through the magnetization shift, and also through cavity pulling. These two frequency shifts can cancelled out by tuning the pick-up coil resonances properly. Rick Stoner at SAO has also developed this system of "magic detunings" [86] and it has been experimentally verified to reduce the effects of P_z oscillations.

One likely source of noise in our system is the vibration introduced by our air flow. The noise observed on the pick-up coils is reduced substantially when the air is turned off. The hypothesis is that the air is moving the coil and/or the cell within the non-uniform magnetic field, which naturally leads to induced noise. Reducing the flow rate would reduce the noise caused by such vibration. For example, less air would be needed to cool the maser cell if it the air were chilled by passing it through a copper tube immersed in liquid nitrogen. For the pump chamber, the air flow can be eliminated entirely through the use of an rf heating circuit. Small circuits in Kapton tape are suitable for wrapping around the glass chambers of the cells. By using two circuits back to back to cancel out the current, and by running at around 200 kHz, the effects of magnetic fields or gradients are reduced to a manageable level (i.e. the noble gas polarizations are not reduced). The rf heating may even be able to provide better temperature control, reducing the effects of density fluctuations for example. A prototype of this system has already been constructed, so that full implementation would be much easier.

The vibrational noise can also be reduced by switching the type of oven material used. An alternative to Nylatron is Zerodur, which has a lower coefficient of expansion and greater rigidity. Right now a lack of correlation with oven temperatures implies that there are no expansion problems, but more rigid connections might be the easiest way to reduce vibrational effects.

Another source of noise is the drift in the laser power and frequency that leads to a change in the maser amplitudes. This is much more of a problem for the Opto-Power units that it is for the Coherent laser, and will be even less important when the entire table-top is temperature controlled. However, it might at some point be necessary to improve the control even for the Coherent. A system to control the Opto-Power lasers has already been implemented at SAO [77], and this could easily be modified for the Coherent as well. A copy of the control system was made in

Michigan, but was never fully implemented.

Correcting the drift in the laser output is a two part process, essentially a rough control using current and a fine control using temperature. To correct the laser current, the output power of the laser is monitored . A small part of one beam is split off , sent it through a chopper, and then onto a photodiode. A lock-in amplifier picks out the AC signal, which is then compared to a constant voltage, typically 4.0 V. An offset is added to the AC signal to match this, and then the error signal is fed to a PI control circuit. The output of the circuit adjusts the current of the laser diode to prevent large drifts.

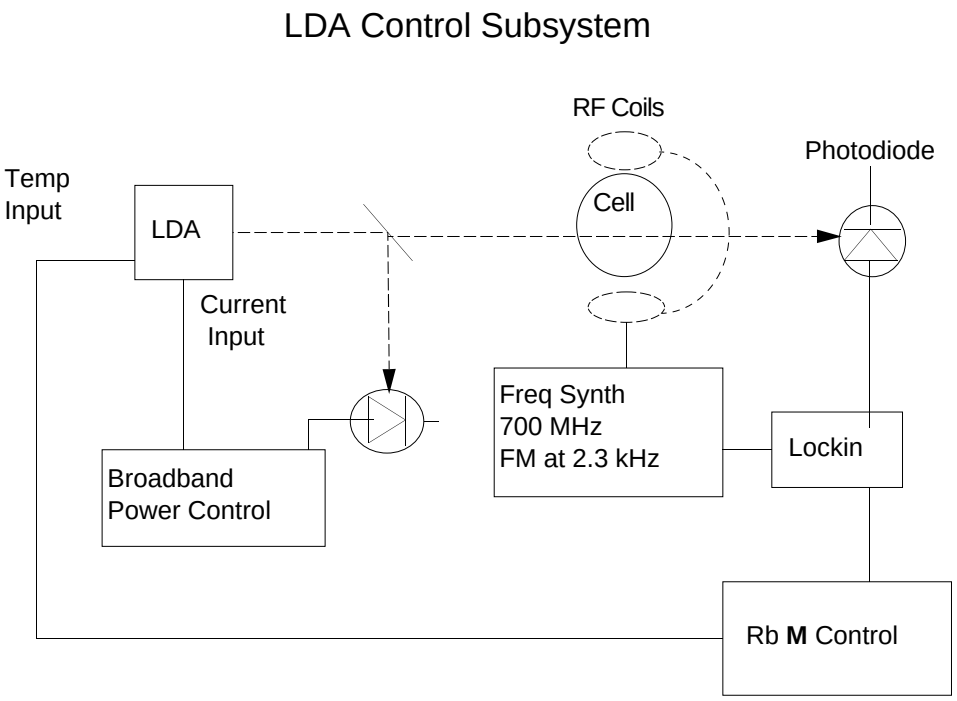

Figure 6.4: Laser Control Sub-system

This turns out to correct most of the maser drift. If even better stability is desired, the temperature of the diodes can also be controlled, to stabilize the frequency of the laser. This is done though use of a rubidium magnetometer, similar to the one described above. In this case the rubidium in the pump bulb is used, and the transmission of the pumping laser itself is observed. The only modifications inside the shields are a pair of rf coils are added to the sides of the oven. The transmitted light is observed by a photodiode sitting in a temperature stabilized box just outside

the shields. A piece of ground glass sits in between to spread out the light and reduce the effects of slight path changes. The photodiode output is fed to an SR830 lockin amplifier and then to another PI control circuit. This output of the circuit modifies the set voltage from the laser controller to control the laser diode temperature. By controlling to the Rb magnetization, one controls for a particular γ_{opt}. This eliminates concerns about slipping into a trough in the complex laser beam profile. However, since applying the rf field to the rubidium lowers its polarization, this second stage of control will only be useful if the stability is improved from present levels.

Finally, the work at SAO has also shown that the performance of the control systems can be improved through the use of better electronics. For example, the stability of the reference frequencies can be improved an order of magnitude by using Wave-Tek Model DDS29 units [93] tied to a DS345 reference. The magnetic field control loop and temperature control loops can be improved by using LR130 [57] for the PID controllers. This clearly improved the temperature stabilities to about 5mKrms, and may also contribute to the better frequency stability of the SAO system. Given the present size of the free-running maser frequency uncertainty, and a lack of correlation with system temperatures, these improved control loops would only play a role if other sources of instability are reduced.

6.3 ^{223}Rn EDM

It may be possible to make sufficient improvements in the present system to reach the 10^{-28} e cm level, or even an order of magnitude lower than this. This would translate into perhaps a factor of ten improvement in the accuracy to which **T**-violating parameters are known. In order to improve substantially on this, the use of a different species is required.

As mentioned in Chapter One, the size of the **T**-violating effects that generate an EDM scale with the atomic number Z^2 or Z^3. On that basis, switching to an atom such as radon or radium would therefore increase the sensitivity by a factor of 3 or 4. There is more to the story, though. The work of Flambaum, et al. [28] has shown that there is a mechanism that can greatly enhance the size of an EDM. The mechanism arises for atoms with a substantial octopole deformation, arising from closely spaced

parity doublets in the atom's nuclear spectrum. Combining this effect with the usual Z^2 enhancement described above, the authors predict an electric dipole moment in radon-223 that is 4000 times the size of a xenon-129 EDM, and values for radium-223 and -225 are comparable. All these isotopes are radioactive, but the possibility of making a very sensitive measurement of the size of the nucleon-nucleon interactions makes it worth pursuing an EDM measurement in one of these species.

In many respects, ^{225}Ra is the best candidate for these measurements. Unlike the other isotopes it is spin 1/2, which eliminates complications due to magnetic quadrupole interactions. The half-life of ^{225}Ra is 15 days, and it can be produced much more easily than radon. The disadvantage to radium is that it is difficult to polarize, which is an important limitation in making an EDM measurement. ^{223}Rn, on the other hand, is a noble gas that can be polarized in exactly the same way that xenon and helium are. It is therefore natural to turn to radon for our experiment. The remainder of this section will focus on how to measure a ^{223}Rn EDM.

The experimental technique for measuring radon frequencies is straightforward, and has been tested for other noble gas isotopes [6],[50]. The latter reference describes a measurement of the magnetic dipole moment of radon-209, which very similar to radon-223 in terms of half-life (29 versus 23 minutes). To measure an electric dipole moment, the only fundamental change required is the addition of an electric field. From that point, it becomes a matter achieving the needed experimental sensitivity. The following discussion will assume radon is the species to be measured.

The key components of the experimental apparatus are sketched in figure 6.5. The first step of the procedure is to generate the needed radioactive isotope. In previous work this occurred at the ISOLDE facility of CERN. A proton beam impacting onto a ThC_2 target produces radon through a spallation reaction. The resulting beam of radon ions is mass-separated, and the desired isotope is stopped by a tantalum foil. When enough radon has become trapped in the foil, the chamber is isolated and the foil is heated to release the radon gas. The gas is then cryopumped into a prepared cell, as described in section 2.3, and a quantity of nitrogen and a noble gas such as neon are added. The nitrogen is needed to quench the excited rubidium during optical pumping. The noble gas serves as the reference species, to accurately determine the magnetic field.

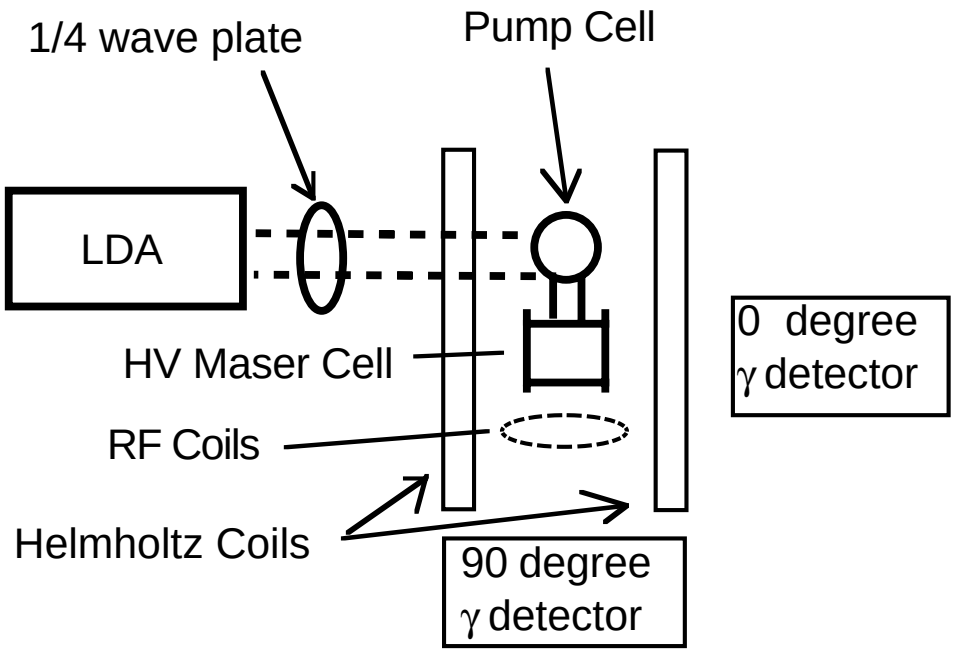

Figure 6.5: Experimental apparatus for measuring the atomic EDM of a radon-223

The cell is then placed in an optical pumping apparatus, and the gases are polarized as described in section 3.2. The radon polarization is measured by observing the anisotropy of the γ-rays emitted when the radioactive isotope decays. Unfortunately this anisotropy is not very large, being about 10% even for a fully polarized sample. To determine the frequency, an oscillating magnetic field is applied to the cell. When the frequency of the rf field matches the atomic frequency, the atomic polarization is destroyed and the γ-ray anisotropy vanishes. (This is completely analogous to the Rb magnetometer set-up described in section 6.1.) By observing the change in frequency as an electric field is applied, the atomic EDM can be measured.

The sensitivity achievable with this set-up depends on the electric field, the achievable polarization, and the number of available atoms. Assuming that the uncertainty is limited by statistics, a reasonable estimate of the sensitivity is given by

$$\begin{aligned} \mathrm{d_{Rn}} &= \frac{\hbar\,\delta\omega}{2\mathrm{E}} \\ &\approx \frac{\hbar}{2\mathrm{E}\mathrm{T}_2^{\mathrm{eff}}(0.1\mathrm{P_{Rn}})\sqrt{\mathrm{N}_{\gamma-\mathrm{ray}}}} \end{aligned} \tag{6.3}$$

Since there will be no helium present in the cell, the electric field can probably be at

least 10 kV/cm and perhaps higher. ^{223}Rn has a nuclear spin of 7/2, and therefore will have more interactions with the walls of the cell compared to ^{129}Xe: however, its larger size also means that it will be easier to polarize. Thus polarizations of at least 50% should be easy to achieve with diode lasers. The T_2^{eff} will principally be limited by T_1, and will be about 100 seconds.

The number of gamma-rays one could collect is the principal concern. Since the gamma-ray detectors will only cover a small portion of the 4π steradians of solid angle, one probably needs about 100 times as many atoms as gamma rays. (This factor could also include losses from atoms that decay before they can be transferred to the cell and polarized.) The number of ^{223}Rn atoms ISOLDE can produce about 5 $\times 10^6$ per second. Given these values, one could obtain about 10^{11} γ-rays in a month of running. The estimated experimental sensitivity for the ^{223}Rn EDM would then be about 4×10^{-26} e cm. Since the radon should be 4000 times more sensitive to **T** violating nuclear effects than xenon-129, the limits on the parameters in table 1.1, would be improved by about an order of magnitude over the present best limits.

Of course there will also be other uncertainties, such as shifts caused by the magnetized gases, etc. However, many of the potential systematic effects will already be understood. The use of a dual-bulb cell can remove the shifts caused by polarized rubidium that would be of the most concern. (In fact, several refillable cells would probably be used, to minimize the dead time.) Furthermore the use of xenon as a reference frequency will remove concerns about magnetic field drifts and leakage currents. Overall the experiment has a good chance to reach the statistical limit quoted above.

APPENDICES

APPENDIX A

EDM Cell Design

The previous chapters have shown that the dual-species maser is a very complex tool, and that many factors affect its stability. Chapter Four explained that large signals are not necessarily better for the measurement, since they may be correlated with large gradients. Overall, the system wants the best possible transverse polarization with the lowest possible longitudinal polarization in as high an electric field as can be managed. Many of the factors that determine these for the masers are set when the EDM cell to be used is designed. This section is intended to give some understanding of the reasons for the design that was eventually employed.

Listed below are the different pieces of cell design that must be considered for EDM cells. Each piece impacts the ultimate performance of the system in one or more ways, and the final value used is typically a compromise between the competing effects. Variations in coatings from cell to cell (the "black magic" of cell-making) make it difficult to fine tune these parameters, so each has only been roughly optimized. In some cases calculations have indicated that further adjustments might prove useful: these are mentioned when relevant. The final section discusses the collaboration's observations of cell aging and deterioration.

There are two different pieces to cell design. One is the physical geometry: the size and shape of the pump bulb, maser bulb, and transfer tube. The choices for these are limited by the styles of glass tubing available. The other piece is the density of the gases put in to the cell: xenon, helium, and nitrogen. Here the limit is set by the need to pull the cells off the system. Using liquid nitrogen, this limits the pressure 2800 torr of helium and nitrogen. One also has to be careful of the risk of

blowing the endplates off the maser cylinder at high pressures. However, the modern cell pressures are relatively low and do not approach these limits.

The geometry of the pump bulb determines the intensity of laser light that shines on the atoms. The use of a spherical pump comes mostly from ease of production: a cylindrical model should work equally well. The size is set by the need for a high laser intensity and a reasonable volume of polarized gas. Given the high power of the lasers employed, the intensity of the light throughout the cell is fairly uniform. With the size of the present laser beams, a slightly larger pump cell might be advisable.

The diameter of the transfer tube affects the escape time from each bulb (G_m and G_p) and the F for the xenon (see the discussion in section 3.6). The two effects compete here: a narrower transfer tube means less transport and so better T_2^{eff}'s, but reduced xenon maser polarization. In addition, a narrow transfer tube makes it harder to clean and pump out the cells (which reduces T_1), but slows the rate of Rb loss and so extends the cell's lifetime. The cell used for data-taking had a transfer tube of inner diameter 3.25 mm, but in fact most cells have either a 3.95 or 4.2 mm ID. All three types are adequate, though the 3.95 mm model seems to be the optimum. The length of the transfer tube has a modest effect on the transport time as well as influencing the magnetic field gradients. 4.0 cm seems to be about right, but this parameter has not explored a great deal.

The maser bulb volume affects escape time and signal size. Its length is important in the maximum E field we can achieve. Its overall shape affects the coupling to the pick-up coils and the shifts and gradients caused by the atomic magnetization. The present design is a reasonable compromise between the effects of gradients and the strength of the E field. However, fatter, shorter cells might improve performance slightly.

The density of nitrogen primarily affects the E field limit, as the He in the cell will break down without a modest amount. The present value of 80-100 torr seems perfectly adequate. This amount of nitrogen is also sufficient for quenching the excited rubidium. Higher densities of N_2 simply impede diffusion and so harm T_2. The nitrogen does contribute to the pressure broadening of the rubidium absorption line, which affects γ_{opt}. However, the noble gases also increase the line width, with nearly the same coefficient. Therefore it is preferable to simply add more helium

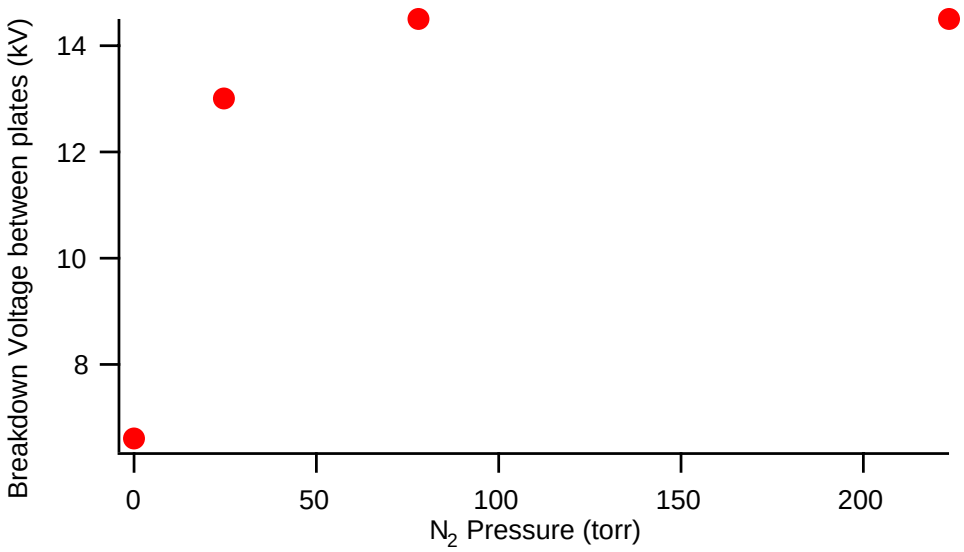

Figure A.1: Breakdown Voltage as a function of $[N_2]$ in two atmospheres of helium at 20°C

(which increases the size of the helium signal) if more pressure broadening is needed.

The noble gas densities are very important for a variety of reasons. As mentioned earlier, the xenon density dominates in determining the rubidium Γ_{sd}, whereas the helium density dominates in determining γ_{opt}. The noble gas densities also determine the strength of the signal and radiation damping, the size of magnetization gradients and shifts, and the diffusion constants that determine escape times, transport times, and the motional averaging of T_2. In designing cells it is important to note that the different parts of T_2^{eff} depend on density in different ways (refer to equation 3.69). The T_2 from field gradients given above drops sharply with density, while the transport effects grow stronger at lower densities. τ_{rd} has a complex density dependence, whereas T_1 is independent of density for any reasonable pressure.

Work with previous cells has demonstrated that the helium T_2 is generally close to the limits imposed both by the escape time and by the atomic magnetization gradients. The xenon, which is heavier and has a smaller magnetic moment, is more forgiving on both counts. It is generally limited by a combination of atomic magnetization gradients and the T_1. Most early work was with cells of 200 torr Xe and 3 atm He. For cells made entirely of glass these higher densities were needed to get τ_{rd} small enough for to masing to occur. More recent work has been with

EDM cells, which have a better Xe T_1. In this case the increased gradients from the improved magnetization became the limiting factor . To compensate, the densities of both species were reduced by a factor of two. Signal sizes remained fairly constant, and the Xe T_2 rose somewhat. The He T_2 also improved a little, until it was clearly limited by escape time.

There are two possible reasons why the cells made entirely of glass consistently had a worse Xe T_1 than those with metal endplates. First, the glass cells are more difficult to clean and coat, and so glass cells may not have a really good OTS layer. Second, the Xe may actually experience less relaxation in the presence of the molybdenum that in does in the presence of the glass. Making EDM-style cells by attaching glass endplates to the maser cylinder would determine which factor was more important, but this experiment has not yet been performed. Even so, there are reasons to believe that the second hypothesis is the correct one. By using metal endplates which are impermeable to the Xe, the gas is prevented from being trapped in niches that cause relaxation. Furthermore the endplates used may have fewer magnetic impurities than the glass. When the endplates were made from a different company's molybdenum sheeting, the Xe T_1's clearly decreased. (This demonstrates that the cleaning procedure is not the only factor in determining T_1.) Finally there is the work of Thad Walker's group, which has measured Xe T_1's for surfaces of gold and silver and found them to be about twenty minutes for a 1 cm cube at room temperature [92]. This demonstrates that metals can have relaxation rates at least comparable to coated glass.

To conclude this section, here are a few comments on cell death. Observations suggest that the EDM cells stop working when the coating is burned, when excessive high voltage is applied to the endplates, or when the rubidium is driven out of the pump bulb. The first two methods are avoidable and so of little interest. However, the driving of the rubidium out of the cells is considerably more complicated. Surprisingly, one generally does not simply see a gradual decrease in signal with time. Instead much of the aging occurs in the cycles of heating the cell from room temperature to operating conditions and back again. Since this is a concern, it is difficult to judge if cells go bad just sitting on the shelf. Some cells have been observed to undergo an abrupt change in performance shortly after being heated up. The helium

signal nosedives, dropping an order of magnitude in size over the course of several days. The decay of the xenon is slower, but tends to accelerate about the point that the helium signal has completely vanished. The T_1's remain roughly constant through the decline. Note that this description is consistent with the rubidium being driven from the pump bulb. Essentially there is less [Rb] than one would expect from Killian's formula, and so a lower effective temperature for purposes of spin exchange. Naturally this affects the helium more strongly than the xenon at first, until the [Rb] is so low that not even the xenon is polarized to an appreciable extent. As mentioned in section 2.2.6, attempts to chase the rubidium back into the pump bulb have not been successful. Typical heating periods were 3-5 days: perhaps waiting for weeks or months would yield better results.

BIBLIOGRAPHY

BIBLIOGRAPHY

[1] S.M. Barr, W.J. Marciano in"CP Violation", ed. C. Jarlskog, World Scientific, Teaneck, New Jersey, 1989

[2] S.M. Barr, Int. J. Mod. Phys. A **8** 209, 1993

[3] S.M. Barr in "Particle Astrophysics, Atomic Physics, and Gravitation", eds. J. Tran Thanh Van, G. Fontaine, E. Hinds, Editions Frontieres, Cedex, France, 1994

[4] Phillip Bevington and D. Keith Robinson, *Data Analysis and Error Reduction for the Physical Sciences, 2nd edition*, McGraw-Hill Inc., Singapore, 1989

[5] A. Baranga, S. Appelt, M. Romalis, C. Erickson, A. Young, G. Cates, W. Happer, Phys. Rev. Lett **80** 2801, 1998

[6] F.P. Calaprice, W. Happer, D.F. Schreiber, M.M. Lowry, E. Miron, and X. Zeng, Phys. Rev. Lett. **54** 174, 1985

[7] G.D. Cates et al. Phys. Rev. A **38** 5092, 1988

[8] G.D. Cates et al. Phys. Rev. A **49** 4631, 1992

[9] J.H. Christenson, J.W. Cronin, V.L. Fitch, R. Turlay, Phys. Rev. Lett. **13** 138, 1964

[10] T.E. Chupp and K.P. Coulter, Phys. Rev. Lett. **55** 1074, 1985

[11] T.E. Chupp, E.R. Oteiza. J.M. Richardson, and T.R. White, Phys. Rev. A **38** 3998, 1988

[12] T.E. Chupp, R.A. Loveman, A.K. Thompson, A.M. Bernstein, and D.R. Tieger, Phys. Rev. C **45** 915, 1992

[13] T.E. Chupp, R.J. Hoare, R.L. Wlasworth, and Bo Wu, Phys. Rev. Lett. **72** 2363, 1994

[14] Cirrus Software, S28A, C2, R.R.1, Kaleden, BC, Canada V0H 1K0, cirrus@vip.net

[15] Coherent, 5100 Patrick Henry Dr., Santa Clara, CA 95054, (877) 434-6337

[16] E.D. Commis, S.B. Ross, D. Demille, B.C. Regan, Phys. Rev. A **50** 2960, 1989

[17] *CRC Standard Probability and Statistics, Tables and Formulae*, ed. William Beyer, CRC Press Inc., Ann Arbor, 1991

[18] G.D. Cates, S.R. Schaeffer, W. Happer, Phys. Rev. A **37** 2877, 1988

[19] R.E. Cunningham and R.J.J. Williams, *Diffusion in Gases and Porous Media*, Plenum Press, New York, 1980

[20] D.A. Dicus, E.W. Kolb, V.L. Teplitz, R.V. Wagoner, Phys. Rev. D **18** 1829, 1978

[21] B. Driehuys, G.D. Cates, W. Happer, Phys Rev. Lett. **74** 4943, 1995

[22] John Ellis and N.N. Mavromatos, to appear in Physics Reports, 1999 (hep-ph/9903386)

[23] Epoxy Technology Inc., 14 Fortune Drive, Billerica, MA 01821, (800) 227-2201

[24] Equilon Enterprises

[25] J.A. Fedchak, P. Cabauy, W.J. Cummings, C.E. Jones, and R.S. Kowalczyk, Argonne National Laboratory, Argonne, IL 60439-4843

[26] V.V. Flaumbaum, I.B. Kriplovich, O.P. Sushkov, Phys. Lett. B **162** 213, 1985

[27] V.V. Flaumbaum, I.B. Kriplovich, O.P. Sushkov, Nuclear Physics A **449** 750, 1986

[28] V. Spevak, N. Auerbah, and V.V. Flaumbaum, Phys. Rev. C **56** 1357, 1997

[29] John M. Fluke Co., 6920-T Seaway Blvd., Everett, WA 98203, (206)-347-6100

[30] R.L. Gamblin and T.C. Carver, Phys. Rev. A **138** 946, 1965

[31] Glassman High Voltage, Route #22 (East), Salem Industrial Park, P.O. Box 551, Whitehouse Station, NJ 08889, (908) 534-9007

[32] David J. Griffiths, *Introduction to Electrodynamics, 2nd edition*, Prentice-Hall, Inc., Englewood Cliffs, N.J., 1989

[33] Martin G.H. Gustavsson and Ann-Marie Matensson-Pendril, Phys. Rev. A **58** 3611, 1998

[34] W. Happer and W.A. Van Wijngaarden, Hyperfine Interactions **38** 435, 1987

[35] P.G. Harris et al. Phys. Rev. Lett. **82** 904, 1999

[36] R.M. Herman, Phys. Rev. A **137** 1062, 1965

[37] Hirschfelder, Curtiss, Bird, *Molecular Theory of Gases and Liquids*, John Wiley & Sons, New York, 1965

[38] D.A. Howe, D.W. Allen, and J. A Barnes, "Properties of Signal Sources and Measurement Methods", *Proceedings of the 35th Annual Symposium on Frequency Control*, 1981

[39] Rohan Hoare, Ph.D. Thesis, Harvard University, 1993

[40] Hewlett-Packard, 3000 Hanover St., Palo Alto, CA 94304, (800) 829-4444

[41] Ithaco, Inc., Ithaco, NY 14850

[42] J.D. Jackson, *Classical Electrodynamics, 2nd edition*, John Wiley & Sons, New York, p186, 1975

[43] James P. Jacobs, Ph.D. Thesis, University of Washington, 1991

[44] J.P. Jacobs, E.N. Fortson, S.K. Lamoreaux, W.M. Klipstein, B. Heckel, Phys. Rev. A **52** 3521, 1995

[45] Cynthia Jameson, University of Illinois, Chicago (private communication)

[46] A.J. Kastler, Phys. Radium **11** 225, 1950

[47] I.B. Khriplovich in "Atomic Physics 11", eds. S. Harouche, J.C. Gay, G. Grynberg, World Scientific, Teaneck, New Jersey, 1989

[48] I.B. Khriplovich, *Parity Nonconservation in Atomic Phenomena*, Gordon and Breach Science Publishers, Philadelphia, 1991

[49] J.-E. Kim, Phys. Rep. **150** 1, 1987

[50] M. Kitano, et al. Phys. Rev. Lett. **60** 2133, 1988

[51] Keithley Instruments, 28775 Aurora Rd., Cleveland, OH 44139, (440) 248-0400

[52] J. Kestin, K. Knierim, E.A. Mason, B. Najafi, S.T. Ro, M. Waldman, J. Phys. Chem. Ref. Data **13** 238, 1984

[53] Kilovac, P.O. Box 4422, Santa Barbara, CA 93140, (805) 684-4560

[54] Edward W. Kolb, Michael S. Turner, *The Early Universe*, Addison-Wesley Publishing Co., New York, 1990

[55] Kenneth Krane, *Introductory Nuclear Physics*, John Wiley & Sons, New York, p73, 1987

[56] S.K. Lamoreaux, Phys. Rev. A **53** R3705, 1996

[57] Linear Research, 5231-T Cashima Place, Suite 21, San Diego, CA 92110, (619) 299-0719

[58] G. Luders, Ann. Phys. **2** 1, 1957

[59] Rivka Maoz and Jacob Sagiv, Journal of Colloid and Interface Science **100** 465, 1984

[60] Bruce McKellar, University of Melbourne, private communincation

[61] D.D. McGregor, Phys. Rev. A **41** 2361, 1990

[62] MKS Instruments, 6 Shattuck Rd., Andover, MA 01810, (800) 227-8766

[63] R.N. Mohapatra in "CP Violation", ed. C. Jarlskog, World Scientific, Teaneck, New Jersey, 1989

[64] A. Martensson-Pendrill, Phys. Rev. Lett. **54** 1153, 1985

[65] William Press, Brian Flannery, Saul Teukolsky, and William Vetterling, *Numerical Recipes*, Cambridge Univeristy Press, New York, 1986

[66] Omega, P.O. Box 4047, Stamford, CT 06907, (800) 826-6342

[67] Opto-Power Corporation, 3321 E. Global Loop, Tuscon, AZ 85706, (520) 746-1234

[68] Eduardo R. Oteiza, Ph.D. thesis, Harvard University, 1992

[69] Donald H. Perkins, *Introduction to High Energy Physics, 3rd edition*, Addison-Wesley Publishing Company, Inc., Menlo Park, 1987

[70] Norman Ramsey, Phys. Rev. **100** 1191, 1955

[71] Ramsey, Miron, Zeng, and Happer, Chem. Phys. Lett. **102** 340, 1983

[72] F. Reif, *Fundamentals of Statistical and Thermal Physics*, McGraw-Hill Book Company, New York, 1965

[73] M.G. Richards, B.P. Cwan, M. F. Secca, and K. Machin, J. Phys. B **21** 665, 1988

[74] H.G. Robinson and T. Myint, Appl. Phys. Lett. **5** 116, 1964

[75] Matt Rosen, University of Michigan, private communication

[76] Robert G. Sachs, *The Physics of Time Reversal*, The University of Chicago Press, Chicago, 1987

[77] Rick Stoner, David Bear, Ron Walsworth, Harvard-Smithsonian Center for Astrophysics, private communications, 1998-1999

[78] L.I. Schiff, Phys. Rev. **132** 2194, 1963

[79] Leonard I. Schiff, *Quantum Mechanics, 3rd edition*, McGraw-Hill Book Co., New York, 1963

[80] Betram Schwarzchild, Physics Today **52** 21, 1999

[81] Tobb B. Smith, Ph. D. Thesis, University of Michigan, 1998

[82] SAES Pure Gas, 4175 Santa Fe Rd., San Luis Obispo, CA 93401, (805) 541-9299

[83] Stanford Reserach Systems Manual for the Model SR850 DSP Lock-In Amplifier 1992

[84] Stanford Research Systems, 1290D Reamwood Ave., Sunnyvale, CA 94089, (408) 744-9040

[85] R.E. Stoner, M.A.Rosenberry, J.T. Wright, T.E. Chupp, E.R. Otieza, and R.L. Walsworth Phys Rev. Lett. **77** 3971, 1996

[86] R.E. Stoner, Harvard-Smithsonian Center for Astrophysics (private communiucation) 1997

[87] David Taber, *Gases,Liquids,and Solids, 2nd ed.*, Columbia Uiversity Press, New York, 1979

[88] T.C. Vold, F.J. Raab, B. Heckel, E.W. Fortson, Phys. Rev. Lett. **52** 229, 1984

[89] T.G. Walker, Phys. Rev. A **40** 4959, 1989

[90] M.E. Wagshul, T.E. Chupp, Phys. Rev. A **40** 4447, 1989

[91] M.E. Wagshul, Ph.D. Thesis, Harvard University, 1991

[92] Thad Walker, University of Wisconisn, private communication, 1999

[93] WaveTek, 9045 Balboa Ave., San Diego, CA 92123, (800) 854-2708

[94] WaveMetrics, P.O. Box 2088, Lake Oswego, OR 97035, (503)-620-3001

[95] Z. Wu, T. G. Walker, W. Happer, Phys. Rev. Lett. **54** 1921, 1985

[96] X. Zeng, Z. Wu, T. Call, E. Mirion, D. Schreiber, W. Happer, Phys. Rev. A **31** 260, 1985

ABSTRACT

A PRECISION MEASUREMENT OF THE ^{129}Xe ELECTRIC DIPOLE MOMENT USING DUAL NOBLE GAS MASERS

by

Mark A. Rosenberry

Chairperson: Professor Timothy Chupp

Abstract: This dissertation describes a measurement of the permanent electric dipole moment (EDM) in ^{129}Xe. An EDM violates both parity and time reversal, and so its size sets limits on the **CP**-violating parameters of the Standard Model and its extensions. Two species of noble gas Zeeman masers were employed to achieve this precision. Zeeman masers are tools that permit very long running times and the advantages of *in situ* magnetometry. The Bloch equations that model the maser behavior are derived, and their solution predicts the maser polarizations for different system settings. Details of the construction of the apparatus (particularly the EDM cells employed) are provided. Over a six month period the experiment achieved a statistical sensitivity of 2.84×10^{-27} e cm but was limited by a systematic effect whose origin is unknown. Various approaches for identifying and eliminating this systematic are discussed.